

Assessments of and Applications for High Spatio-Temporal Resolution X-Ray Detectors for Use in Medical Imaging

Jordan M Krebs

May 11th, 2020

A dissertation submitted to the Faculty of the Graduate School of The State University of New York at Buffalo in partial fulfillment of the requirements for the degree of
Doctor of Philosophy

Department of Radiology (Medical Physics Program)

ProQuest Number:27995681

All rights reserved

INFORMATION TO ALL USERS

The quality of this reproduction is dependent on the quality of the copy submitted.

In the unlikely event that the author did not send a complete manuscript and there are missing pages, these will be noted. Also, if material had to be removed, a note will indicate the deletion.



ProQuest 27995681

Published by ProQuest LLC (2020). Copyright of the Dissertation is held by the Author.

All Rights Reserved.

This work is protected against unauthorized copying under Title 17, United States Code
Microform Edition © ProQuest LLC.

ProQuest LLC
789 East Eisenhower Parkway
P.O. Box 1346
Ann Arbor, MI 48106 - 1346

Copyright by

Jordan Michael Krebs

2020

Dedication

I dedicate this work to my daughters. I love you all and hope that someday you are able to pursue your own dreams and find the same success and support that I have.

Acknowledgments

It's difficult to even know where to begin when thanking all the people who have helped make this a possibility.

First of all, I would like to thank my graduate advisor and mentor, Dr Stephen Rudin, for taking me on as a student and guiding me up to this point. Dr Rudin was quick to take me under his wing offering me a position on his team. Dr Rudin has consistently provided me with direction and guidance as I've developed new skills as a researcher and scientist. Dr Rudin has been a wonderful teacher in the classroom, in the lab, and in the day-to-day of research. I'm so grateful for everything he has taught me and for the opportunity provided to work on some truly unique research projects.

I would also like to thank Dr Daniel R. Bednarek and Dr Ciprian N. Ionita for additional advice, expertise and instruction. Both taught classes critical to my understanding of medical physics and their advice regarding abstracts, papers, and other research material has been invaluable in my success as a student and researcher.

Dr Iris Z. Wang and Dr Joseph Spornyak were kind enough to agree to be a part of my committee and have also been excellent in instructors. I am truly grateful for the time and effort to teach me along with all the other members of the medical physics faculty.

Dr Megan K Russ and Dr Alok Shankar also served as mentors for me, teaching me about physics and helping me with so many projects. I'm grateful not only for their help and friendship, but also for answering my endless questions and giving me advice that has helped me pursue my own career as a medical physicist. They were also kind enough to allow me to participate in their own research projects as I began my student career here in at the University at Buffalo.

All of the individuals at the Canon Stroke and Vascular Research Center (CSVRC) have been exceptionally helpful in aiding me to pursue the research. In particular I would like to thank Dr. Swetadri Vasan Setlur Nagesh for aiding me with the technical expertise required to use the equipment at CSVRC and for the advice to improve my projects. Liza Gutierrez was invaluable in aiding with acquiring equipment and also advising on experiments, along with managing all the administrative responsibilities in the lab. It is also my pleasure to acknowledge the aid of Mike Rejewski, Haruki Iwai, Ko Fuchigami, Zhenyu Xiong, Alexander Podgorsak, Chao Guo, Lauren Shepard, Jonathan Troville, Allison Shields, and Jacob Collins.

I would also like to thank Justin and Kate Kay, Zach and Lauren Huber, and Daniel Desrosiers who have been friends to me, a stranger in Buffalo.

I am grateful to Jennifer Hwu, Larry Sadwick, Derek Kress, Sam Judd and the rest of my coworkers from Innosys Inc who provided me my first exposure to research and were supportive of my efforts to continue my education, even providing letters of recommendation that helped me enter the graduate program here at the University at Buffalo.

I could never thank my parents enough for all of their support. They have both cheered me on every step of the way. They have sacrificed so much for me, so that I could get to this point. I will never be able to repay them or sufficiently express my gratitude.

Finally, to my darling wife. She has been a better companion than I could have ever asked for. Even when I didn't believe in myself she still did. She has spent an incalculable amount of time listening patiently to my endless descriptions of projects and has served as a sounding board whenever I had to write. I am so grateful she was willing to leave behind our comfortable life and family so that I could pursue my dream. Thank you.

Table of Contents

Copyright	ii
Dedication	iii
Acknowledgments	iv
List of Tables	ix
List of Figures	x
List of Videos	xvi
List of Abbreviationsxviii
Abstract	xx
1 Introduction	1
1.1 Motivation	1
1.2 Risk of Stroke	2
1.3 Stroke Diagnosis and Treatment	3
1.3.1 Treatment of Ischemic Stroke	4
1.3.2 Treatment of Hemorrhagic Stroke	4
1.4 Imaging Technologies	5
1.4.1 Image Intensifiers	6
1.4.2 Flat Panel Detectors	8
1.5 Region of Interest Imagers	10
1.6 Present Work	11
2 Comparison of Integrated Detector Modes Through Use of Imaging Metrics Including the Relative Object Detectability (ROD) Family of Metrics	13
2.1 Introduction	13
2.2 Materials and Methods	14
2.2.1 Details of Detector Modes	14
2.2.2 Qualitative and Semi-Quantitative Comparisons	15
2.2.3 Standard Metrics	16
2.2.4 Generalized Metrics	18

2.2.5	Relative Object Detectability Metrics	19
2.3	Results	23
2.3.1	Qualitative and Semi-Quantitative Comparisons	23
2.3.2	Standard Metrics	25
2.3.3	Generalized Metrics	28
2.3.4	ROD Metrics for Hi-Def Relative to FPD Mode	31
2.4	Discussion	36
2.5	Conclusion	37
3	Effect of Anti-Scatter Grid on Performance of Hi-Def Mode	38
3.1	Introduction	38
3.2	Materials and Methods	39
3.2.1	Details of the Anti-Scatter Grid	39
3.2.2	Metrics Used for Comparison	41
3.3	Results	43
3.3.1	Standard Metrics	43
3.3.2	G-ROD Metrics	49
3.4	Discussion	52
3.5	Conclusion	52
4	Assessment of Gantry-Motion Blur in Both Individual Projections and in Recon- structed Images for Cone Beam CT and Tomography	53
4.1	Introduction	53
4.2	Materials and Methods	54
4.2.1	Magnitude of Motion-Induced Blur Due to Gantry Rotation	54
4.2.2	Gantry Rotational Motion-Induced Blur in Cone-Beam Computed Tomog- raphy	59
4.3	Results	62
4.3.1	Magnitude of Motion-Induced Blur Due to Gantry Rotation	62
4.3.2	Gantry Rotational Motion-Induced Blur in Cone-Beam Computed Tomog- raphy	64
4.4	Discussion	71
4.5	Conclusion	72
5	Initial Investigations of 1000 FPS High Speed Angiography (HSA) and the Use of HSA in Endovascular Image Guided Interventions	73
5.1	Introduction	73
5.2	Materials and Methods	75
5.2.1	XCounter's Actaeon Detector	75
5.2.2	3D Printed Phantoms	77
5.2.3	Experimental Setup	80
5.3	Results	82
5.3.1	Initial Visualization of Flow Patterns Using 1000 FPS HSA	82
5.3.2	Increasing Imaging Timing Window	85
5.4	Discussion	88

5.5	Conclusion	90
6	Quantification of Blood Flow Velocities Acquired with HSA Sequences	92
6.1	Introduction	92
6.2	Materials and Methods	93
6.2.1	HSA Quantitative Flow Analysis	93
6.2.2	Performing X-Ray Particle Image Velocimetry (X-PIV) with HSA	95
6.2.3	Impact of Frame Rates on X-PIV	97
6.3	Results	97
6.3.1	HSA Quantitative Flow Analysis	97
6.3.2	Performing X-Ray Particle Image Velocimetry (X-PIV) with HSA	100
6.3.3	Impact of Frame Rates on X-PIV	120
6.4	Discussion	125
6.5	Conclusion	126
7	Summary and Future Works	127
7.1	Summary	127
7.2	Future Works	130
7.2.1	Impact of Anti-Scatter Grid on Hi-Def Mode	130
7.2.2	Quantification of Blood Flow with HSA	131
7.2.3	Time Dependent Comparative Metrics	131
7.3	Conclusions	132
	References	133
	Appendix A: List of Publications and Presentations	141

List of Tables

2.1	Evaluation of line-pair detector resolution in various detector modes	25
2.2	GM-ROD values for different magnifications and spatial frequency integration bounds.	35
5.1	Limitations on the number of frames due to current limitations in the Actaeon's on-board memory.	86

List of Figures

1.1	Diagram of image intensifier's structure (Source: The AAPM/RSNA Physics Tutorial for Residents).	7
1.2	Images depicting the pincushion distortion (left) and S distortion (right), two artifacts that image intensifiers are susceptible to (Source: The AAPM/RSNA Physics Tutorial for Residents).	8
1.3	Diagrams of an individual dixel (left) and the circuitry for a TFT flat panel system (right).	9
1.4	Examples of ROI detectors showing a detector to be mounted to a c-arm (a) and one integrated into a c-arm (b) (Source: Canon Medical Systems).	11
2.1	Canon's Alphenix detector with integrated Hi-Def and FPD imaging modes (Source: Canon Medical Systems).	15
2.2	Examples of (a) $obj(x, y)$ and (b) $OBJ(f_x, f_y)$ for an aluminum sphere.	20
2.3	Examples of how changing the $OBJ(f_x, f_y)$ function impacts the resultant image with (a) containing all image data for $OBJ(f_x, f_y)$, (b) containing image data from $0 \frac{lp}{mm}$ to $1 \frac{lp}{mm}$, and (c) containing image data from $1 \frac{lp}{mm}$ to the Nyquist.	22
2.4	Stent $OBJ(f_x, f_y)$ function showing (a) all of frequency space and (b) frequency space from $1 \frac{lp}{mm}$ to the Nyquist.	23
2.5	Images acquired of a pipeline stent deployed in a vascular phantom using (a) the new detector's FPD mode and (b) the new detector's Hi-Def mode.	24
2.6	Images acquired of pipeline stent deployed in a vascular phantom using (a) the new detector's FPD mode and (b) the new detector's Hi-Def mode.	24
2.7	Images acquired of a deployed pipeline stent in a vascular phantom using (a) the new detector's FPD mode and (b) the new detector's Hi-Def mode.	25

2.8	Plot of the MTF for Hi-Def and FPD zoom modes.	26
2.9	Plot of the NNPS for Hi-Def and FPD zoom modes.	27
2.10	Plot of the DQE for Hi-Def and FPD zoom modes.	28
2.11	Plot of the G-MTF for Hi-Def and FPD zoom modes ($\rho = 0.34$, mag = 1.05).	29
2.12	Plot of the G-MTF for Hi-Def and FPD zoom modes ($\rho = 0.34$, mag = 1.40).	29
2.13	Plot of the GDQE for Hi-Def and FPD zoom modes ($\rho = 0.34$, mag = 1.05).	30
2.14	Plot of the GDQE for Hi-Def and FPD zoom modes ($\rho = 0.34$, mag = 1.40).	30
2.15	Plot of the ROD metric for Hi-Def and FPD zoom modes for spheres, discs, and wires.	31
2.16	$OBJ(f_x, f_y)$ function for a 50μ diameter (a) sphere and (b) wire.	32
2.17	Plot of the G-ROD metric for Hi-Def and FPD zoom modes for spheres, discs, and wires.	33
2.18	Plot of the G-ROD metric for Hi-Def and FPD zoom modes for spheres, discs, and wires.	33
2.19	Stent images acquired using (a) the FPD zoom mode and (b) the Hi-Def zoom mode.	34
2.20	Inverted stent images acquired using (a) the FPD zoom mode and (b) the Hi-Def zoom mode.	35
3.1	Diagram of an anti-scatter grid showing septa and interspace material. The septa are made of dense material, usually lead, to attenuate scattered radiation.	39
3.2	Picture of the grid equipped to the Alphenix detector.	40
3.3	Diagram demonstrating how the G-MTF was measured for the Hi-Def zoom mode with and without anti-scatter grid.	42
3.4	Detector G-MTF measured with and without the anti-scatter grid in place for the 2.3 inch FOV using the Hi-Def mode.	44
3.5	Detector G-MTF measured with and without the anti-scatter grid in place for the 3.0 inch FOV using the Hi-Def mode.	44

3.6	Detector NNPS measured with and without the anti-scatter grid in place for the 2.3 inch FOV using the Hi-Def mode. Exposure measured just prior to the grid was measured to be 324 nGy.	45
3.7	Detector NNPS measured with and without the anti-scatter grid in place for the 3.0 inch FOV using the Hi-Def mode. Exposure measured just prior to the grid was measured to be 324 nGy.	46
3.8	GDQE measured with and without the anti-scatter grid in place for the 2.3 inch FOV using the Hi-Def mode. Exposure measured at the detector surface was measured to be 188 nGy.	47
3.9	GDQE measured with and without the anti-scatter grid in place for the 3.0 inch FOV using the Hi-Def mode. Exposure measured at the detector surface was measured to be 188 nGy.	47
3.10	GDQE measured with and without the anti-scatter grid in place for the 2.3 inch FOV using the Hi-Def mode. The GDQE was calculated with the air kerma measured just prior to the grid (324 nGy).	48
3.11	GDQE measured with and without the anti-scatter grid in place for the 3.0 inch FOV using the Hi-Def mode. The GDQE was calculated with the air kerma measured just prior to the grid (324 nGy).	48
3.12	G-ROD measured with and without the anti-scatter grid in place for the 2.3 inch FOV using the Hi-Def mode.	49
3.13	G-ROD measured with and without the anti-scatter grid in place for the 3.0 inch FOV using the Hi-Def mode.	50
3.14	G-ROD measured with and without the anti-scatter grid in place for the 2.3 inch FOV using the Hi-Def mode. The GDQE was calculated with the air kerma measured just prior to the grid.	51
3.15	G-ROD measured with and without the anti-scatter grid in place for the 3.0 inch FOV using the Hi-Def mode. The GDQE was calculated with the air kerma measured just prior to the grid.	51
4.1	Diagram of a point object rotating about the gantry isocenter to illustrate gantry motion-induced blur in projection images.	55
4.2	Diagram of a point object rotating about the gantry isocenter with the geometry labeled to facilitate calculating image projection blur.	56

4.3	Sample line profiles acquired with and without gantry motion. The dashed green line shows the background grayscale level and the dashed gray lines approximate the lines fitted to the BB edges for measuring the blurred BB width.	58
4.4	Simulated pattern phantom with fine features used to measure the effects of gantry motion blur on reconstructed images.	60
4.5	Sinogram of projections acquired every 0.1° from the simulated pattern phantom. Projection angles are along the vertical axis and detector values are along the horizontal axis.	61
4.6	Images showing (a) the effect of motion blur along the direction of gantry rotational motion compared to (b) no gantry motion. Gantry rotational speed was fixed at $20^\circ s^{-1}$, with the object positioned 25 cm from isocenter with a frame length of 34.2 ms.	63
4.7	Magnitude of blurred BB width plotted as a function of distance from isocenter. . .	64
4.8	Simulated 30 fps (33.3 ms acquisition time) sinogram. Projection angles are along the vertical axis and detector values are along the horizontal axis.	65
4.9	Simulated 60 fps (16.7 ms acquisition time) sinogram. Projection angles are along the vertical axis and detector values are along the horizontal axis.	65
4.10	Simulated 120 fps (8.3 ms acquisition time) sinogram. Projection angles are along the vertical axis and detector values are along the horizontal axis.	66
4.11	Reconstructed image using the simulated 30 fps (33.3 ms acquisition time) sinogram.	67
4.12	Reconstructed image using the simulated 60 fps (16.7 ms acquisition time) sinogram.	68
4.13	Reconstructed image using the simulated 120 fps (8.3 ms acquisition time) sinogram.	69
4.14	Images show upper left quadrants of (a) the simulated pattern phantom and the reconstructed images using (b) the simulated 30 fps sinogram, (c) the simulated 60 fps sinogram, and (d) the simulated 120 fps sinogram. The axis rotation corresponds to the bottom right corner of each image.	70
4.15	Blur measurements relative to simulated objects' distance from isocenter. Points are measured blur and dashed lines are the theoretically predicted blur vales.	71
5.1	XCounter's Actaeon detector (Source: Direct Conversion).	76
5.2	Flow chart illustrating the steps used to print patient specific phantoms.	78

5.3	Objet Eden 260V Polyget 3D printer (Source: Stratasys).	79
5.4	3D printed phantoms used to illustrate flow patterns using HSA imaging. Phantoms are described in the text above.	80
5.5	3D printed phantoms used to illustrate flow patterns using HSA imaging.	81
5.6	Images showing (a) a single frame acquired at 1000 fps HSA and (b) a DA image simulated by integrating 100 consecutive HSA frames.	83
6.1	Picture of the 3D printed aneurysm phantom used to develop methods for flow measurements.	94
6.2	Method for producing difference images in which successive images are subtracted from one another to highlight the flow of iodine contrast.	95
6.3	Velocity vectors plotted on projection image of 3D printed aneurysm phantom. . . .	98
6.4	X-PIV measurements in the bifurcated carotid artery phantom made using the automated trackpy software with (a) being the raw velocity data measurements and (b) being the smoothed velocity data.	103
6.5	X-PIV measurements in the bifurcated carotid artery phantom made using the manual tracking method with (a) being the raw velocity data measurements and (b) being the smoothed velocity data.	104
6.6	Histogram velocities measured in the bifurcated carotid artery phantom.	105
6.7	X-PIV measurements in the internal carotid artery with idealized saccular aneurysm phantom made using the automated trackpy software with (a) being the raw velocity data measurements and (b) being the smoothed velocity data.	107
6.8	X-PIV measurements in the internal carotid artery with idealized saccular aneurysm phantom made using the manual tracking method with (a) being the raw velocity data measurements and (b) being the smoothed velocity data.	108
6.9	Histogram velocities measured in the internal carotid artery with idealized saccular aneurysm phantom.	109
6.10	X-PIV measurements in the internal carotid artery with wide-necked saccular aneurysm phantom made using the automated trackpy software with (a) being the raw velocity data measurements and (b) being the smoothed velocity data.	111

6.11 Histogram velocities measured in the internal carotid artery with wide-necked sac- cular aneurysm phantom.	112
6.12 X-PIV measurements in the basilar apex saccular aneurysm phantom made using the automated trackpy software with (a) being the raw velocity data measurements and (b) being the smoothed velocity data.	114
6.13 Histogram velocities measured in the basilar apex saccular aneurysm phantom. . .	115
6.14 X-PIV measurements in the idealized basilar apex saccular aneurysm phantom made using the automated trackpy software with (a) being the raw velocity data measurements and (b) being the smoothed velocity data.	117
6.15 Histogram velocities measured in the idealized basilar apex saccular aneurysm phantom.	118
6.16 Histogram comparing manual and automated X-PIV measurements for the bifur- cated carotid artery phantom.	119
6.17 Histogram comparing manual and automated X-PIV measurements for the internal carotid artery with idealized saccular aneurysm phantom.	120
6.18 X-PIV measurements in the internal carotid artery with wide-necked saccular aneurysm phantom made using the automated trackpy software for (a) 500, (b) 333, (c) 250, and (d) 200 fps image sequences.	121
6.19 Averaged X-PIV measurements in the internal carotid artery with wide-necked sac- cular aneurysm phantom made using the automated trackpy software for (a) 500, (b) 333, (c) 250, and (d) 200 fps image sequences.	122
6.20 Histogram comparing the relative frequency of measured velocities for simulated 500 fps are compared to the ground truth. Both measurements were made via trackpy X-PIV.	123
6.21 Histogram comparing the relative frequency of measured velocities for simulated 333 fps are compared to the ground truth. Both measurements were made via trackpy X-PIV.	123
6.22 Histogram comparing the relative frequency of measured velocities for simulated 250 fps are compared to the ground truth. Both measurements were made via trackpy X-PIV.	124
6.23 Histogram comparing the relative frequency of measured velocities for simulated 200 fps are compared to the ground truth. Both measurements were made via trackpy X-PIV.	124

List of Videos

- 5.1 Example of high speed images acquired at 1000 fps using HSA. Video also available at: <https://youtu.be/Urb0COsh-xw>. 74
- 5.2 1000 fps HSA video showing blood flow detail in a saccular aneurysm phantom before treatment. Video also available at: <https://youtu.be/7vMbosANtFg>. 84
- 5.3 1000 fps HSA video showing blood flow detail in a saccular aneurysm phantom after treatment with a pipeline embolization device flow-diverter. Video also available at: <https://youtu.be/kJ3zjgIsIA4>. 85
- 5.4 1000 fps HSA video showing blood flow detail in a saccular aneurysm phantom. Flow dynamic visualization limited by short x-ray pulses (83 ms) and limited duty cycle (50%). Video also available at: <https://youtu.be/gL1LV7wZfQo>. . . 87
- 5.5 1000 fps HSA video showing blood flow detail in a saccular aneurysm phantom. Flow dynamic visualization improved by continuous x-ray exposure for 3 s. Video also available at: <https://youtu.be/1pIksOL11P8>. 88
- 5.6 HSA and DA images acquired simultaneously using the Actaeon detector. HSA images displaying flow details in the 3D printed aneurysm before treatment are shown in the images to the left while the right shows the DA images simulated from the HSA images and are played simultaneously for comparison. Video also available at: <https://youtu.be/m8wkeYdCqoY>. 89
- 5.7 HSA and DA images acquired simultaneously using the Actaeon detector. HSA images displaying flow details in the 3D printed aneurysm after treatment are shown in the images to the left while the right shows the DA images simulated from the HSA images and are played simultaneously for comparison. Video also available at: <https://youtu.be/rBc3qCOD08U>. 90
- 6.1 HSA sequence used to quantify blood flow using manual measurements of difference images obtained during iodine contrast injection. Video also available at: <https://youtu.be/rm53uyBDubQ>. 99

- 6.2 HSA sequence used to quantify blood flow using manual measurements of difference images obtained during iodine contrast injection. Video also available at: <https://youtu.be/ww79pD6amBg>. 100
- 6.3 HSA sequence of the bifurcated carotid artery phantom used for manual and automated X-PIV measurements. Video also available at: <https://youtu.be/cieH8w70sMs>. 102
- 6.4 HSA sequence of the internal carotid artery with idealized saccular aneurysm phantom used for manual and automated X-PIV measurements. Video also available at: <https://youtu.be/JwsmM-cEYHk>. 106
- 6.5 HSA sequence of the internal carotid artery with wide-necked saccular aneurysm phantom used for manual and automated X-PIV measurements. Video also available at: <https://youtu.be/IrnfxnoxRT4>. 110
- 6.6 HSA sequence of the basilar apex saccular aneurysm phantom used for manual and automated X-PIV measurements. Video also available at: <https://youtu.be/Kk4qxSdJXnE>. 113
- 6.7 HSA sequence of the idealized basilar apex saccular aneurysm phantom used for manual and automated X-PIV measurements. Video also available at: <https://youtu.be/rkmWNf0tCbc>. 116

List of Abbreviations

ACC - Anti-Coincidence Circuitry

AVM - Arteriovenous Malformation

CAPIDS - Control Acquisition Processing and Image Display System

CBCT - Cone Beam Computed Tomography

CFD - Computational Flow Dynamics

CMOS - Complementary Metal-Oxide-Semiconductor

CT - Computed Tomography

DA - Digital Angiography

DSA - Digital Subtraction Angiography

DQE - Detective Quantum Efficiency

EID - Energy Integrating Detector

EIGI - Endovascular Image Guided Interventions

ESF - Edge Spread Function

FOV - Field of View

FPD - Flat Panel Detector

fps - Frames per Second

G-DQE - Generalized Detective Quantum Efficiency

GM-ROD - Generalized Measured Relative Object Detectability

G-MTF - Generalized Modulation Transfer Function

G-NNPS - Generalized Normalized Noise Power Spectrum

G-ROD - Generalized Relative Object Detectability
HRF - High Resolution Fluoroscopy
HSA - High Speed Angiography
II - Image Intensifier
lp/mm - Line Pairs per mm
MRI - Magnetic Resonance Imaging
MTF - Modulated Transfer Function
MTF_D - Detector Modulation Transfer Function
MTF_F - Focal Spot Modulation Transfer Function
MTF_S - Scatter Modulation Transfer Function
NEQ - Noise Equivalent Quanta
NNPS - Normalized Noise Power Spectrum
NNPS_D - Detector Normalized Noise Power Spectrum
PCD - Photon Counting Detector
PIV - Particle Image Velocimetry
ROD - Relative Object Detectability
ROI - Region of Interest
SAD - Source to Axis Distance
SID - Source to Image Distance
SOD - Source to Object Distance
SNR - Signal to Noise Ratio
TFT - Thin Film Transistor
tPA - Tissue Plasminogen Activator
X-PIV - X-ray Particle Image Velocimetry

Abstract

Endovascular image guided interventions (EIGI) are a minimally invasive alternative for the treating stroke and other vascular diseases that minimize patient discomfort and have reduced mortality and morbidity. The image quality delivered to physicians, both in spatial and temporal resolution, can influence diagnostic and treatment decisions directly related to patient outcomes. Current state-of-the-art detector systems provide sub-optimal spatial resolution for visualization of fine image detail and temporal resolution has been limited to tens of frames per second at best. The medical physics research group at the University at Buffalo's Canon Stroke and Vascular Research Center has worked to improve both these aspects of imaging detectors, including an array of region-of-interest, small field-of-view, high-resolution detectors, and a new high-speed high-resolution direct-detector capable of providing high-quality images and detailed blood flow patterns.

The high-resolution properties of a region-of-interest "Hi-Def" detector was assessed with a family of detector metrics designated Relative Object Detectability (ROD) metrics. The ROD metrics are a task-based group of metrics that compare the relative imaging capabilities of different detector systems. The ROD metric is the product of a detector DQE and a simulated object function, integrated over all spatial frequencies, and divided by the respective integral of another detector. This metric gives an idealized comparison of the performance of two imaging systems in detecting specific objects. Another metric from the ROD family is the Generalized Relative Object Detectability (G-ROD) metric. This metric is calculated in a manner similar to the ROD metric but uses the Generalized DQE (G-DQE) which takes into account elements of the detector system such as focal spot size, scatter, etc. The final metric calculated was the Generalized Mea-

sured Relative Object Detectability (GM-ROD). The GM-ROD is measured using images of real objects, which gives the most accurate comparison of detector systems relative performance. The GM-ROD is calculated from the ratio of the square of the Fourier transform of the object's image, divided by the generalized NNPS (GNNPS), integrated over all spatial frequencies, and divided by the respective integral of another detector.

The bulk of this dissertation is principally concerned with the effects of high-speed motion and the application of high-speed detectors to new challenges. The first question examined is the effect of motion blur due to rapid gantry-motion, particularly during the acquisition of Cone-Beam CT (CBCT). The magnitude of the blur in individual projections is examined in relation to different factors such as gantry speed, object position, and x-ray pulse duration. This study was followed up by examining the contributions of individual projections to reconstructions. To do this, a detailed phantom was simulated and individual projections were intentionally blurred. From these blurred projections, the initial phantom was reconstructed using filtered backprojection, the reconstructed image was compared to the initial phantom, and the magnitude of blur was measured.

One of the greatest challenges facing EIGIs is evaluating the interventional procedure and assessing the impact of the procedure on blood flow. The application of high-speed imaging to this particular challenge has shown much potential in revealing detailed flow dynamics to interventionalists during a procedure. To examine such detail a new direct detector with 100 μm pixel spacing and 1000 fps imaging capabilities was used to image the motion of contrast in a number of models. Initially the movement of contrast within the heart of a mouse and subsequently a rabbit was examined under x-ray. Following this experiment, 3D printed models of arterial stenosis and cerebral aneurysms were examined for how these disease states may impact blood flow in the vessel. Methods for using high-speed imaging were examined based on frame rates, timing windows, and simultaneous acquisition during conventional DA and DSA exams.

Using high-speed angiography (HSA) enabled the quantification of flow details using multiple methods. Initially, flow velocities were measured manually by tracking blobs of contrast across multiple frames. Flow velocities were derived from this manually acquired positional information

and mapped onto vessel images. Later, particles soaked in contrast were injected into the same phantoms and were tracked using methods similar to those employed in particle image velocimetry (PIV) the current gold standard for measuring flow. Finally, the effects of stenosis on contrast flow were examined based on properties such as transit time and contrast density. Each method provided new experimental information into the flow dynamics within diseased vessels that may be useful to physicians in diagnosing, planning, and treating patients.

Chapter 1

Introduction

1.1 Motivation

The current state of the art method for treating arterial pathologies makes use of x-ray imaging to guide interventional devices through a patient's vasculature to the site of the pathology for minimally invasive treatment. These endovascular image guided interventions (EIGIs) make use of state of the art technology that enables radiologists to visualize image details during treatment. Current detectors are limited in spatial resolution which may hinder the assessment of device use. It is for this reason that the imaging physics research team at the University at Buffalo SUNY has sought to improve the spatial resolution of interventional detectors. The first part of this work attempts to assess the performance improvement of a new high spatial resolution detector developed in conjunction with Canon.

Along with improvements to spatial resolution the same group is seeking to make improvements to the temporal resolution of x-ray detectors. Most detectors have very limited temporal resolution, achieving no more than 30 fps. With such low frame rates vascular flow detail present during contrast injections is almost entirely lost. This flow detail contains critical information that could be used to diagnose or track the condition of certain pathologies, or could be used to assess whether deployed devices have sufficiently altered flow dynamics to allow for healing. The second

part of this work examines the use of very high frame rates (up to 1000 fps) and how it may be employed in the clinic to improve interventional outcomes.

1.2 Risk of Stroke

A stroke is any disease that affects the vessels that carry oxygen and other nutrients to the brain and is the fifth leading cause of death. In the United States alone there are more than 795,000 strokes each year. The risk of stroke is greatest among the elderly with nearly 75 percent of strokes occurring in people over 65 and the risk of stroke more than doubles for every decade after 55.¹ Stroke is also the leading cause of disability in the United States resulting in a number of disabilities including problems with thinking, awareness, attention, learning, judgement, memory, speech, depression, numbness, pain, and paralysis.² Stroke occurs whenever an artery is either blocked by a clot or a vessel ruptures, preventing blood from reaching parts of the brain leading to the death of brain cells within minutes if proper blood flow is not restored. All strokes can be divided between two categories: ischemic (caused by a clot or obstruction in the vessel) and hemorrhagic (caused by vessel rupture).³

Ischemic strokes account for approximately 87 percent of all strokes. Ischemic strokes are caused primarily by fatty deposits that either develop onsite at the fatty plaque within the blood vessel (cerebral thrombosis) or develop elsewhere in the vascular system before becoming dislodged and causing a blockage in a smaller vessel in the brain (cerebral embolism).⁴ Some ischemic strokes are transient (often referred to as a ministroke) and last only a few minutes due to a temporary blockage. While ministrokes tend to do no permanent damage, they can indicate a more severe future stroke and merit the same immediate medical attention a typical stroke would receive.⁵

While only 13 percent of strokes are hemorrhagic,⁶ mortality rates of hemorrhagic strokes were found to be 32 percent after 30 days compared to 12 percent after 30 days for ischemic stroke.⁷ Hemorrhagic strokes occur when a cerebral vessel weakens and ruptures allowing blood to leak

into the brain. The pooling blood causes pressure to build up in the brain damaging the surrounding tissue. Two vascular conditions lead to a rupture in a cerebral vessel: aneurysms and arteriovenous malformations (AVMs).

An aneurysm is an enlarging of a blood vessel due to weak areas in the vessel and are the more common cause of hemorrhagic strokes.⁶ Aneurysms can be divided into two categories based on geometry: saccular and fusiform. The most common form of cerebral aneurysms are saccular aneurysms, where a weakened portion of the vessel wall balloons out into a rounded sac attached to an artery. Many aneurysms are small and cause no problems for patients. Nevertheless all aneurysms have the potential to rupture, causing a stroke.⁸ It is therefore critical to monitor and, if necessary, treat all diagnosed aneurysms.

AVMs are defects in the vascular system where a tangle of arteries and veins bypass capillaries and divert oxygenated blood from the arteries to the veins. This diversion of blood robs organs of some oxygen, though most AVMs are asymptomatic. Though the cause of AVMs is unknown, there is evidence that they develop either during pregnancy or shortly after birth.⁹ Because AVMs are composed of abnormal vessels they are weaker than typical vessels. High blood pressure can cause vessels to dilate over time leading to eventual leaking or burst, causing a stroke.¹⁰

1.3 Stroke Diagnosis and Treatment

Since stroke affects the brain symptoms may vary from person to person and can manifest throughout the body. Some of the most common symptoms include weakness or numbness (often in one side of the body), sudden dimness or loss of vision (particularly in one eye), difficulty speaking or understanding speech, dizziness, loss of balance, and sudden, excruciating headaches.¹¹ If someone shows symptoms of a stroke, they should be taken to the emergency room as quickly as possible for diagnosis, and treatment.

Upon arrival at the emergency room, patients with stroke-like symptoms typically undergo a computed tomography (CT) scan to localize the site of stroke and determine its cause. In some

cases, a magnetic resonance imaging (MRI) scan may also be necessary for small, deep injuries. Another common test is cerebral angiography in which X-ray contrast is injected into the cerebral vasculature and an x-ray image is taken. The x-ray contrast is more attenuating than surrounding tissue and remains confined to the vasculature causing it to display more prominently in the resulting x-ray image. The cerebral angiography highlights blood flow in the brain and allows physicians to identify size and location of blockages.¹² Once the stroke has been diagnosed and located, treatment depends on whether a stroke is ischemic or hemorrhagic.

1.3.1 Treatment of Ischemic Stroke

If the stroke is ischemic, then treatment requires the removal of the blockage to restore blood flow to the brain. One option is an injection of recombinant tissue plasminogen activator (tPA), also known as alteplase, which can dissolve clots. To minimize risk of long-term damage and death, alteplase must be administered to patients less than 4.5 hours after the symptoms of stroke began. In some cases, physicians may determine that an emergency endovascular procedure is necessary. In these cases a catheter is inserted into a patient's artery (usually in the groin) and fluoroscopically guided through the vasculature to the brain where drugs may be delivered directly to the site of the stroke, or where the clot may be removed mechanically using a stent retriever.¹³

1.3.2 Treatment of Hemorrhagic Stroke

Small, unruptured aneurysms are asymptomatic making them difficult to diagnose. As aneurysms grow, they may exert pressure on surrounding tissue causing pain, numbness, weakness, and other symptoms that may still go undiagnosed. In fact, most cerebral aneurysms go unnoticed until rupture or when detected during a medical imaging exam for another condition. Cerebral aneurysms are usually identified and located via CT, MRI, and cerebral angiography.⁸

If an aneurysm is identified before rupture and the patient is determined to be at risk of rupture, or if the aneurysm does rupture then there are three common treatment options available. First, a neurosurgeon gains access to the aneurysm after removing a section of the patient's skull and places

a clip at the neck of the aneurysm to stop the flow into it. Second, an interventional radiologist fluoroscopically guides a catheter to the aneurysm and fills the aneurysm with coils of wire that disrupts the flow of blood into the aneurysm, sealing it off from the main artery. Third, is for the interventional radiologist to deploy a flow diverter in the parent vessel. Flow diverters are stent-like tubes that divert flow away from an aneurysm and allow it to heal.¹⁴ Methods two and three are known as EIGIs and are less invasive than clipping. EIGIs also carry less risk of mortality and morbidity for the patient and so are coming to replace surgical procedures when possible.¹⁵

In the last few decades, the number of patients diagnosed with AVMs has doubled though only about 12% of people with AVMs experience symptoms. If an AVM begins to bleed it can lead to a hemorrhagic stroke. Once an AVM begins to bleed the odds of rebleeding increase and it becomes necessary to treat the AVM. Treatment options include microsurgery, endovascular embolization, and stereotactic radiotherapy.¹⁶ In microsurgical treatment a surgeon gains access to the AVM and it is resected from the brain. Endovascular embolization is a less invasive option in which a catheter is guided to the AVM during an EIGI and a substance (a glue or coils) is injected into the AVM to block the flow of blood into the vessel. In stereotactic radiosurgery, a focused beam of high-energy radiation are concentrated on the AVM, damaging the tissue, and causing a scar that blocks the bleeding.¹⁰

1.4 Imaging Technologies

EIGIs rely on x-ray imaging to guide the catheter to the interventional site and to carry out the intervention. This imaging must balance the physician's need to visualize the intervention against the dose delivered to the patient. Current methods use real-time, low-dose x-ray fluoroscopy, in which x-ray pulses (usually 3 to 30 pulses per second) create a video that allows physicians to monitor the progress of the intervention. Physicians may also use angiography, a higher dose method that images the passage of iodinated contrast through patient vasculature, to highlight patient anatomy and disease morphology. Digital image processing can also be used in conjunction with these

imaging methods to logarithmically subtract background structures or to provide physicians with a “roadmap” during fluoroscopy.

All x-ray modalities rely on the same principle method for producing x-rays, namely an x-ray tube. In x-ray tubes a tungsten cathode is heated up and releases electrons into a vacuum chamber. The electrons are focused and accelerated by electric fields towards a tungsten anode. A fraction of the electrons colliding with the anode produce x-rays with energies from 0 keV up to the maximum voltage difference applied to the tube. Since only a fraction of the electrons produce x-ray photons the majority of the energy becomes heat the anode can be spun to distribute the heat over a large surface area to handle larger workloads. Two types of x-ray detectors are predominately used in EIGIs: image intensifiers (IIs) and flat panel detectors (FPDs). These two detector types rely on different methods for converting x-ray information in visible light displayed to an interventionalist.

1.4.1 Image Intensifiers

First developed in 1948, the image intensifier amplifies light signals from an input phosphor to provide a conveniently bright visible light signal. The primary structures of the II as shown in figure 1.1 are the input phosphor, photocathode, focusing electrodes, anodes, output phosphor, and window. These various components work together to produce an electron beam that amplifies the original x-ray signal. The use of an electron beam in the II requires that all the components be kept under vacuum.

When x-rays first arrive at the II they pass through the input window, a thin aluminum cap that maintains the vacuum but also attenuates some of the x-rays. After passing through the input window the x-rays reach the input phosphor. The most common input phosphor for IIs is thallium-doped cesium iodide (CsI:Th) which, as the name implies, converts incoming x-rays into visible light. Cesium iodide is a common phosphor for x-ray detection because its attenuation properties enable high efficiency while maintaining a relatively thin phosphor. Thin phosphors are preferred because the visible light signal can spread laterally within the phosphor causing the image to become slightly blurred. Cesium iodide is also preferred because the crystals can be grown in

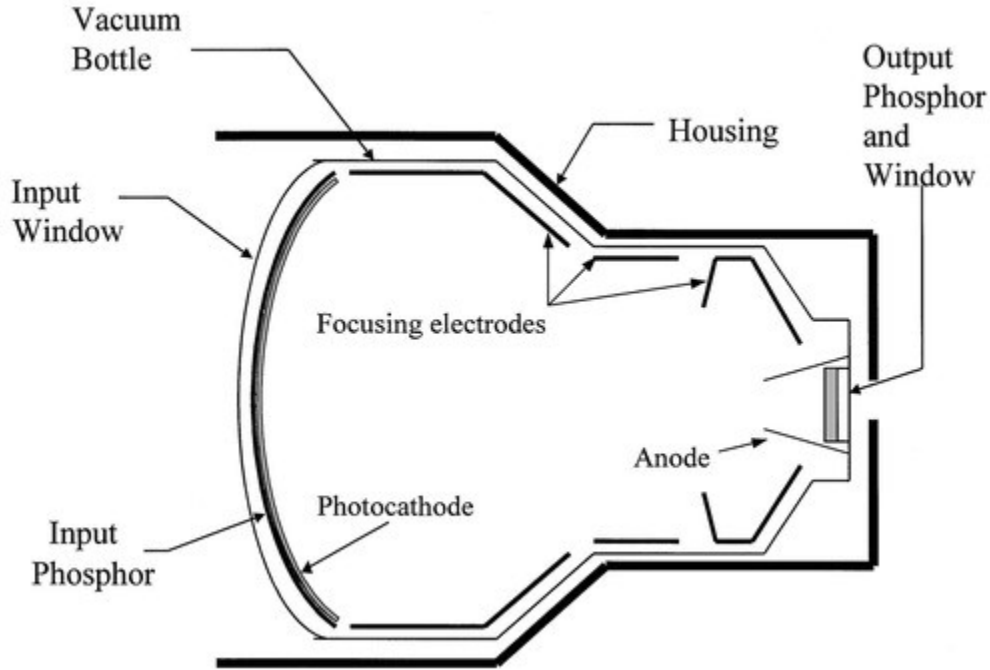


Figure 1.1: Diagram of image intensifier's structure (Source: The AAPM/RSNA Physics Tutorial for Residents).

columnar structures that can act as light pipes, further reducing the lateral spread of visible light signals. Each x-ray interaction within the phosphor layer generates thousands of visible light photons proportional to the energy of the x-ray.

In order to further amplify the original signal, the phosphor layer is followed by a photocathode. The photocathode converts incident light photons to electrons which are then accelerated across a vacuum towards an anode through a potential difference of 25-35 kV. To maintain the same signal pattern from the input x-rays, focusing electrodes are used to guide the electrons towards an anode, minimizing the pattern as the electrons are accelerated. The accelerated electrons bombard a second phosphor layer (typically ZnCdS) which converts the electrons back into visible light. Due to the increased kinetic energy of electrons across the vacuum, each electron interaction results in thousands of light photons, further amplifying the initial signal. These photons then exit through an output window optically coupled to a camera before being passed to a display.

There is a large difference between the size of the input phosphor and the output phosphor allowing for a third stage of signal amplification known as minification. The magnitude of mini-

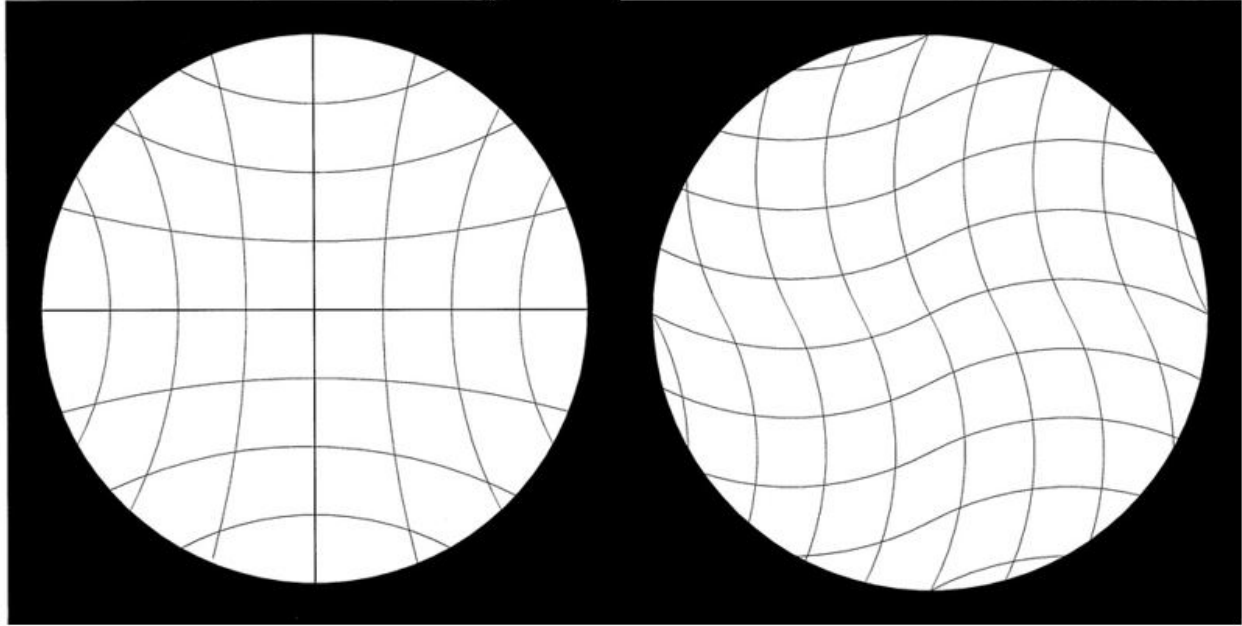


Figure 1.2: Images depicting the pincushion distortion (left) and S distortion (right), two artifacts that image intensifiers are susceptible to (Source: The AAPM/RSNA Physics Tutorial for Residents).

ification gain can be adjusted by changing the field size at the input phosphor and adjusting the focusing electrodes to create an apparent magnification of an image. The greater the image magnification, the lower the minification gain. The product of each of these amplifications give a total system gain.

The nature of the image intensifier system makes it susceptible to a couple artifacts. First, and most notably, the pincushion effect is when an image becomes warped around the edges due to the curved geometry of the input phosphor and the flat output phosphor. Second, the S distortion in which stray magnetic fields affect the electronic lensing within the image intensifier creating random distortions dependent on the magnetic field strength and orientation (see figure 1.2).¹⁷

1.4.2 Flat Panel Detectors

Flat panel Thin-Film Transistor array detectors (FPDs) come in two major varieties: indirect and direct detectors. The difference between the two types of detectors is the layer where x-ray interactions occur. In a direct detector a semiconductor material interacts directly with incident radiation

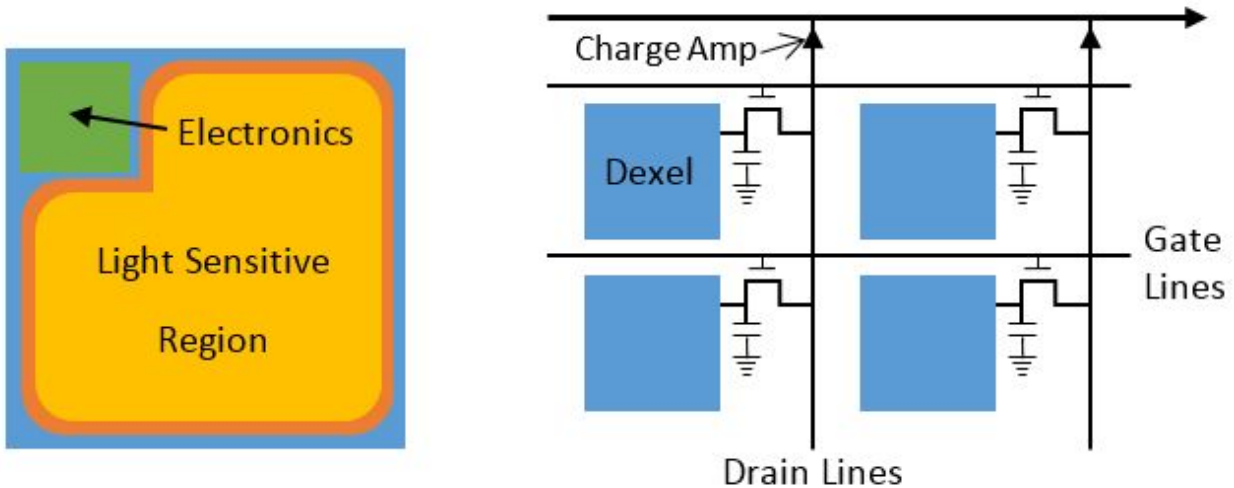


Figure 1.3: Diagrams of an individual dexel (left) and the circuitry for a TFT flat panel system (right).

to produce electron-hole pairs in proportion to x-ray energy and intensity. Electrodes collect the electron-hole pairs and apply a voltage bias to prevent lateral movement of charge in the semiconductor. An indirect detector uses a scintillation layer (typically CsI) to convert x-rays to visible light, proportional to x-ray energy and intensity. The visible light is collected by a light sensitive array optically coupled to the back of the scintillation layer. In contrast to the direct detector, an indirect detector has some blurring of the initial signal due to lateral movement of the visible light in the scintillator.

In both direct and indirect detectors, the interacting layer is backed by an array of electronics that collects and stores signal until individual detector elements (dexels) are read out. Each dexel contains a charge collection electrode and capacitor for storage. These dexels are organized in rows and columns with a thin film transistor (TFT) composed of a gate, source and drain that control dexel readout. The electronic components take up some of the dexel area giving a “fill-factor” (ratio of sensitive to insensitive region of the dexel) less than one (figure 1.3).¹⁸

FPDs are not subject to the same distortions and artifacts as IIs. Furthermore, the lack of a vacuum envelope enables thinner, less dense materials to be used to cover the FPDs scintillator, which reduces the attenuation of the FPD’s housing. FPDs digital nature also allows for greater flexibility when binning or interpolating pixels to provide the adequate balance between image

resolution and noise. These advantages among others have made FPDs the technology of choice in most modern interventional suites.

1.5 Region of Interest Imagers

Though endovascular interventions provide a minimally invasive alternative to other procedures, they do face challenges. One of the greatest obstacles to overcome is the visualization of the details of patient anatomy and the fine featured instruments used in the treatment. Such visualization is necessary not only for performing a procedure, but also for assessing the success or failure of a treatment.

An interventionalist's visualization at the site of an intervention can be improved through use of a smaller field of view, high-resolution detector. These high-resolution detectors (or ROI detectors) provide two benefits: improved visualization of fine details that may improve chances for treatment success, and sparing of surrounding skin as dose is confined to the site of the treatment during use of high-resolution detector.

There are currently two designs in use for ROI detectors: a separate detector that can be moved in and out of the x-ray field with a mechanical changer arm, and an integrated detector built-in to the standard FPD. The separate detector can be added to any current c-arm system, but the x-ray field must be collimated to the ROI detector, typically requires a separate imaging chain for displaying images, and does require a small amount of time to deploy. The integrated detector can only be added to compatible c-arm systems, but once added is fully integrated into the preexisting imaging chain allowing the field of view to be automatically collimated, and can be activated instantly simply by pressing a button. Figure 1.4a shows a high-resolution ROI detector that can be mounted to any c-arm and figure 1.4b shows an integrated detector with both large FOV standard resolution and small FOV high-resolution capabilities. Note that the integrated detector would be indistinguishable from a standard FPD detector.



(a)



(b)

Figure 1.4: Examples of ROI detectors showing a detector to be mounted to a c-arm (a) and one integrated into a c-arm (b) (Source: Canon Medical Systems).

1.6 Present Work

Chapter 2 presents a comparison of the two modes of a new integrated ROI detector by assessing detector performance through use of detector metrics. The metrics used compare spatial resolution (MTF), noise performance (NNPS) and the general performance of an imaging system (DQE). A direct comparison of the two imaging modes is made using a family of metrics known as the Relative Object Detectability (ROD) metric.

Chapter 3 continues the work of chapter 2 by comparing the performance of a high-resolution ROI detector with and without an anti-scatter grid in place. Anti-scatter grids are used to improve image signal to noise ratio by preventing scatter from reaching the detector surface, but the grids also attenuate some of the primary beam. To offset the attenuation of the primary beam the exposure to the patient is increased. The ROI detector has a smaller field of view and therefore imaging has reduced scatter. To assess the impact of the grid on image quality the DQE is measured for the ROI detector with and without the grid in place and ROD metrics are calculated for both scenarios

as well.

Chapter 4 begins by deriving the magnitude of image blurring due to gantry motion. The contribution is found to be significant depending on the location of the feature, the magnitude of the gantry's rotational velocity, and duration of each frame exposure. The magnitude of the blur in individual projection images is then verified experimentally. Blur due to gantry motion is most likely to impact physicians' visualization during acquisition of projections used to reconstruct CBCT images. To investigate the impact of gantry motion blur, projection images were simulated from a pattern phantom and the blurred projections were used to reconstruct images where the blur could then be measured.

In Chapter 5, a new direct detector is introduced. This new detector is capable of operating at up to 1000 fps and is used to image processes in the body that occur at high speed. Among these processes are the movement of the heart (as imaged in animal models) and the movement of blood through vessels (obtained from animal models and 3D printed phantoms). This chapter outlines preliminary works examining how high-speed detectors may be used in the clinic to improve patient treatment, including the effect of deployed interventional devices on the flow of blood in and around a saccular aneurysm.

Chapter 6 continues to build upon the work of chapter 4 by introducing quantitative methods to the examination of flow details. The first portion of this chapter covers methods for quantifying the velocity of blood flow within patient specific models. The following section uses methods similar to techniques used in parametric imaging to evaluate the impact of stenosis of varying degrees on blood flow with patient-specific phantoms.

The final chapter seeks to summarize the individual works examined in each chapter and to discuss the next steps that are expected for these works.

Chapter 2

Comparison of Integrated Detector Modes Through Use of Imaging Metrics Including the Relative Object Detectability (ROD) Family of Metrics

2.1 Introduction

An interventionalist's visualization of fine detail is paramount to the success of a neurovascular image-guided intervention. Factors such as stent wall apposition, the presence of endoleaks, and other details related to the placement of endovascular devices are critical in ensuring optimal patient outcomes. Conventional flat panel detectors (the current standard of care for neurovascular interventions) typically have pixel sizes ranging from 140 to 200 μm ,¹⁹ and lack the spatial resolution to resolve critical details that allow interventionalists to perform a procedure with confidence in the final device placement. The medical physics imaging research group at the University at Buffalo has worked to develop high-resolution, small field of view detectors that can be placed on a mechanical arm to be moved in and out of the x-ray beam as needed by the interventionalist.

These detectors have been used in the clinic for treatment, and studies show that interventionalists prefer the image quality of high-resolution images to standard-resolution images.^{20,21,22}

The same research group that originally developed the high-resolution ROI detectors has continued to collaborate with Canon Medical Systems to produce a new flat panel detector with integrated standard resolution (196 μm pixel pitch) FPD mode and high resolution (76 μm pixel pitch) Hi-Def mode. This new detector has the improved resolution capabilities of previous detectors while also having the convenience of being able to switch detector modes instantly through use of an electronic switch.

It has been shown qualitatively that interventionalists prefer the performance of the Hi-Def mode relative to the FPD mode for images acquired during a simulated neurointerventional procedure.²³ To provide a quantitative comparison of the new Hi-Def mode relative to the performance of the standard FPD mode standard detector metrics were acquired for both detector modes including the detector MTF, NNPs, and DQE. Following the measurement of the standard detector metrics a comparison was made using the generalized metrics (generalized MTF [GMTF], generalized NNPS [G-NNPS], and generalized DQE [GDQE]) which include system factors such as magnification, focal spot blur, and scatter to the detector. Finally, a new family of metrics known as the relative object detectability (ROD) metric, was used to compare the task-based performance of the two detector modes imaging specific objects.

2.2 Materials and Methods

2.2.1 Details of Detector Modes

The flat panel detector from Canon, the new Alphenix Hi-Def Detector, is a unique hybrid detector capable of switching instantly between two detector modes with an electronic switch (see figure 2.1). The two modes provide standard-resolution (FPD mode) for FOVs ranging from 6 to 12 inches and high-resolution (Hi-Def mode) for FOVs ranging from 1.5 to 3 inches. Canon's detector makes use of a single scintillation layer of thallium-doped CsI with a thin film transistor (TFT)

readout coupled to the beam-side of the scintillator and a low-noise CMOS camera coupled to the opposite side. When the FPD mode is activated the TFT readout is used providing 194 μm pixels (2.6 lp/mm). Alternatively, the Hi-Def mode makes use of the CMOS detector with its 76 μm pixels (6.6 lp/mm).



Figure 2.1: Canon's Alphenix detector with integrated Hi-Def and FPD imaging modes (Source: Canon Medical Systems).

2.2.2 Qualitative and Semi-Quantitative Comparisons

To provide a qualitative assessment of the detector performance under clinical conditions a pipeline stent was deployed in a vascular phantom. The pipeline stent is composed of very thin wires the require very high spatial resolution to resolve properly. To simulate imaging conditions during

an interventional procedure a an anthropomorphic head phantom was placed below the vascular phantom with deployed stent and images were acquired using both detector modes in DA mode with small focal spot. The images for the Hi-Def mode and FPD mode were assessed side-by-side for the visibility of stent struts.

For a semi-quantitative comparison of the two detectors a line-pair phantom was placed against the outer face of the detector in both vertical and horizontal orientations. Raw images were acquired using the system's digital angiography (DA) mode with the maximum exposure allowed for the small focal spot. An RQA5 phantom was placed in the beam's path and the anti scatter grid was left in place to mimic clinical circumstances. The images acquired using the FPD and Hi-Def modes were placed side by side on a computer screen and the highest visible line-pair frequency with no sign of aliasing was assessed.

2.2.3 Standard Metrics

The modulation transfer function (MTF) is widely accepted as the gold standard for comparing spatial resolution performance between detectors. Several methods exist for calculating the MTF, but for this experiment, we utilized the slanted edge method.²⁴ In the edge response method a precisely machined tungsten plate surrounded by lead is placed on the detector surface and angled between 1.5° - 3° from the pixel array. An over-sampled edge spread function (ESF) was built from the rows running perpendicular to the machined edge. The angling of the edge allows for the oversampling of the MTF in which the angled edge allows for a sampling pitch much finer than would otherwise be allowed by the detector pixel pitch as in each row of pixels the edge has been slightly shifted.²⁵ The MTF can be calculated from the ESF via the following:

$$MTF = \left| \int \frac{d}{dx} ESF(x) \cdot e^{-2\pi i x f} dx \right| \quad (2.1)$$

Edge images were acquired using a standard RQA5 x-ray spectrum (21 mm of added aluminum filtration at 70 kVp) as recommended in IEC 62220-1²⁶ along both axes of the pixel array. A set

of 150 images were acquired for each orientation using 200 mA at 10 ms technique parameters. The acquired images were dark-field and flat-field corrected before averaging the full sequence to provide a single edge image.

The normalized noise power spectrum (NNPS) is a measurement that not only quantifies the magnitude of noise, but also its “texture.” The NNPS gives a frequency dependent measure of the correlation of noise and is calculated from flat-field images broken up into overlapping regions of 256 x 256 pixels as follows:

$$NNPS = \frac{\Delta x \cdot \Delta y}{\bar{d}^2 \cdot M \cdot 256 \cdot 256} \sum_{m=1}^M \left| \sum_{i=1}^{n_x} \sum_{j=1}^{n_y} (I(x_i, y_j) - \bar{I}) \cdot e^{-\frac{2\pi i x_i y_j f_x f_y}{n_x n_y}} \right|^2 \quad (2.2)$$

where \bar{d} is the average detector output signal, M is the number of ROIs, n_x and n_y are the number of ROI rows and columns respectively, Δx and Δy are the pixel dimensions, $I(x_i, y_j)$ is one of the 256 x 256 pixel regions, and \bar{I} is the same region with pixel values averaged across multiple frames. Flat-field images were also acquired using an RQA5 x-ray spectrum. X-ray pulse length was set to 10 ms and tube current was varied between 50, 100, and 160 mA to vary the exposure per frame (measured at 30.2, 61.3, and 98.2 μ R per frame respectively). Flat-field images were dark-field and flat-field corrected before processing.

The detector’s detective quantum efficiency (DQE) is a measure of the detector systems output signal to noise ratio (SNR) relative the detector’s input SNR and can be calculated from the detector’s MTF and NNPS as follows:

$$DQE(f) = \frac{MTF(f)^2}{\Phi(X) \cdot NNPS(f)} \quad (2.3)$$

where $\Phi(X)$ is the photon fluence ($\frac{quanta}{mm^2}$) for a given detector exposure. Photon fluence was calculated from the air kerma using the IEC conversion factor 30.17 $\frac{photons}{mm^2 \cdot nGy}$ for the RQA5 spectrum.²⁶

2.2.4 Generalized Metrics

Standard metrics neglect to include detrimental effects of the imaging chain such as magnification, focal spot size, and scatter. As a result, the standard metrics give a somewhat idealized result of the detectors performance. A set of generalized metrics have been developed to compare detectors in an imaging chain.^{27,28} The first of these metrics is the generalized modulation transfer function (G-MTF). The G-MTF quantifies the spatial resolution response of a detector system, while also accounting for focal spot blurring, geometric unsharpness due to magnification, and scatter. The G-MTF is defined in equation 2.4.

$$G - MTF(f, \rho, m) = \left\{ (1 - \rho) \cdot MTF_F([m - 1] \cdot f) + \rho \cdot MTF_S(f) \right\} \cdot MTF_D(f) \quad (2.4)$$

where ρ is the scatter fraction m is the magnification, f is the spatial frequency, MTF_F is the focal spot MTF, MTF_S is the scatter MTF, and MTF_D is the detector MTF.

The MTF_F is a measure of blurring due to the finite size of the focal spot and is directly proportional to the magnification of an object. The MTF_F can be measured directly from the modulus of the Fourier transform of an image of a focal spot acquired with the use of a pinhole camera.²⁹ The MTF_S measures the detrimental effect of scatter on the spatial response of the imaging system^{30,31} which is directly proportional to the scatter and tends to dominate the low spatial frequencies.

The G-MTF can further be scaled back to the object plane by including the magnification as shown in equation 2.5.

$$G - MTF(f, \rho, m) = \left\{ (1 - \rho) \cdot MTF_F\left([m - 1] \cdot \frac{f}{m}\right) + \rho \cdot MTF_S\left(\frac{f}{m}\right) \right\} \cdot MTF_D\left(\frac{f}{m}\right) \quad (2.5)$$

The generalized normalized noise power spectrum (G-NNPS) scales the $NNPS_D$ (the detector

NNPS) to the object plane according to equation 2.6.

$$G - NNPS(f, X, m) = \frac{1}{m^2} \cdot NNPS_D\left(\frac{f}{m}, X\right) \quad (2.6)$$

Note that if the magnification goes to 1 (meaning the object is at the detector plane) the expression for G-NNPS becomes equivalent to $NNPS_D$.

Finally the generalized detective quantum efficiency (GDQE) can be calculate from the G-MTF and the G-NNPS:

$$GDQE(f, \rho, X, m) = \frac{G - MTF(f, \rho, m)^2}{\Phi(X) \cdot G - NNPS(f, X, m)} \quad (2.7)$$

where, as before, $\Phi(X, m)$ is the number of quanta per mm^2 scaled from the detector face to the object plane.

2.2.5 Relative Object Detectability Metrics

The standard metrics excel at quantify the detectors response and the generalized metrics provide a mathematical description of the imaging system's response, but neither assess the performance of detectors in task-based tests. The relative object detectability (ROD) metric compares the relative abilities of two detectors to image a simulated object. The noise equivalent quanta (NEQ) gives the frequency dependence of the SNR_{out}^2 for a detector. When the NEQ is convolved with an object image this gives the detector response to the object image, and the integral over spatial all frequencies gives a detectability index for an ideal observer:^{32,33,34}

$$d_{ideal}^2 = \int_{-f_{Nx}}^{f_{Nx}} \int_{-f_{Ny}}^{f_{Ny}} |OBJ(f_x, f_y)|^2 \cdot NEQ(f_x, f_y) df_x df_y \quad (2.8)$$

where f_{Nx} and f_{Ny} are the Nyquist frequencies in the x and y directions respectively, and $OBJ(f_x, f_y)$ is the Fourier transform of an object image. The $OBJ(f_x, f_y)$ is computed from the position-dependent signal differences relative to background for a simulated object (see equation 2.10) as in equation 2.9:

$$OBJ(f_x, f_y) = \int \int obj(x, y) \cdot e^{-2\pi i(xf_x + yf_y)} dx dy \quad (2.9)$$

$$obj(x, y) = \frac{background - signal}{background} = \frac{N_0 - N_0 e^{-\mu \cdot t(x, y)}}{N_0} = 1 - e^{-\mu \cdot t(x, y)} \quad (2.10)$$

where $obj(x, y)$ is the object function in real space, N_0 is the initial photon flux, μ is the linear attenuation coefficient of the object, $t(x, y)$ is the position-dependent object thickness, and $OBJ(f_x, f_y)$ is the object function defined in frequency space. Figure 2.2a is an example of an $obj(x, y)$ function for an aluminum sphere and its corresponding $OBJ(f_x, f_y)$ function is shown in figure 2.2b.

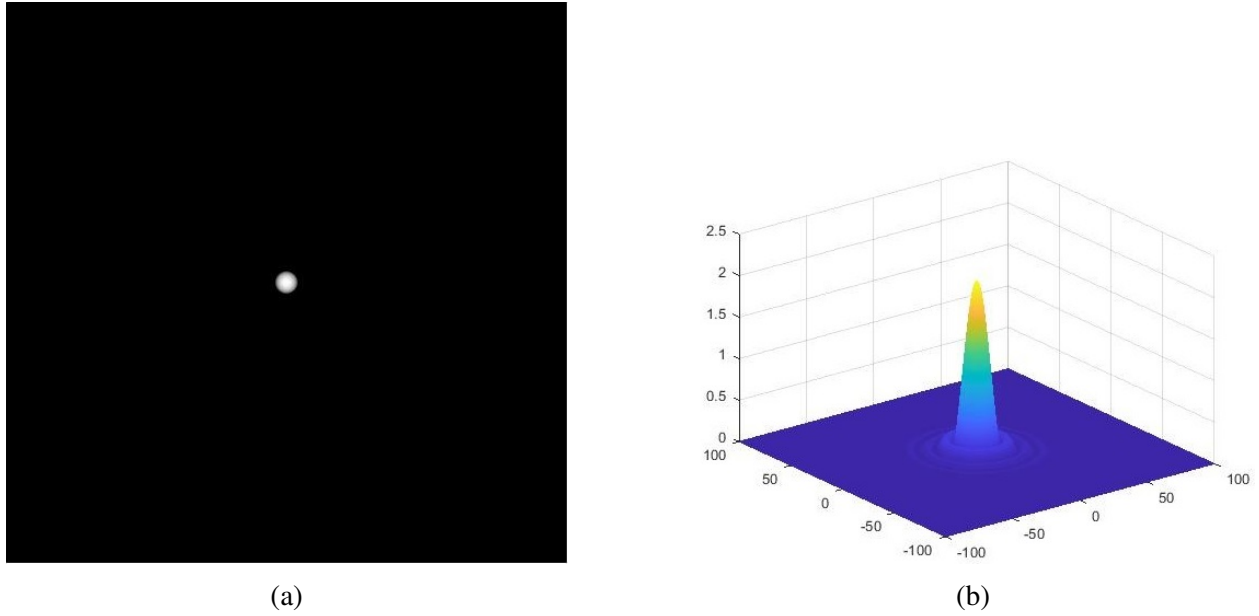


Figure 2.2: Examples of (a) $obj(x, y)$ and (b) $OBJ(f_x, f_y)$ for an aluminum sphere.

By replacing the NEQ in equation 2.8 with the DQE the efficiency of the detectability relative to the input signal to noise ratio squared can be quantified.³⁵ The ROD then can then be calculated by taking the ratio of this quantity for two different detectors with a specified object giving the relative performance of the two detectors for a specific object detection task.³⁵

$$ROD = \frac{\int_{-f_{Nx}}^{f_{Nx}} \int_{-f_{Ny}}^{f_{Ny}} |OBJ(f_x, f_y)|^2 \cdot DQE_1(f_x, f_y) df_x df_y}{\int_{-f_{Nx}}^{f_{Nx}} \int_{-f_{Ny}}^{f_{Ny}} |OBJ(f_x, f_y)|^2 \cdot DQE_2(f_x, f_y) df_x df_y} \quad (2.11)$$

The generalized metrics can alternatively be used in the ROD equation to create a new metric known as the generalized-ROD^{36,37} (G-ROD). The G-ROD is mathematically defined in equation 2.12.

$$G - ROD = \frac{\int_{-f_{Nx}}^{f_{Nx}} \int_{-f_{Ny}}^{f_{Ny}} |OBJ(f_x, f_y)|^2 \cdot GDQE_1(f_x, f_y) df_x df_y}{\int_{-f_{Nx}}^{f_{Nx}} \int_{-f_{Ny}}^{f_{Ny}} |OBJ(f_x, f_y)|^2 \cdot GDQE_2(f_x, f_y) df_x df_y} \quad (2.12)$$

Substituting the standard metrics for the generalized metrics in equation 2.11 allows for the inclusion of detrimental effects in the imaging chain (scatter, geometric unsharpness due to magnification, and focal spot blur). This substitution allows for a task-based comparison of detector systems' detection ability for specified objects.

The final metric used for comparison in this work is the generalized-measured-ROD^{35,38} (GM-ROD). The GM-ROD metric provides greater flexibility to comparing detector systems on the basis of images acquired of real objects for detector systems. Given that the acquired image contains both the object function (given by the object in the detector field of view and the x-ray spectrum's energy and fluence) convolved with the generalized-MTF (which describes the detector response and the blurring effects introduced into the imaging chain) this removes the need to acquire the G-MTF for an array of exposure conditions and simulate objects for comparison. Furthermore, since the objects are real it allows for comparison of more complex geometries, such as flow-diverting stents, that would be difficult to simulate realistically. Since the image includes the obj function and the G-MTF, the GM-ROD can be calculated with just the object image and the G-NNPS as shown in equation 2.13.

$$GM - ROD = \frac{\int_{-f_{Nx}}^{f_{Nx}} \int_{-f_{Ny}}^{f_{Ny}} \frac{|OBJ_1(f_x, f_y)|^2}{G-NNPS_1(f_x, f_y)} df_x df_y}{\int_{-f_{Nx}}^{f_{Nx}} \int_{-f_{Ny}}^{f_{Ny}} \frac{|OBJ_2(f_x, f_y)|^2}{G-NNPS_2(f_x, f_y)} df_x df_y} \quad (2.13)$$

The $OBJ_N(f_x, f_y)$ in equation 2.13 refers to the Fourier transform of the object images ac-

quired on detector 1 or 2. These object images are low noise images (produced by averaging a large number acquired images) to reduce the impact of noise on the object function and G-MTF built into the object images. The image was then inverted by subtracting the original image from the average background image, making the object in the image the source of the digital signal.

Further analysis of the GM-ROD was performed by varying the integration bounds. Changing integration bounds for the GM-ROD metric allows for a comparison of different features in the object image. This enables a comparison of a detector system's ability to image object detail by focusing on the high spatial frequencies (where most image detail is contained) instead of the low spatial frequencies (where the general shape of an image is contained). For example, figure 2.3a is an image of a flow diverting stent acquired using the Hi-Def detector and figure 2.4b shows the $OBJ(f_x, f_y)$ for the same stent image. If only spatial frequencies above $1 \frac{lp}{mm}$ are kept (see figure 2.4b for the corresponding $OBJ(f_x, f_y)$), then the image is reduced to almost only the stent strut details that is shown in figure 2.3c. Conversely, the image corresponding to only the low spatial frequencies ($0 \frac{lp}{mm}$ to $1 \frac{lp}{mm}$) is shown if figure 2.3b and contains almost no stent strut detail.

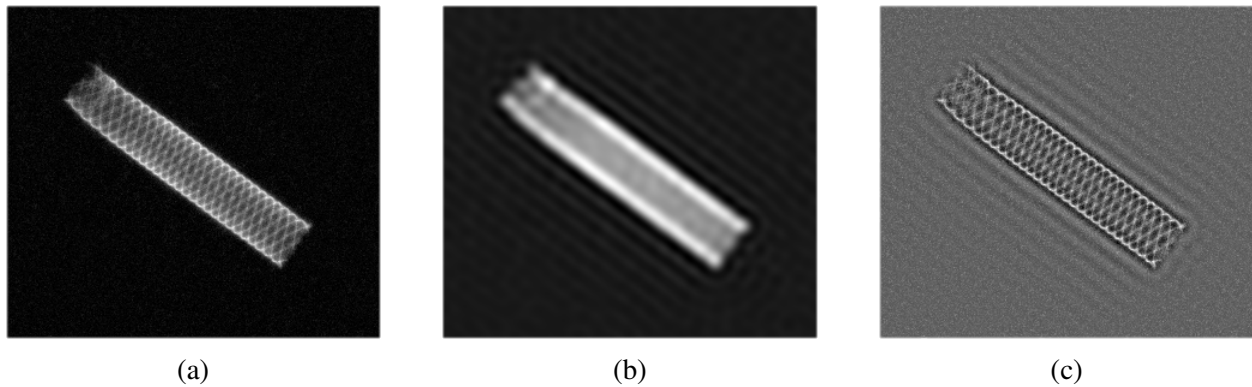


Figure 2.3: Examples of how changing the $OBJ(f_x, f_y)$ function impacts the resultant image with (a) containing all image data for $OBJ(f_x, f_y)$, (b) containing image data from $0 \frac{lp}{mm}$ to $1 \frac{lp}{mm}$, and (c) containing image data from $1 \frac{lp}{mm}$ to the Nyquist.

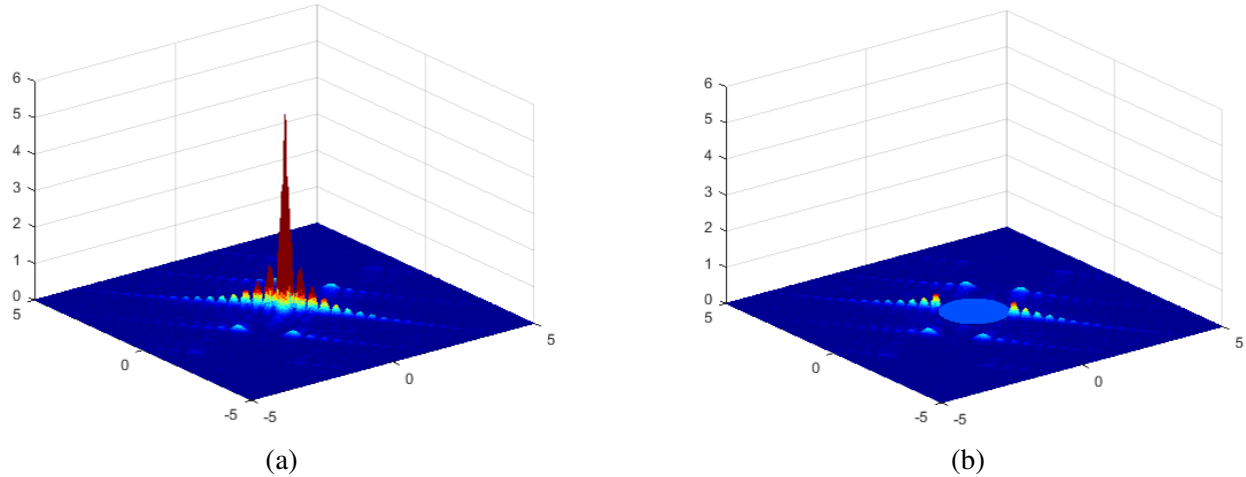
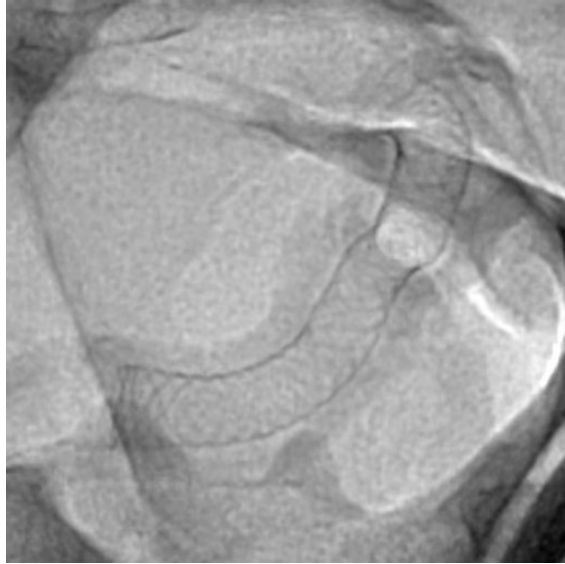


Figure 2.4: Stent $OBJ(f_x, f_y)$ function showing (a) all of frequency space and (b) frequency space from $1 \frac{lp}{mm}$ to the Nyquist.

2.3 Results

2.3.1 Qualitative and Semi-Quantitative Comparisons

Figures 2.5 and 2.6 are example images captured using both detector modes operating in digital angiographic mode. The devices shown are pipeline stents deployed in vascular phantoms. It can clearly be seen from the two figures that the Hi-Def mode (shown in figure 2.5b and 2.6b) has improved imaging performance over the FPD mode (shown in figure 2.5a and 2.6a). The comparison is the first qualitative comparison of the performance of the two detector modes and was an important first step in assessing performance.

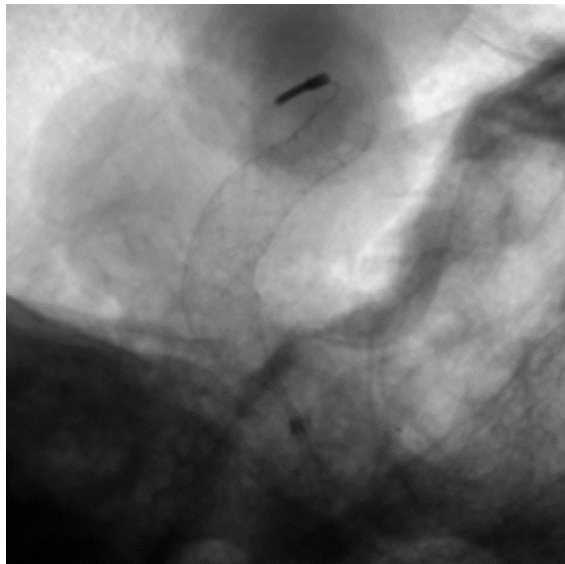


(a)

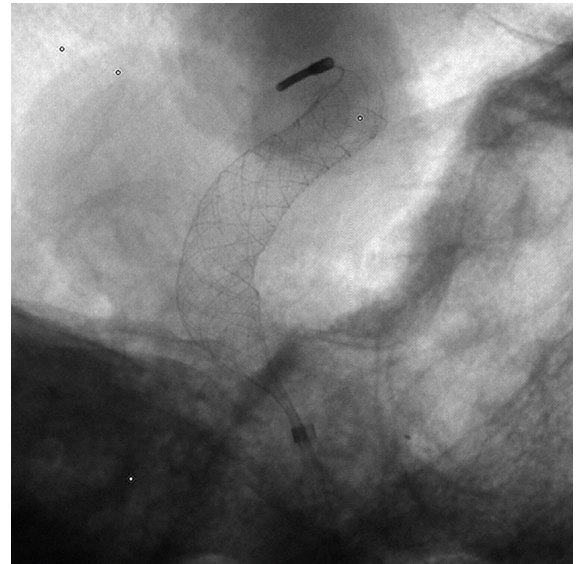


(b)

Figure 2.5: Images acquired of a pipeline stent deployed in a vascular phantom using (a) the new detector's FPD mode and (b) the new detector's Hi-Def mode.



(a)



(b)

Figure 2.6: Images acquired of pipeline stent deployed in a vascular phantom using (a) the new detector's FPD mode and (b) the new detector's Hi-Def mode.

For a semi-quantitative comparison figure 2.7 shows a comparison of line-pair phantoms acquired using both FPD (figure 2.7a) and Hi-Def (figure 2.7b) modes. Images were acquired with the line-pair phantom oriented both vertically and horizontally, but for conciseness only the vertical

images are shown here.

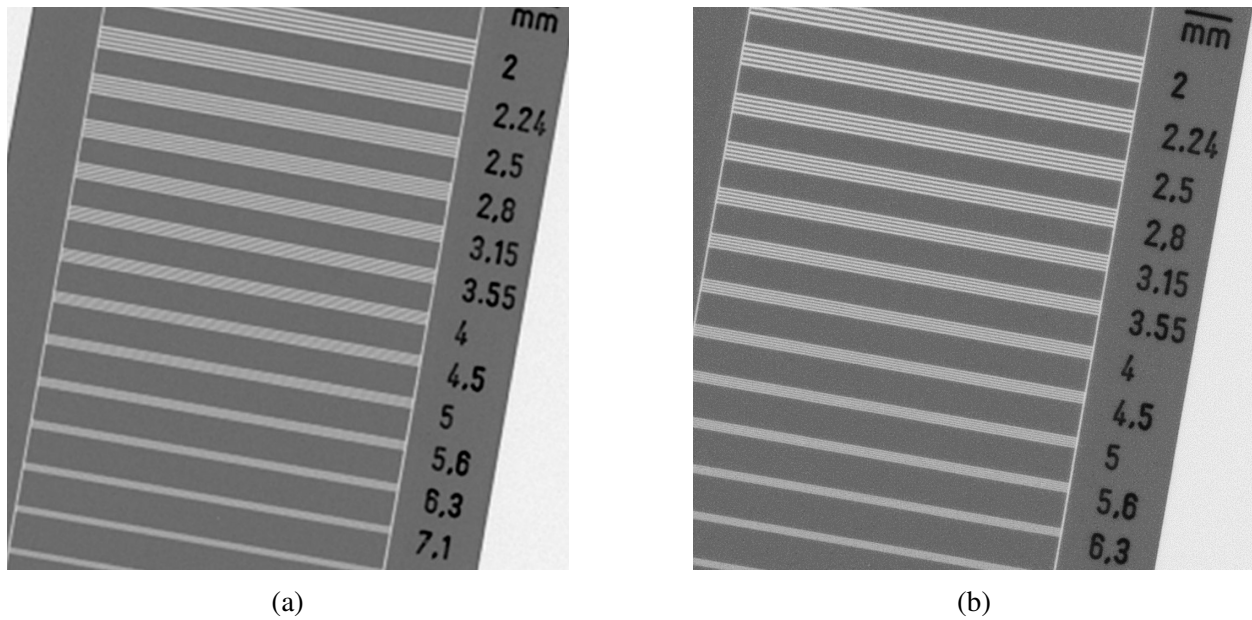


Figure 2.7: Images acquired of a deployed pipeline stent in a vascular phantom using (a) the new detector's FPD mode and (b) the new detector's Hi-Def mode.

The line pair phantoms were assessed by two users who determined maximum number of line pairs that could be resolved from the image without aliasing. The Hi-Def mode demonstrated superior imaging capabilities relative to the FPD mode and the full results of the test are shown in table 2.1.

	FPD Zoom Mode		Hi-Def Zoom Mode		
Mag Mode	3.3 inch	2.5 inch	3.0 inch	2.3 inch	1.5 inch
Vertical (lp/mm)	2.24	2.24	5.6	5.6	6.3
Horizontal (lp/mm)	2.24	2.24	5.6	5.6	6.3

Table 2.1: Evaluation of line-pair detector resolution in various detector modes

2.3.2 Standard Metrics

The MTF for the FPD and Hi-Def modes of the Alphenix detector has previously been measured and reported by this group³⁹ and are plotted in figure 2.8. The Hi-Def outperforms the FPD detector

at all spatial frequencies. In the figure it is also clear that the smaller pixel size of the Hi-Def mode not only enables the imaging of higher spatial frequencies that would otherwise be aliased by the FPD zoom mode.

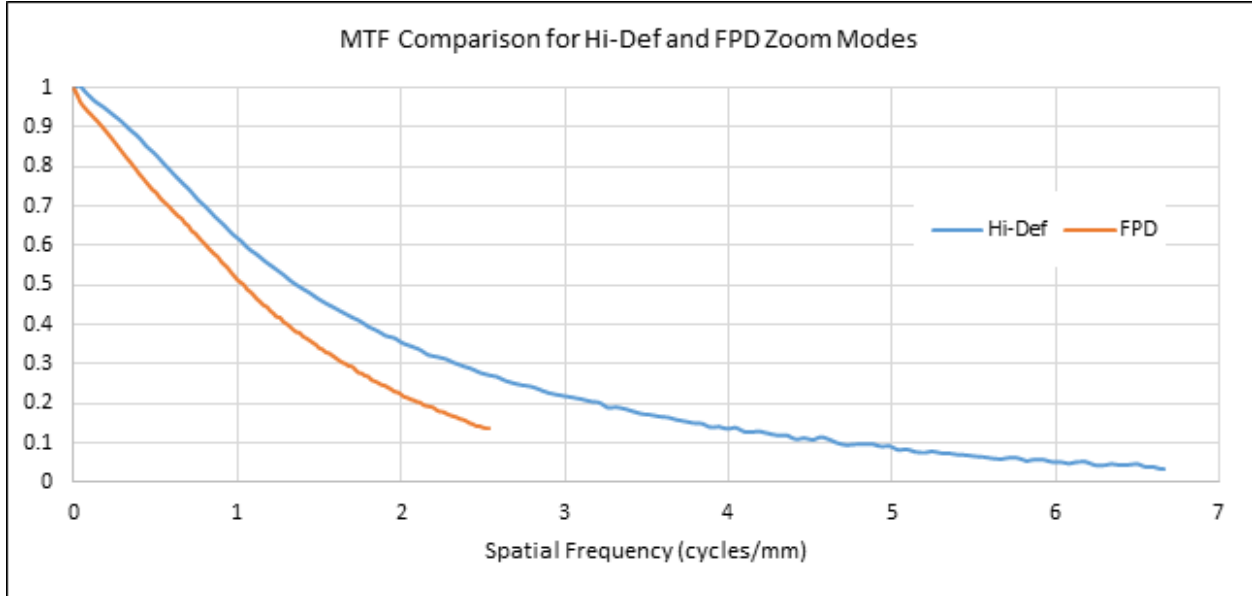


Figure 2.8: Plot of the MTF for Hi-Def and FPD zoom modes.

The NNPS for the FPD and Hi-Def zoom modes of the Alphenix detector has also been measured and are reported here (see figure 2.9). The plot shows that for low exposures the FPD has lower noise than the Hi-Def zoom mode, due to the larger pixel size of the FPD zoom mode. An images quantum noise is equal to \sqrt{N} , where N is the number of detected events, under most circumstances. Since the NNPS was measured for both the Hi-Def and FPD zoom modes using the same spectrum and the same technique parameters the exposure at the detector surface is the same, and since photon fluence is proportional to exposure⁴⁰ the number of quanta detected per pixel is directly proportional to pixel area. As exposure increases, however, the noise is reduced for both detectors and they approach similar performance.

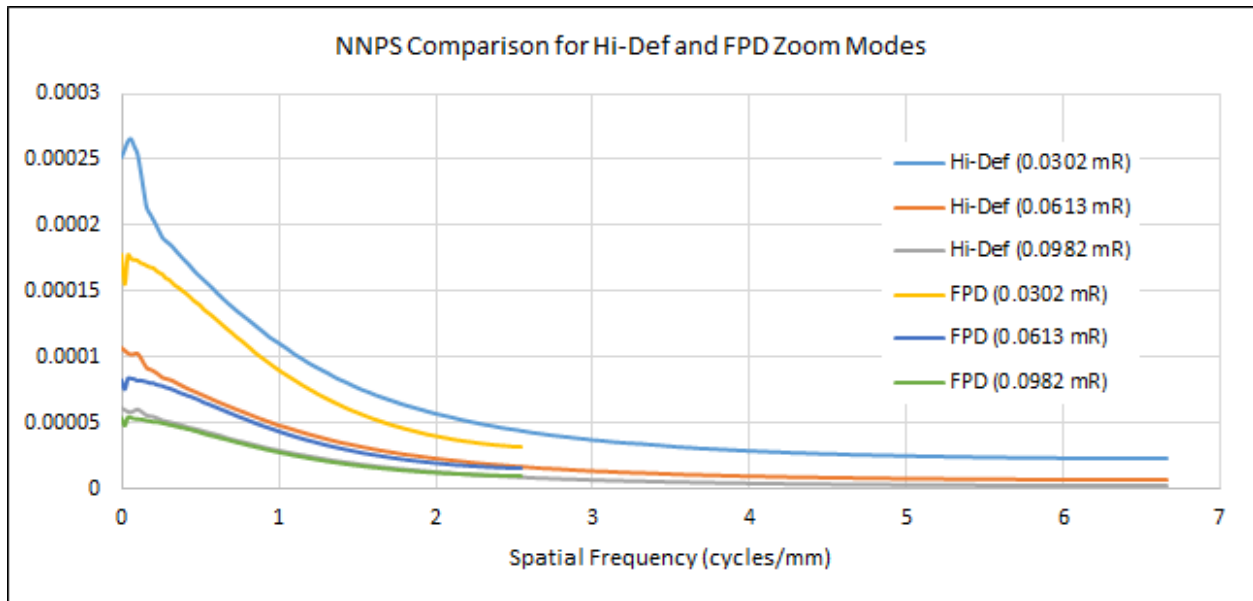


Figure 2.9: Plot of the NNPS for Hi-Def and FPD zoom modes.

The DQE for the FPD and Hi-Def zoom modes of the Alphenix detector were calculated from the MTF and NNPS and have previously been reported by this group³⁹ (see figure 2.10). For this plot the NNPS for the highest exposure level, 98.2 μR , was used. In the plot it can be seen that the Hi-Def zoom mode outperforms the FPD zoom mode at all but the very lowest of spatial frequencies. This is owed principally to higher MTF of the Hi-Def mode across all spatial frequencies. Further, the Hi-Def zoom mode has much higher performance in the high spatial frequency range where, as discussed above, the image detail resides.

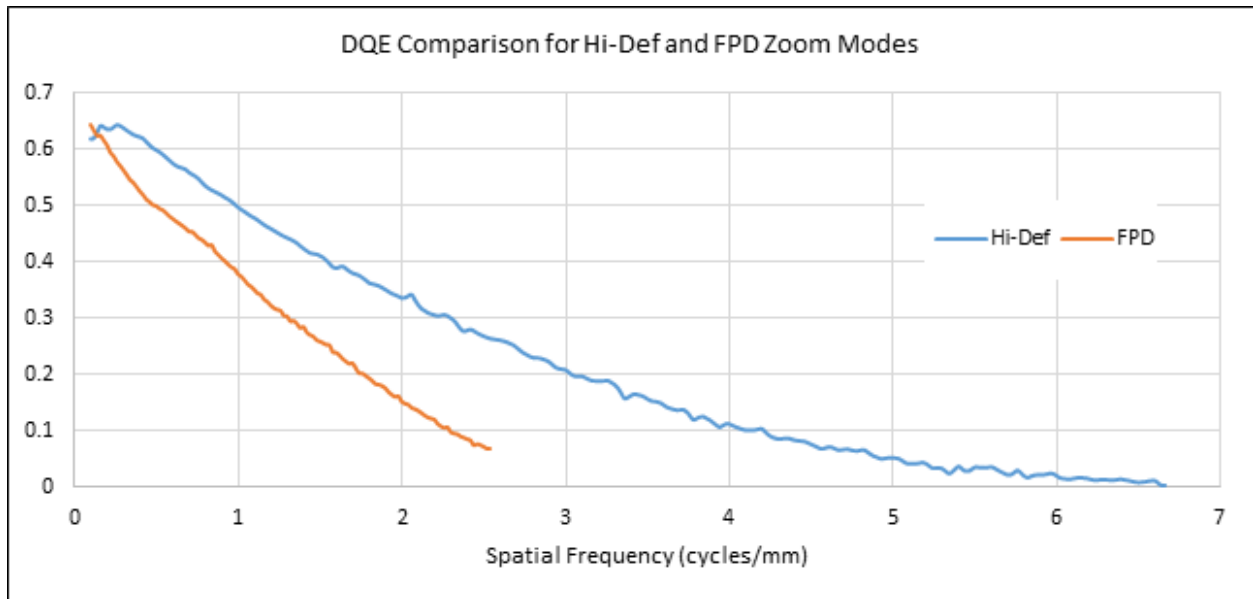


Figure 2.10: Plot of the DQE for Hi-Def and FPD zoom modes.

2.3.3 Generalized Metrics

The G-MTF for the FPD and Hi-Def modes of the Alphenix detector has previously been measured and reported by this group.³⁹ The G-MTF has been measured for a variety of magnifications and scatter fractions ranging from 1.05x to 1.40x magnification and 0.34 to 0.62 scatter fraction. Due to limitations in space the G-MTFs for scatter fraction 0.34 with magnifications of 1.05x and 1.40x only are displayed in figures 2.11 and 2.12 respectively. The Hi-Def outperforms the FPD mode at all spatial frequencies under both conditions displayed in the plots. At low spatial frequencies the detectors have very similar performance due to scatter, and increases in magnification reduce the advantage of the Hi-Def due to geometric unsharpness.

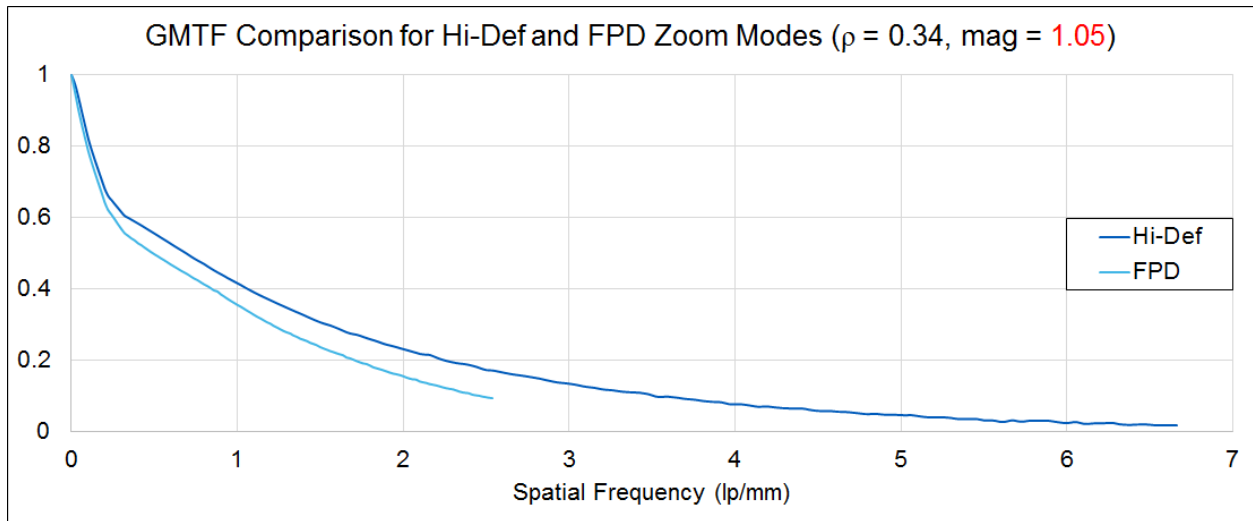


Figure 2.11: Plot of the G-MTF for Hi-Def and FPD zoom modes ($\rho = 0.34$, $\text{mag} = 1.05$).

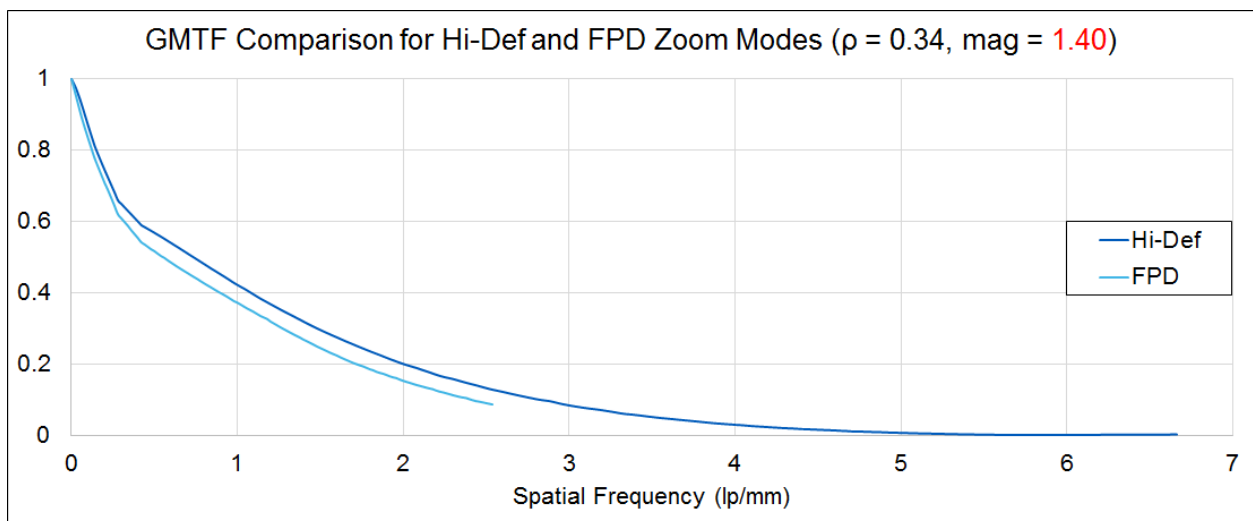


Figure 2.12: Plot of the G-MTF for Hi-Def and FPD zoom modes ($\rho = 0.34$, $\text{mag} = 1.40$).

Given that the G-NNPS is primarily a scaling of the NNPS to the object plane through use of the factor $\frac{1}{m}$ it is not here reported, though it is used in the calculation of the GDQE.

The GDQE for the FPD and Hi-Def modes of the Alphenix detector has previously been measured and reported by this group.³⁹ The GDQE has been measured for a variety of magnifications and scatter fractions ranging from 1.05x to 1.40x magnification and 0.34 to 0.62 scatter fraction. Due to limitations in space the GDQEs for scatter fraction 0.34 with magnifications of 1.05x and 1.40x only are displayed in figures 2.13 and 2.14 respectively. The Hi-Def outperforms the FPD

mode at all spatial frequencies under both conditions displayed in the plots. At low spatial frequencies the detectors have very similar performance due to scatter (just like in the G-MTF plots), and increases in magnification reduce the advantage of the Hi-Def due to geometric unsharpness with almost all gains lost for the highest magnification.

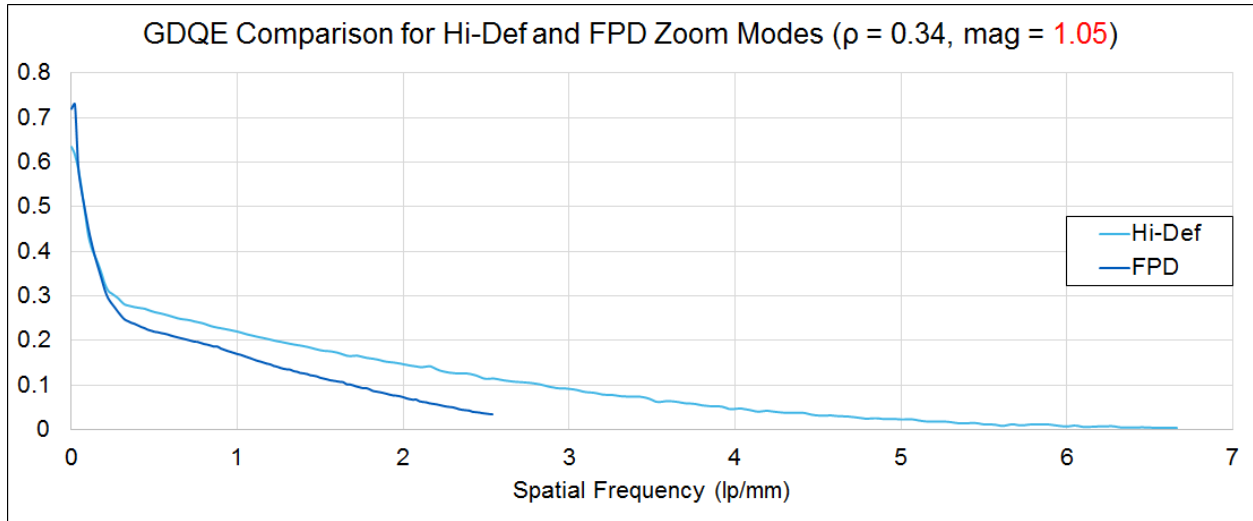


Figure 2.13: Plot of the GDQE for Hi-Def and FPD zoom modes ($\rho = 0.34$, mag = 1.05).

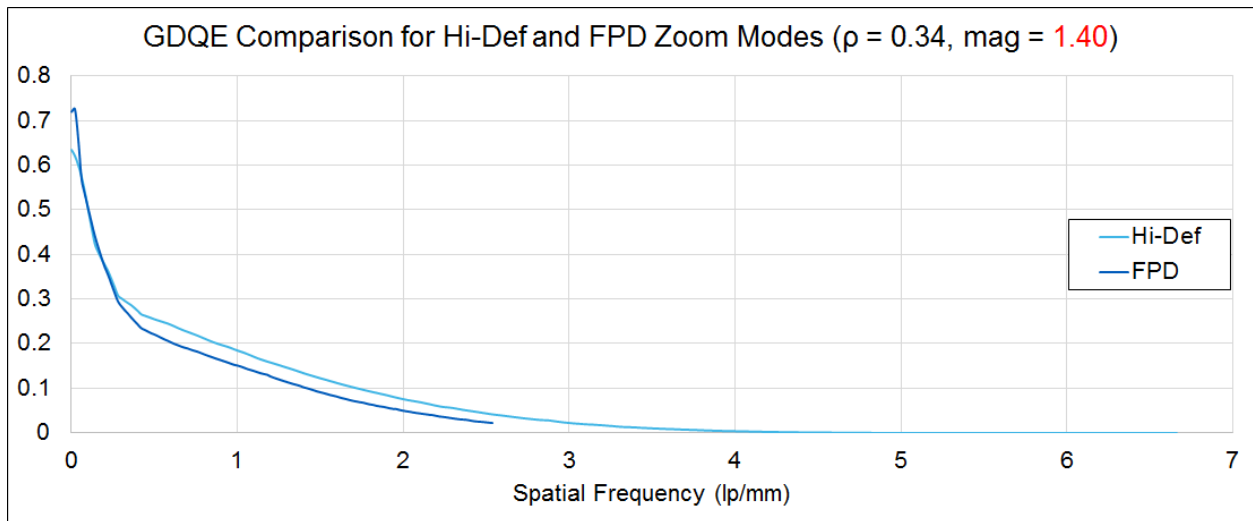


Figure 2.14: Plot of the GDQE for Hi-Def and FPD zoom modes ($\rho = 0.34$, mag = 1.40).

2.3.4 ROD Metrics for Hi-Def Relative to FPD Mode

The ROD family of metrics makes task-based comparisons of detectors and detector systems using both simulated and real objects. Previously simulated object functions have included spheres, wires, iodinated vessels, discs, and cubes.^{35,37,41,42} For the purposes of this paper the only simulated objects to be presented are spheres, wires, and discs.

ROD Metric Results

The task-based performance of the Hi-Def zoom mode was compared to the FPD zoom mode based on the frequency dependent signal to noise performance of the detectors quantified in the DQE. The imaging task used for the ROD comparison was simulated spheres, discs, and wires with diameters ranging from 50 μm to 2 mm.³⁹ The results of the comparison are shown below in figure 2.15.

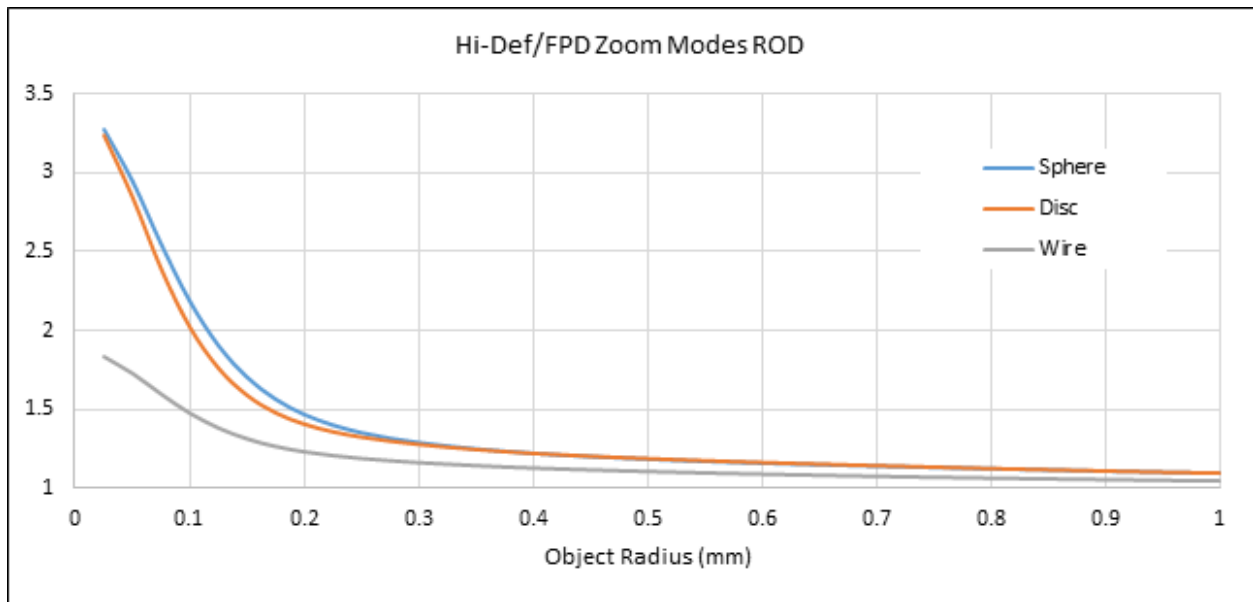


Figure 2.15: Plot of the ROD metric for Hi-Def and FPD zoom modes for spheres, discs, and wires.

The plot demonstrates the superior performance of the Hi-Def zoom mode relative to the FPD mode, especially for spheres and discs of small diameter (50 to 300 μm), with the Hi-Def mode

outperforming the FPD mode by a factor 3.25 for the smallest objects. Spheres and discs had similar performance since the objects have similar profiles and therefore produce similar $OBJ(f_x, f_y)$ functions. The ROD value for the wire is lower than for the spheres and discs due to differences in the $OBJ(f_x, f_y)$ function, namely a higher value for the function in the lower spatial frequencies due to the length of the wire as is shown in figure 2.16. The length of the wire enables improved detectability even for the larger pixel size of the FPD zoom mode, though the Hi-Def still outperforms the FPD mode by a factor of 1.8 for the smallest objects. As object diameter increases, the ROD value approaches unity due to the majority of the spatial information being confined to the low spatial frequencies.

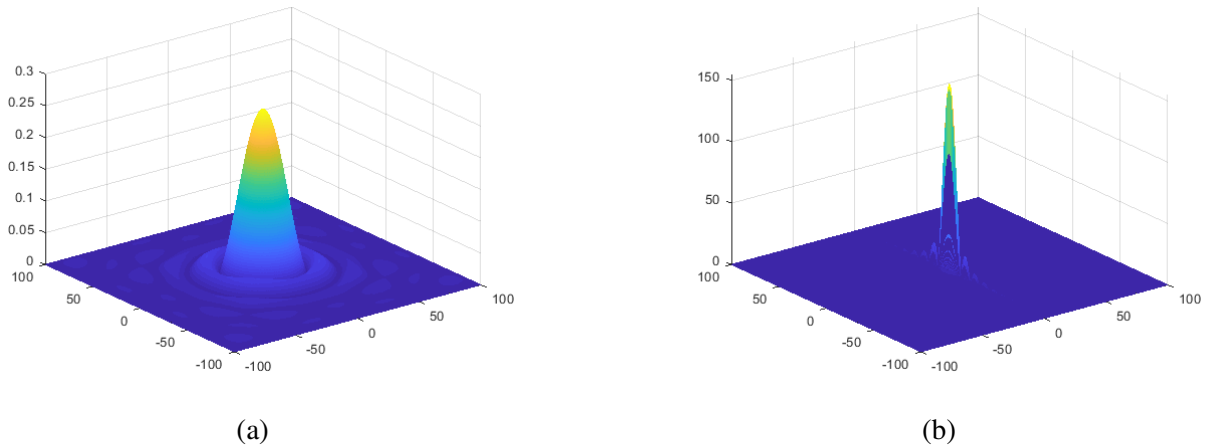


Figure 2.16: $OBJ(f_x, f_y)$ function for a 50μ diameter (a) sphere and (b) wire.

G-ROD Metric Results

The relative task-based performance of the Hi-Def and FPD zoom modes once included in an imaging chain was also measured for the same simulated objects and has been reported on by this group.³⁹ The results of the G-ROD for the Hi-Def relative to the FPD are show below in figures 2.17 and 2.18 for magnification factors of 1.05 and 1.40 respectively.

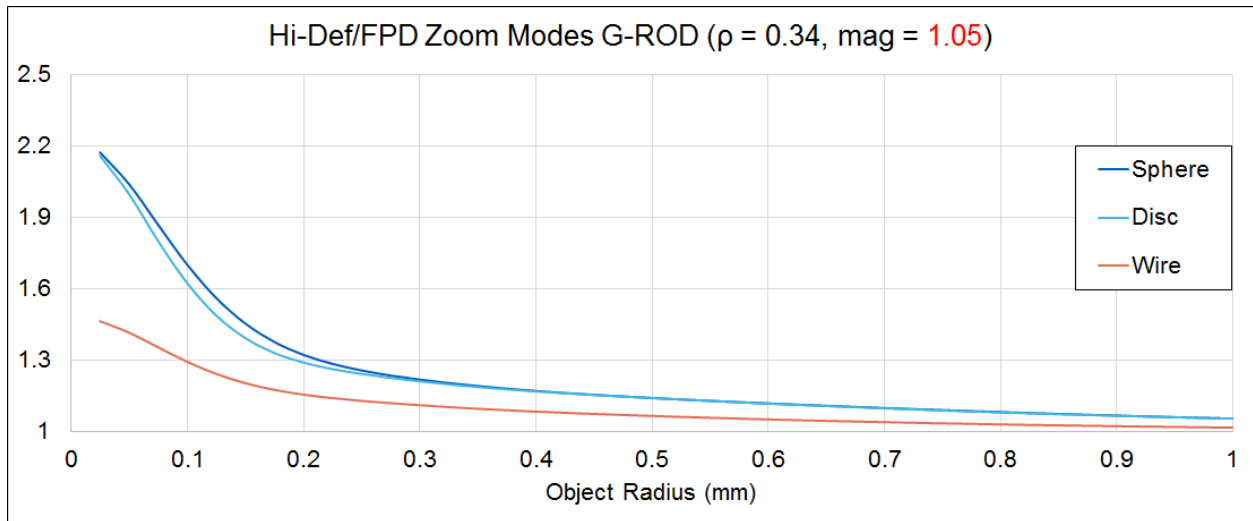


Figure 2.17: Plot of the G-ROD metric for Hi-Def and FPD zoom modes for spheres, discs, and wires.

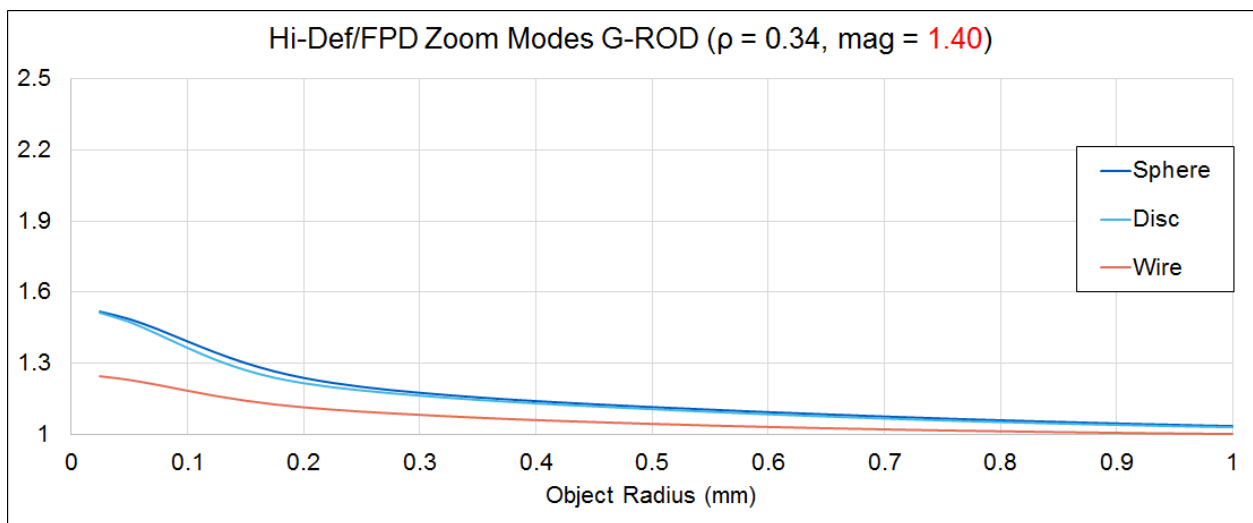


Figure 2.18: Plot of the G-ROD metric for Hi-Def and FPD zoom modes for spheres, discs, and wires.

Once again the plot shows the improved object detectability of the Hi-Def mode over the FPD mode. For the 1.05 magnification factor the Hi-Def had nearly 2.2 times the performance of the FPD mode for discs and spheres of 50 μm diameter and nearly 1.5 times the performance of the FPD mode for wires of 50 μm diameter. Increasing the magnification factor to 1.40 greatly reduces the performance of the Hi-Def mode relative to the FPD mode for small objects due to magnification blurring, with the Hi-Def achieving just over 1.5 times the performance of the FPD

mode for discs and spheres of 50 μm diameter and nearly 1.25 for wires of 50 μm diameter.

GM-ROD Metric Results

The GM-ROD was calculated using a pipeline stent centered in the FOV. Figure 2.19 shows the two views of the pipeline stent imaged with the FPD zoom mode (figure 2.19a) and imaged with the Hi-Def zoom mode (figure 2.19b) both images were acquired at 1.10x magnification using an RQA5 spectrum. Following acquisition the images were cropped to the same spatial dimensions. The images below qualitatively show an improvement in image quality for the Hi-Def zoom mode given that the stent struts are more clearly visible.

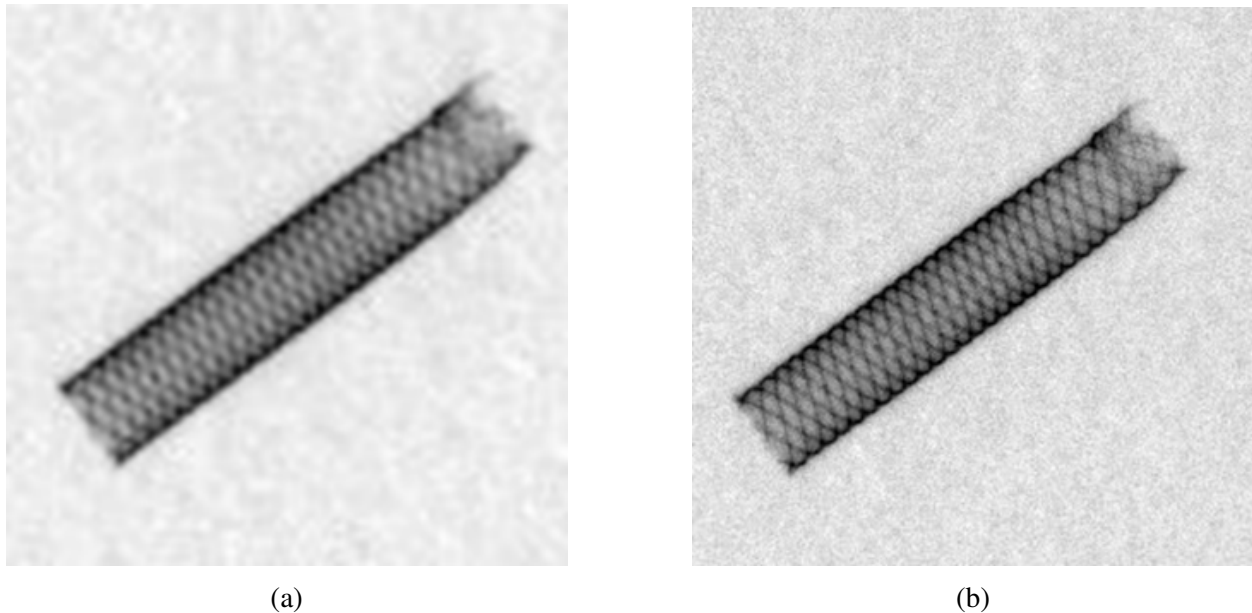


Figure 2.19: Stent images acquired using (a) the FPD zoom mode and (b) the Hi-Def zoom mode.

After acquisition and cropping, the images were inverted so the image signal came from the stent object only. The images shown in figure 2.20 are the same images shown in figure 2.19 after subtracting the image from background. Following subtraction from background the images were converted to frequency space and then divided by the G-NNPS of the corresponding detector at each spatial frequency. The results were then integrated over frequency space to calculate the detectability index for the stent object.

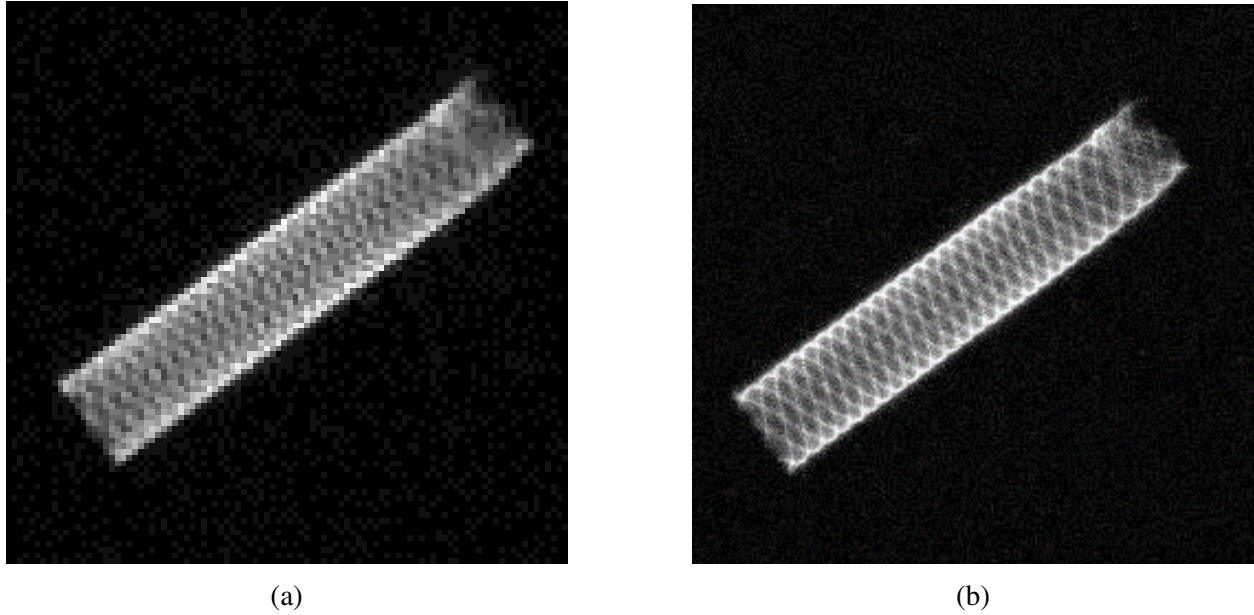


Figure 2.20: Inverted stent images acquired using (a) the FPD zoom mode and (b) the Hi-Def zoom mode.

Table 2.2 displays the GM-ROD values of the Hi-Def zoom mode relative to the FPD zoom mode as reported on previously.³⁹ The GM-ROD results show the improved performance across several magnification factors for varying integration bounds, with the Hi-Def producing a minimum of 1.90 times the detectability index for stent images relative to the FPD's performance and nearly 10 times the detectability index of the FPD zoom mode for image detail (integration bounds of $1.5 \frac{lp}{mm}$ to the Nyquist).

		GM-ROD of Stent Images (Hi-Def/FPD Zoom Modes)			
		Integration Bounds (cycles/mm)			
		0 to Nyquist	0.5 to Nyquist	1.0 to Nyquist	1.5 to Nyquist
Magnification	1.10 x	2.52	6.44	7.90	9.66
	1.16 x	2.22	5.66	6.93	8.42
	1.22 x	2.41	5.70	6.78	7.93
	1.28 x	2.16	4.98	6.02	7.09
	1.34 x	1.90	4.16	5.13	6.13

Table 2.2: GM-ROD values for different magnifications and spatial frequency integration bounds.

2.4 Discussion

It is clear from the results presented in this chapter that the Hi-Def zoom mode has improved performance over the FPD zoom mode under nearly all circumstances. The much smaller pixel size of the Hi-Def zoom mode enables the imaging of higher spatial frequencies (up to $6.6 \frac{lp}{mm}$) that are inaccessible to the FPD zoom mode. The low noise CMOS camera also gives relatively similar noise performance for exposure levels common to Digital Angiography (DA) sequences. These factors enable greater SNR performance for the Hi-Def mode across all but the lowest spatial frequencies (as quantified by the detector DQEs).

The improved SNR of the Hi-Def zoom mode enabled greater performance of the Hi-Def zoom mode relative to the FPD zoom mode across every task-based metric used to compare the two modes. This was most apparent when comparing changes to the integration bounds used to calculate the GM-ROD metric, allowing a more direct comparison of the detectors' respective abilities to image fine detail. This ability to detect device detail can have a great impact on the performance of neuro-interventional procedures.

The above studies were performed using raw image files acquired from the Canon imaging system. A CAN bus made by National Instruments⁴³ allowed for the raw image data to be read in real time to a separate computer terminal. A LabVIEW program called CAPIDS (Control Acquisition Processing and Image Display System)⁴⁴ was used to capture and save the raw image data. The use of the raw image data allowed a direct comparison of detector performance without the effect of image processing.

One concern that may arise from the use of the Hi-Def zoom mode is greater quantum noise due to the smaller pixel size. As has been shown in this chapter the Hi-Def zoom mode has a higher NNPS value, and therefore more noise, than the FPD mode under equivalent exposure conditions, though the difference is reduced as exposure increases. However, the nature of the Hi-Def zoom mode limits the FOV of the detector. This smaller FOV in turn reduces the scatter to the detector, which could enable the removal of the anti-scatter grid during use of the Hi-Def zoom mode.

The impact of the anti-scatter grid on image quality and exposure will be further examined in the following chapter.

2.5 Conclusion

The ROD family of metrics has previously been useful for the quantification of detectors' relative performance in imaging objects. This family of metrics has been used here to quantitatively demonstrate the improved performance of the Hi-Def zoom mode relative to the FPD mode in detecting an array of objects. The ROD demonstrates the maximum theoretical potential of the Hi-Def to outperform the FPD, especially for very small features. The G-ROD metrics demonstrate a more realistic measure of the expected performance of the Hi-Def relative to the FPD under more clinically relevant conditions incorporating scatter and other factors contributing to object blur. Finally, the GM-ROD is the most clinically relevant as it emphasizes the improved performance of the Hi-Def in imaging real objects relative to the FPD, and especially demonstrates the ability of the Hi-Def zoom mode to resolve fine detail that is critical to successful treatment during neuro-interventional procedures.

Chapter 3

Effect of Anti-Scatter Grid on Performance of Hi-Def Mode

3.1 Introduction

Scatter has long been known to degrade image quality by reducing image contrast in screen-film radiography, and as a source of noise in digital radiography degrading the SNR.⁴⁵ The deleterious effects of scattered radiation eventually led to the development of grid systems^{46,47} to reduce scatter to the detector. These grids typically consist of thin lead strips known as septa that can block scattered radiation, alternating with interspace materials (carbon fiber, aluminum, and other radio-luscent materials) that allow the primary radiation to pass through to the detector (see figure 3.1). These grids help to manage scattered radiation, but at the cost of higher exposures to the patient since the grid absorbs a significant portion of the primary radiation. The fraction of primary radiation transmitted through the grid is the primary transmission factor and is approximately 60%^{45,48} for most modern grids.

The Alphenix detector comes equipped with an anti-scatter grid to preserve image quality, and though use of a grid may be required under many circumstances there are additional methods that can be used to manage scatter. For example, the level of scattered radiation increases with field

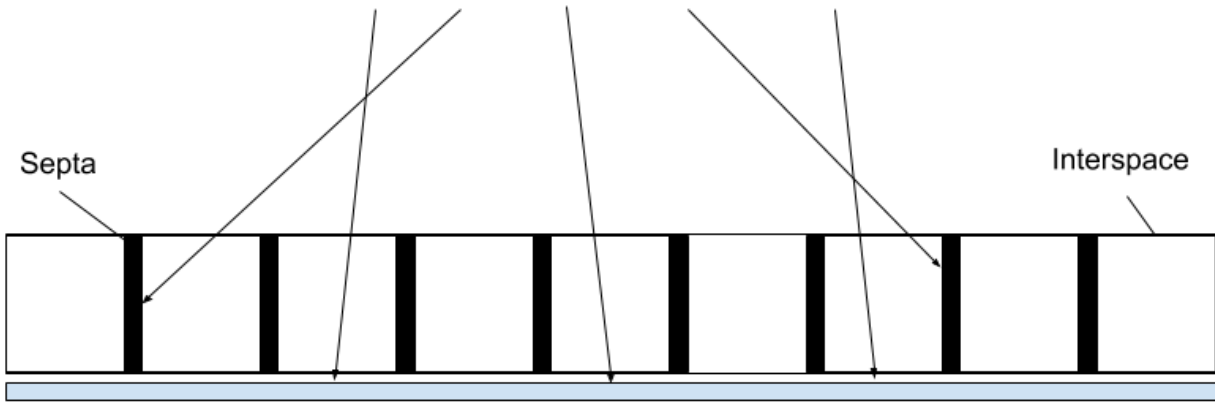


Figure 3.1: Diagram of an anti-scatter grid showing septa and interspace material. The septa are made of dense material, usually lead, to attenuate scattered radiation.

size and rises most sharply at the smallest field sizes before leveling off.⁴⁹ Therefore, scatter to the detector can be reduced through the use of smaller field sizes. Given that the Hi-Def mode makes use of smaller field sizes already, it may be possible to use the Hi-Def mode without the need for an anti-scatter grid.

To test the Hi-Def mode's performance without an anti-scatter grid in place the same metrics introduced in chapter 2 were used to measure detector performance for 3 of the standard field sizes of the Hi-Def zoom mode. These metrics were then compared against the metrics for the Hi-Def mode with the anti-scatter grid in place for identical technique parameters. For a task-based comparison the G-ROD was also acquired for the Hi-Def zoom mode with and without the grid in place.

3.2 Materials and Methods

3.2.1 Details of the Anti-Scatter Grid

Figure 3.2 shows a picture taken of the Alphenix anti-scatter grid. According to the label the grid has a ratio of 15:1 with 80 lines per cm. The primary transmission factor of the grid was measured with an ion chamber at the listed focal distance of 100 cm and was found to be 58% for an RQA5

spectrum.



Figure 3.2: Picture of the grid equipped to the Alphenix detector.

After measuring the primary transmission factor, the next step was to measure the scatter factors for the different Hi-Def zoom mode field sizes. To simulate patient scatter the ANSI head phantom⁵⁰ was used. The ANSI head phantom consists of (starting from the bottom) 2.5 cm of clear acrylic, followed by 2 mm of aluminum (type 1100 alloy), followed by another 10 cm of clear acrylic, a 1 mm aluminum sheet (type 1100 alloy), and a final 2.5 cm of clear acrylic each layer

measuring 30.5 cm by 30.5 cm. The ANSI phantom was placed on a patient table with the top surface of the phantom positioned 10 cm from the detector surface. With the phantom in place the scatter + primary exposure to the detector surface was measured with an ion chamber positioned in the center of the field of view for the four pre-programmed Hi-Def zoom mode field sizes (3 in, 2.3 in, 1.5 in). To measure exposure to the detector surface due to primary radiation the table was lowered to introduce a large air-gap, the ANSI head phantom was placed directly on top of the x-ray tube housing, and the beam was collimated to just the ion chamber. The scatter fraction can then be calculated in equation 3.1:

$$F = \frac{(P + S) - P}{P + S} = \frac{S}{P + S} \quad (3.1)$$

where P is the primary ionization exposure and $(P + S)$ is the scatter + primary ionization exposure.

3.2.2 Metrics Used for Comparison

To quantify the effect of scatter on the detectors spatial response, the G-MTF was then measured along both axes of the Hi-Def detector using the slanted edge method.²⁴ The ANSI head phantom was again positioned on the patient table 10 cm from the detector surface and the edge was placed against the outer housing of the detector to measure the MTF with scatter effects (see diagram in figure 3.3). Edge images were acquired with and without the grid in place for varying fields of view. For the acquired edge images the machine edge was placed against the detector housing along both axes of the detector array. Technique parameters were set to 70 kVp, 100 mA, and 10 ms with the small focal spot. 150 images were acquired using CAPIDS⁴⁴ and were dark-field and flat-field corrected. The acquired edge images were then averaged together before measuring the ESF. The G-MTF was then calculated using equation 2.1.

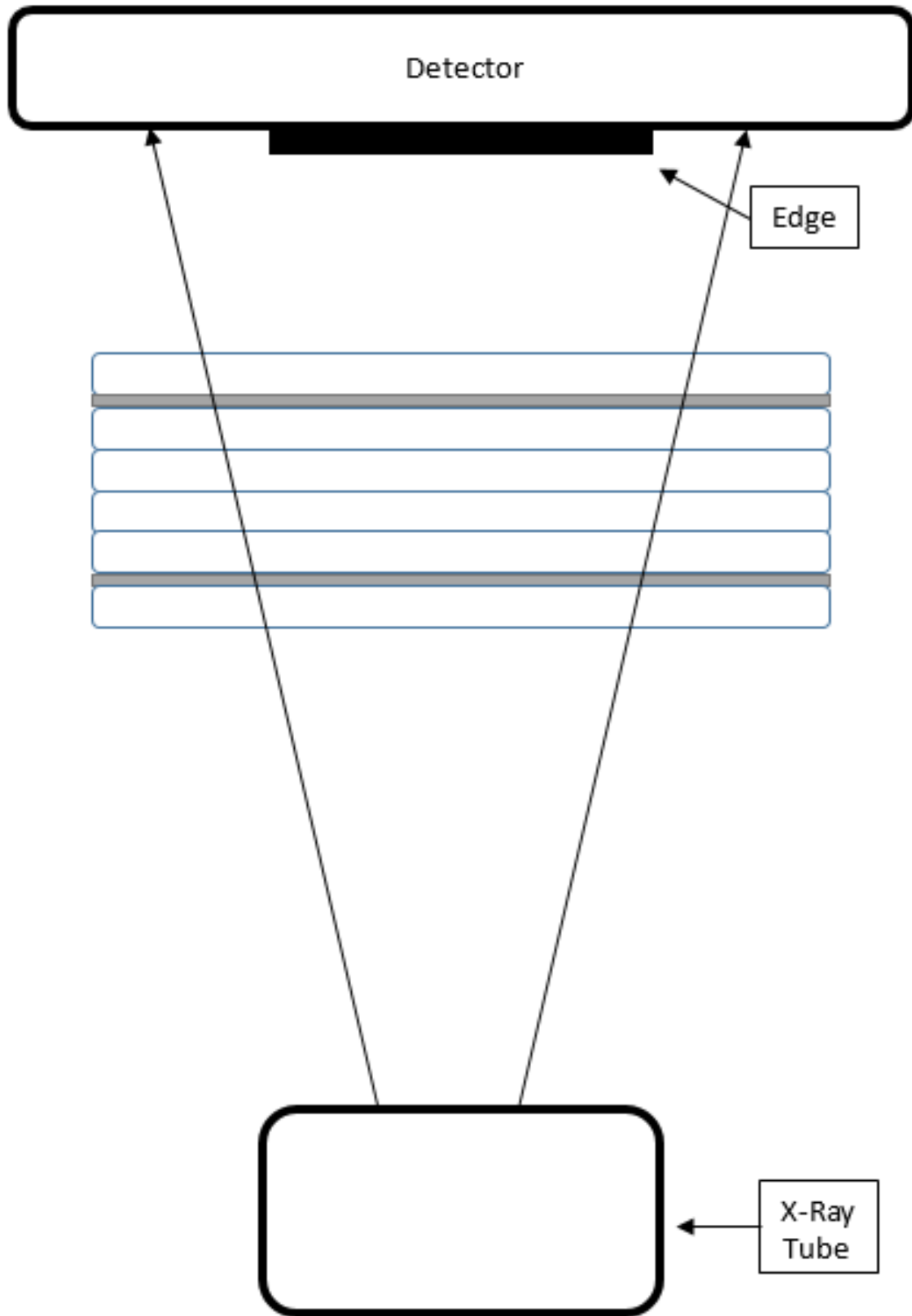


Figure 3.3: Diagram demonstrating how the G-MTF was measured for the Hi-Def zoom mode with and without anti-scatter grid.

To quantify the detectors noise response, the NNPS was measured from acquired flat-field images. The flat field images were acquired at 70 kVp, 100 mA, and 10 ms for all three field sizes with and without the grid in place. Once more the detector was positioned 10 cm from the surface of the ANSI head phantom to simulate patient scatter. 150 images were acquired and the dark-field and flat-field corrected before measuring the detector NNPS according to equation 2.2.

To quantify the effect of scatter on the detector's SNR the GDQE was computed from the detector's G-MTF and NNPS for all three field sizes with and without the grid in place according to equation 2.7.

The task-based performance of the two detectors was performed using the G-ROD metric. The G-ROD metric was used to compare detector performance in imaging small spheres, discs and wires and relies on the use of the detector GDQE according to equation 2.12. A direct comparison was made between the Hi-Def zoom mode performance field sizes with and without the grid in place.

3.3 Results

3.3.1 Standard Metrics

The measured G-MTF for the different field sizes of the Hi-Def mode with and without the grid in place are shown in figures 3.4 and 3.5. The measured G-MTF is similar at the higher spatial frequencies which is where most image detail is located. For the lower spatial regions there is slightly poorer performance in the case with no anti-scatter grid, and this degradation in performance only increases as the FOV (and therefore scatter) increases. This drop in performance is due to scatter reducing contrast near edges.

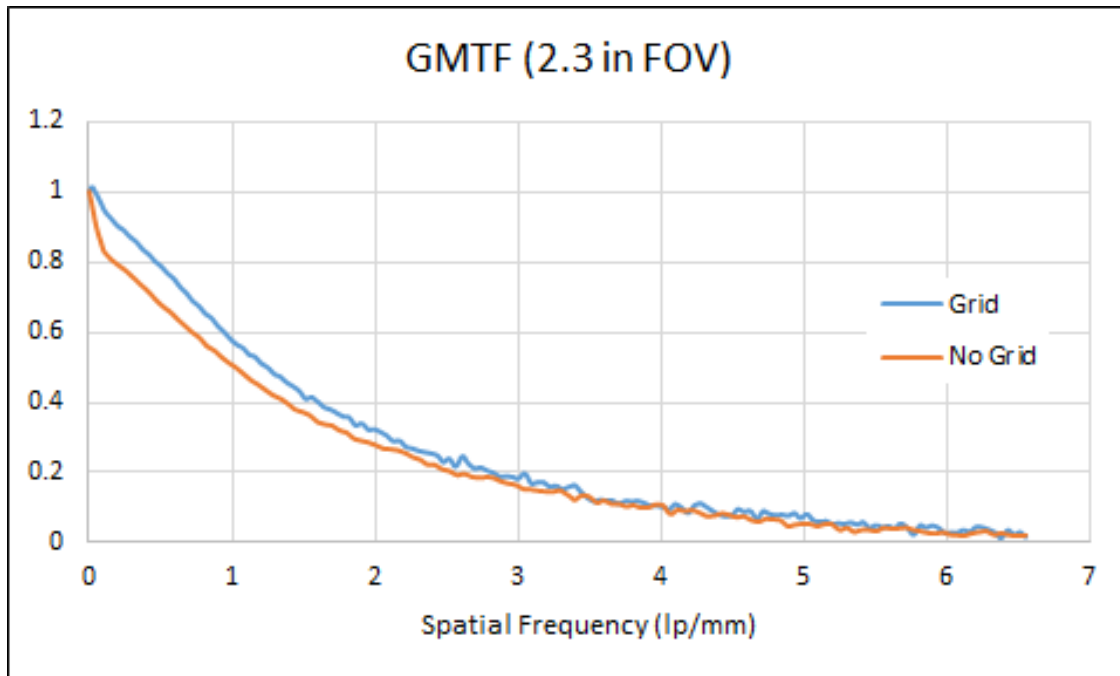


Figure 3.4: Detector G-MTF measured with and without the anti-scatter grid in place for the 2.3 inch FOV using the Hi-Def mode.

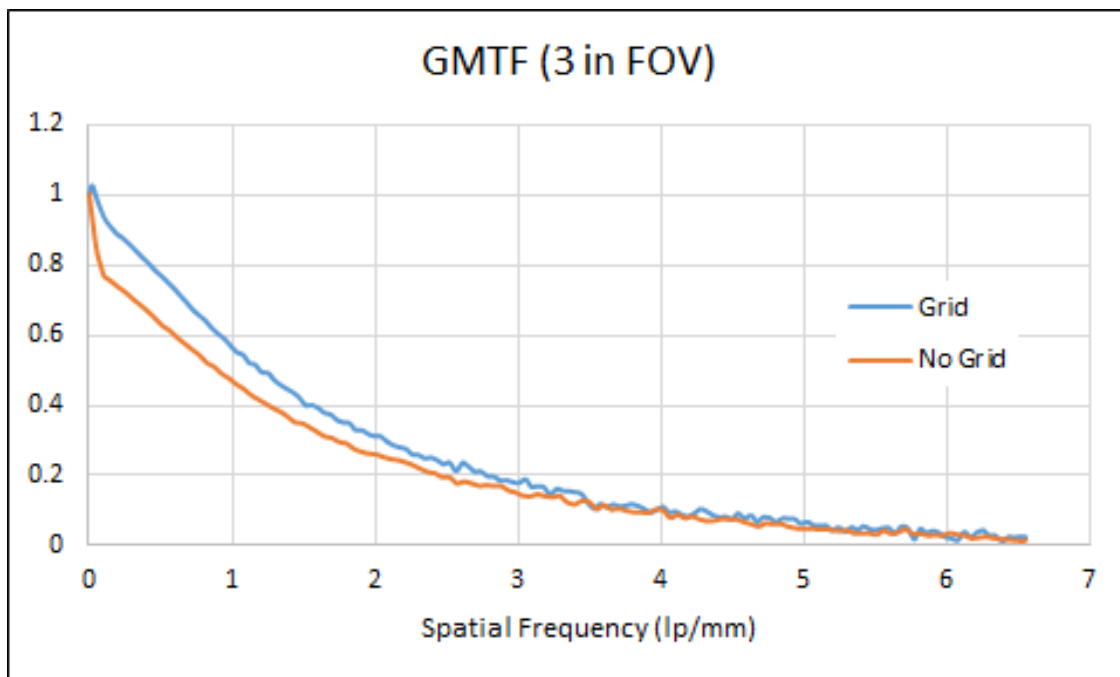


Figure 3.5: Detector G-MTF measured with and without the anti-scatter grid in place for the 3.0 inch FOV using the Hi-Def mode.

The measured NNPS for the different field sizes of the Hi-Def mode with and without the

grid in place are shown in figures 3.6 and 3.7. The NNPS for the Hi-Def mode generally shows better noise performance without the grid in place than with the grid in place. This is due to the increased photon fluence at the detector surface due to the removal of the grid. However, as the field size decreases the noise appears to suffer at the lower spatial frequencies and that becomes most dramatic at the smallest field size without the grid.

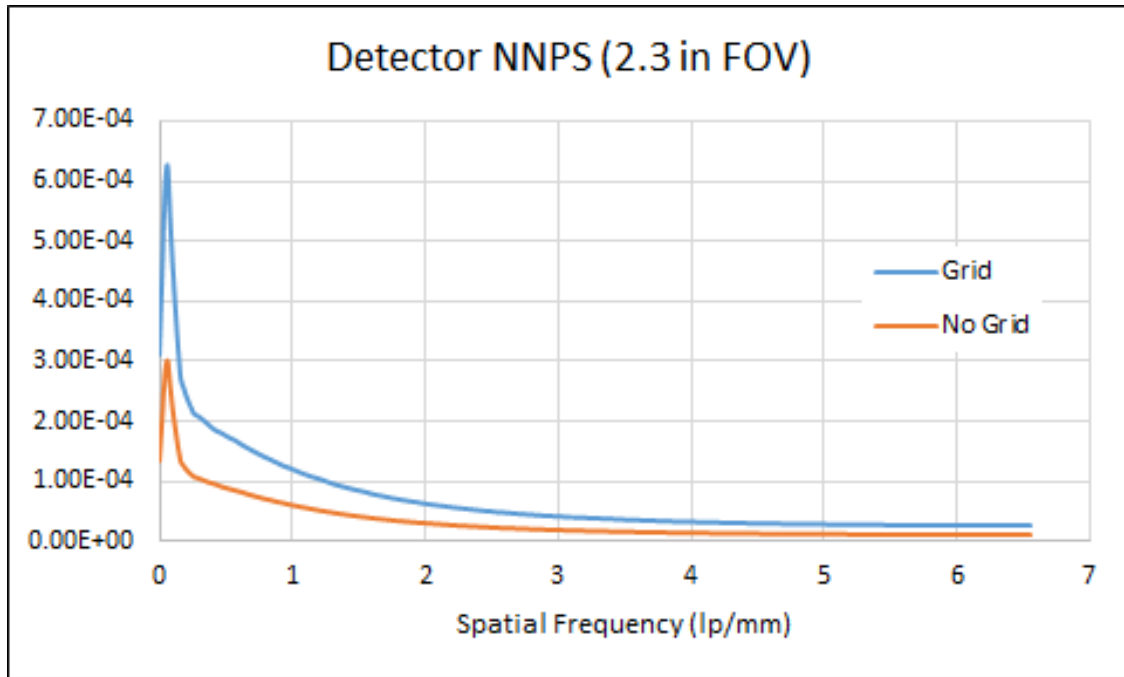


Figure 3.6: Detector NNPS measured with and without the anti-scatter grid in place for the 2.3 inch FOV using the Hi-Def mode. Exposure measured just prior to the grid was measured to be 324 nGy.

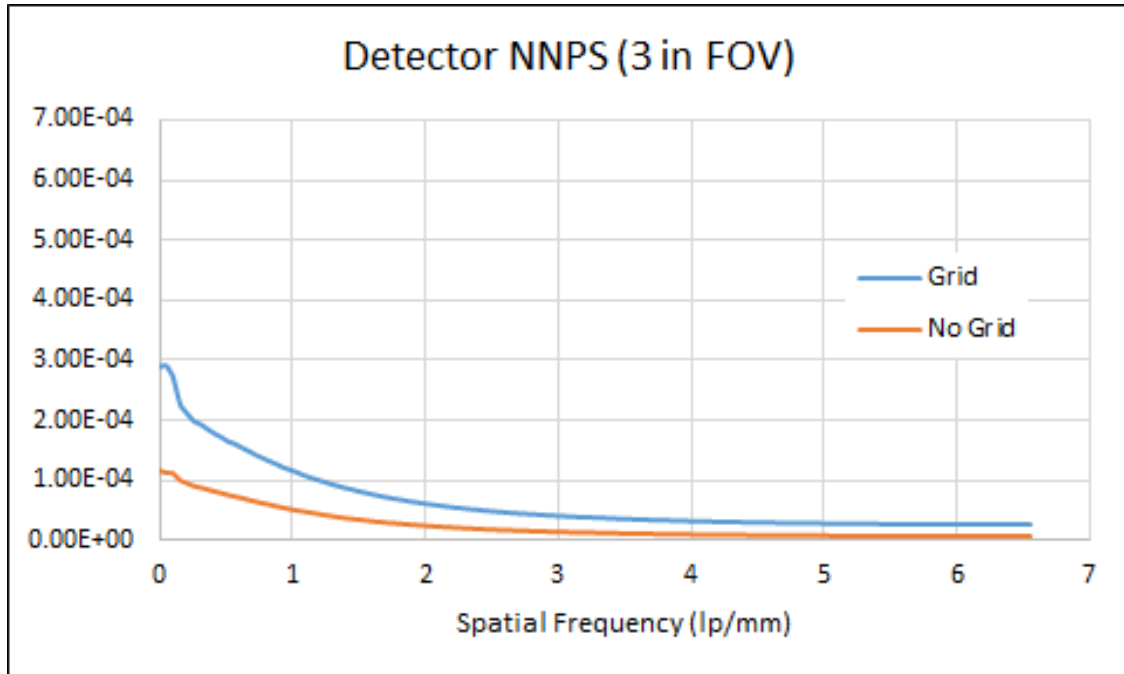


Figure 3.7: Detector NNPS measured with and without the anti-scatter grid in place for the 3.0 inch FOV using the Hi-Def mode. Exposure measured just prior to the grid was measured to be 324 nGy.

The measured GDQE for the different field sizes of the Hi-Def mode with and without the grid in place are shown in figures 3.8 and 3.9. The GDQE was measured according to equation 2.7 where the photon fluence ($\Phi(x)$) was measured based on the air kerma reaching the detector. If instead the air kerma that reaches the grid is used to calculate the GDQE, then the measured result becomes that shown in figures 3.10 and 3.11.

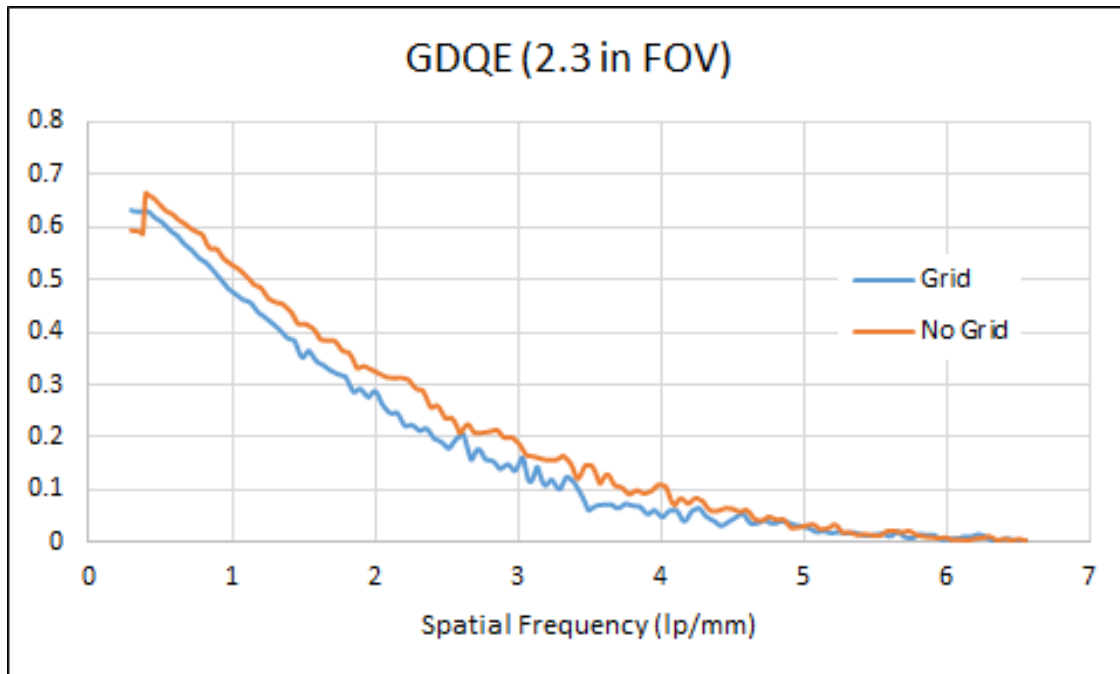


Figure 3.8: GDQE measured with and without the anti-scatter grid in place for the 2.3 inch FOV using the Hi-Def mode. Exposure measured at the detector surface was measured to be 188 nGy.

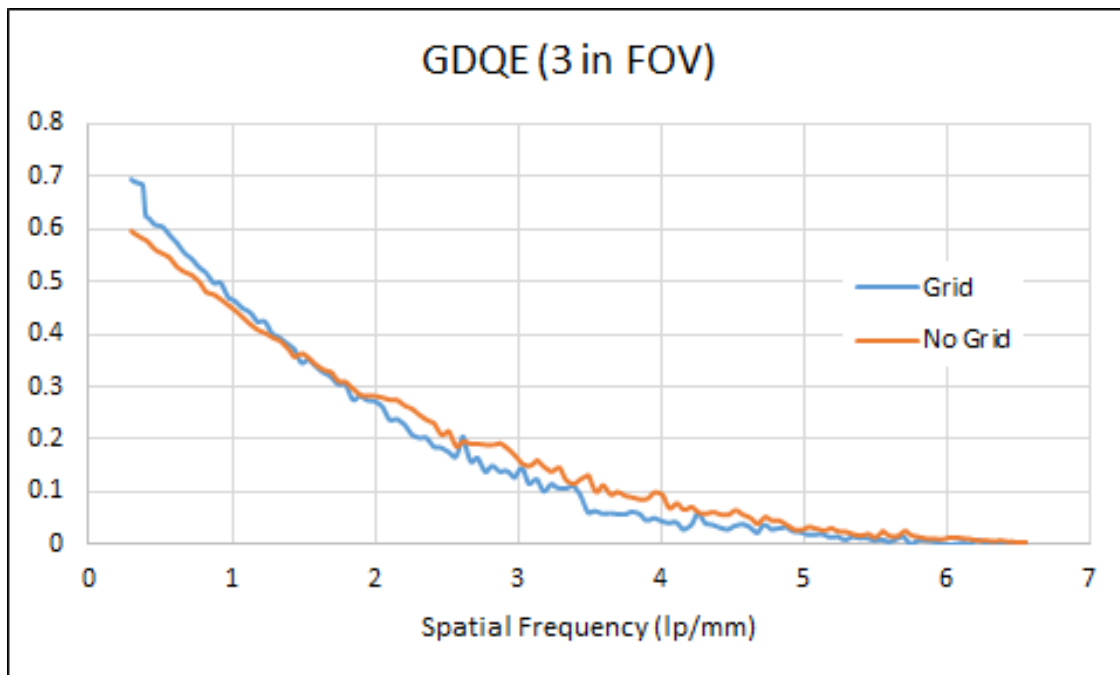


Figure 3.9: GDQE measured with and without the anti-scatter grid in place for the 3.0 inch FOV using the Hi-Def mode. Exposure measured at the detector surface was measured to be 188 nGy.

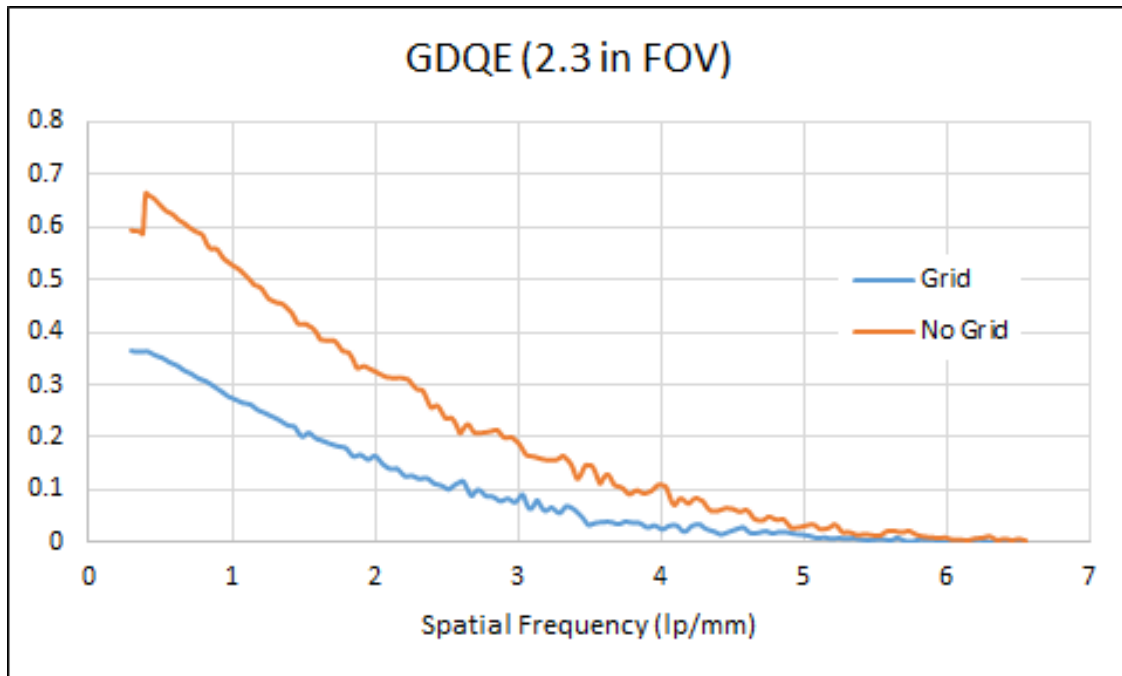


Figure 3.10: GDQE measured with and without the anti-scatter grid in place for the 2.3 inch FOV using the Hi-Def mode. The GDQE was calculated with the air kerma measured just prior to the grid (324 nGy).

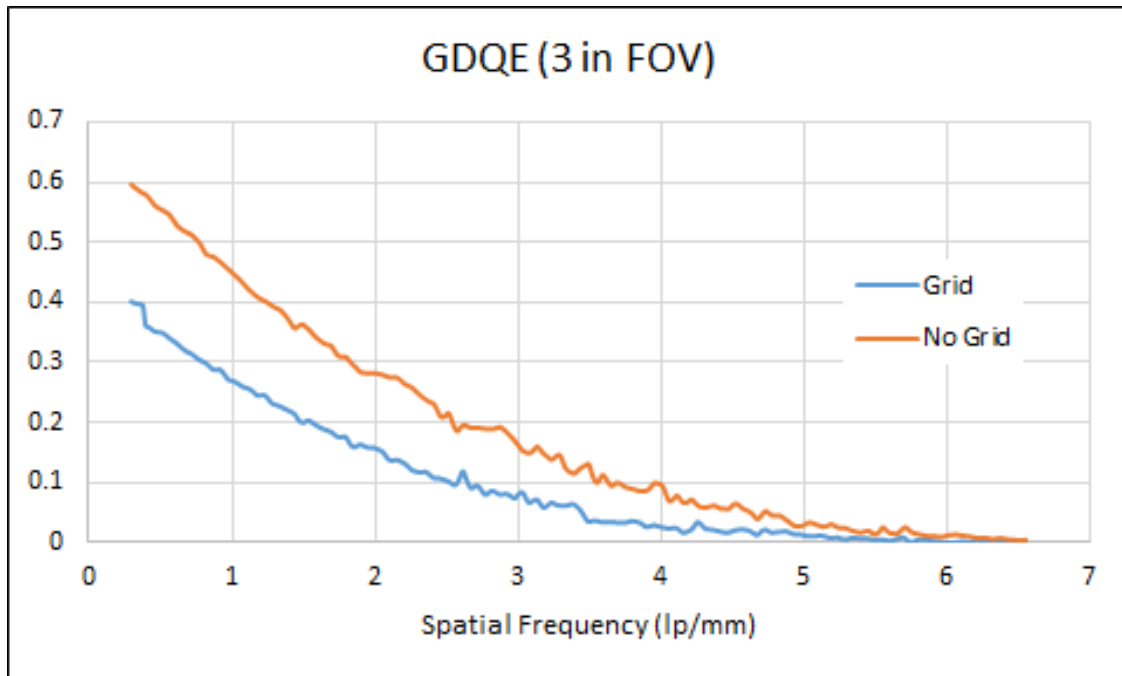


Figure 3.11: GDQE measured with and without the anti-scatter grid in place for the 3.0 inch FOV using the Hi-Def mode. The GDQE was calculated with the air kerma measured just prior to the grid (324 nGy).

3.3.2 G-ROD Metrics

The ROD family of metrics is a task-based comparison of detector modes, comparing their relative ability to image specific objects. The G-ROD comparison here was performed using discs, spheres, and wires as in chapter 2. These objects had simulated diameters ranging from 50 μm to 2 mm and were composed of aluminum. The results of the calculated G-ROD metrics calculated using GDQEs measured with fluence reaching the detector surface are shown in figures 3.12 and 3.13. The G-ROD metrics show that while performance varies slightly between detector FOVs, the relative imaging performance of the detector with and without the anti-scatter grid in place is near unity, though for very small objects the detector without the grid in place has slightly better performance.

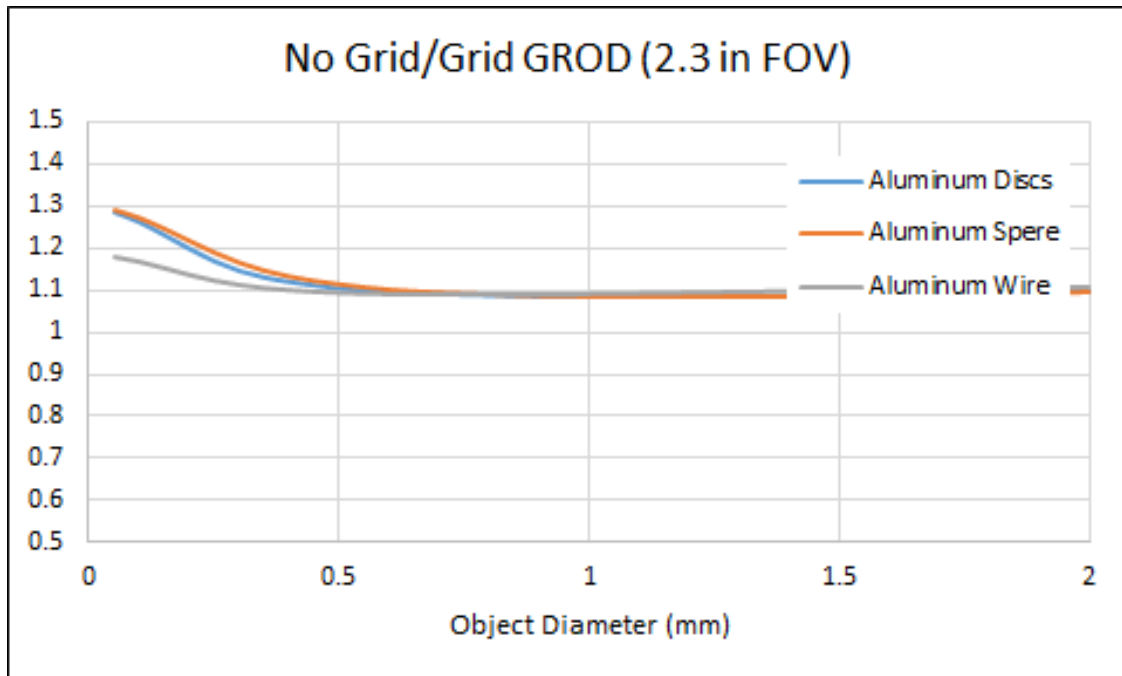


Figure 3.12: G-ROD measured with and without the anti-scatter grid in place for the 2.3 inch FOV using the Hi-Def mode.

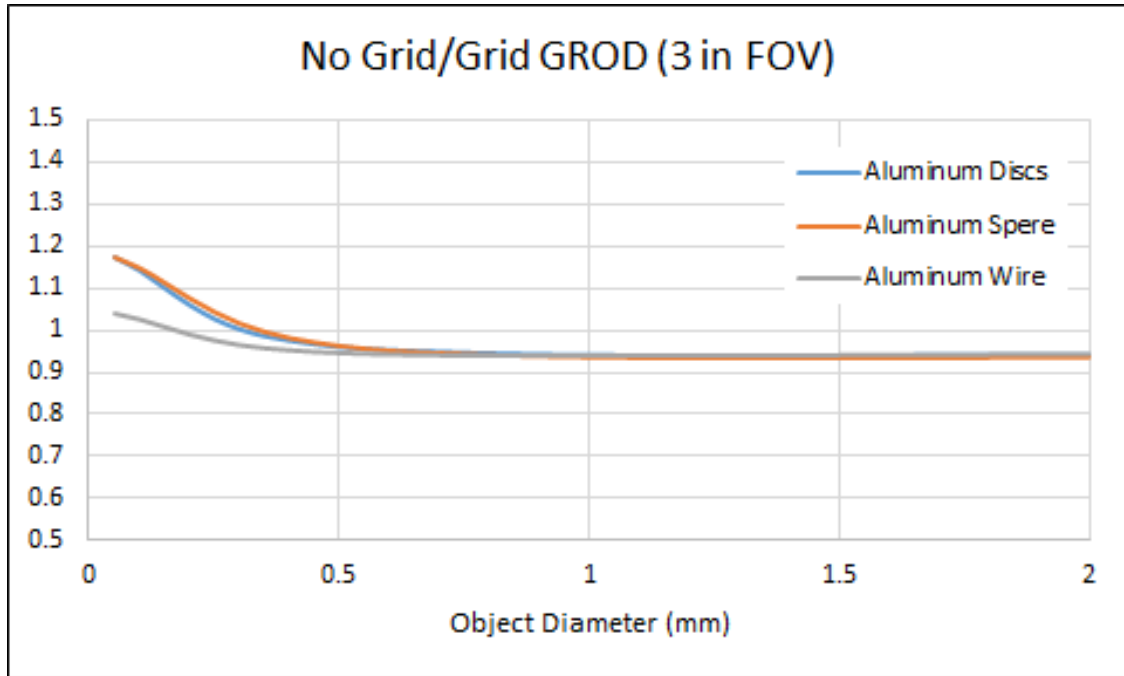


Figure 3.13: G-ROD measured with and without the anti-scatter grid in place for the 3.0 inch FOV using the Hi-Def mode.

If the G-ROD metric is calculated from the GDQE with air kerma measured just prior to the grid (a more fair comparison between the two imaging systems) then a comparison of the imaging systems can be made for the same dose to the patient. These G-ROD values are shown below in figures 3.14 and 3.15. Under these circumstances, the Hi-Def mode without the grid in place significantly outperforms the Hi-Def mode with the grid in place due to the increased photon fluence at the detector surface and its lower noise properties. The advantage is diminished slightly as object size increases, but that effect is minimal.

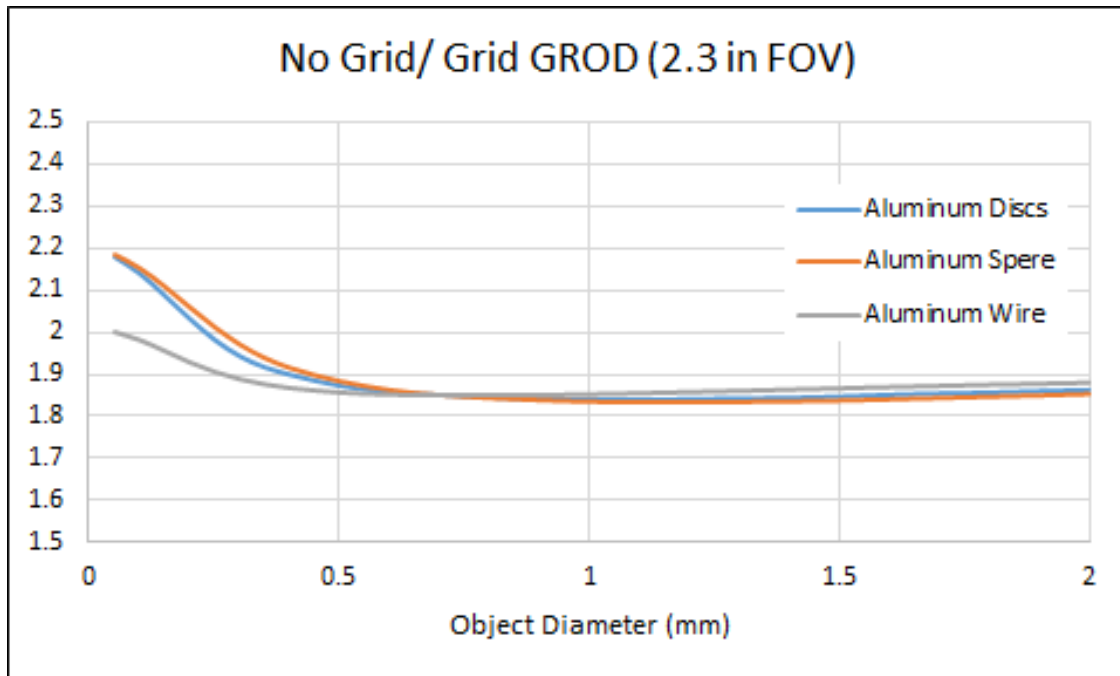


Figure 3.14: G-ROD measured with and without the anti-scatter grid in place for the 2.3 inch FOV using the Hi-Def mode. The GDQE was calculated with the air kerma measured just prior to the grid.

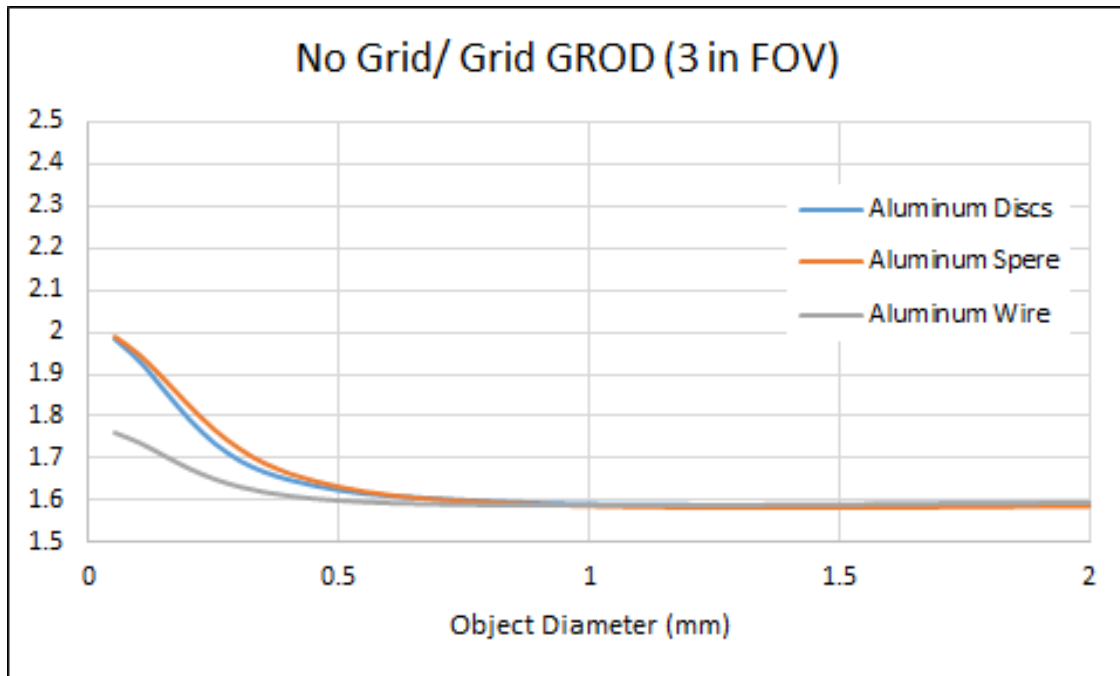


Figure 3.15: G-ROD measured with and without the anti-scatter grid in place for the 3.0 inch FOV using the Hi-Def mode. The GDQE was calculated with the air kerma measured just prior to the grid.

3.4 Discussion

The standard metrics demonstrate relatively similar spatial resolution performance across both detector set-ups. This was to be expected as the effect of scatter on image is a reduction in image contrast and for small fields of view scatter is greatly reduced. Most importantly, both systems maintain relatively similar abilities to image detail (denoted by the higher spatial frequencies of the GMTF) across all field sizes. And according to the GDQE, both systems have similar efficiency given the dose reaching the detector. Therefore quantitatively the two systems should provide similar performance allowing physicians to potentially reduce dose to the patient.

The G-ROD metric for the grid vs no grid Hi-Def detector mode clearly illustrates that the reduction in noise from the increased photon fluence benefits the detectors ability to image detailed objects. From the plots of the G-ROD metrics it was seen that for very small objects the no grid Hi-Def mode had better performance due to its reduced noise.

3.5 Conclusion

Anti-scatter grids have long been used in x-ray imaging applications, and their use has made them ubiquitous for nearly all modalities. However, in performing image guided interventional procedures, there are times when a smaller field of view is sufficient to image the ROI while sparing dose to the surrounding tissue. Given that scatter is a function of tissue volume, reducing the field of view in turn reduces scatter. With sufficiently low scatter the anti-scatter grid primarily serves to reduce the primary beam, but by removing the grid image quality can be improved for sufficiently small fields of view. Alternatively, removing the grid could also result in a reduction of dose to the patient while maintaining the same image quality if mAs is scaled appropriately.

Chapter 4

Assessment of Gantry-Motion Blur in Both Individual Projections and in Reconstructed Images for Cone Beam CT and Tomography

4.1 Introduction

Neuro-interventional procedures rely on optimal image quality to not only localize but also treat neurovascular pathologies. These detectors are susceptible to image blur due to motion, either patient movement or in the case of cone beam computed tomography (CBCT) the movement of the gantry rotation. For the purposes of this work the focus will be on gantry-motion induced blur. This research group has promoted the use of high resolution detectors that enable the visualization of fine features, however, excessive image blurring due to gantry motion could negate these gains.

To reduce patient motion blur during CBCT high gantry speeds are often used. However, gantry motion and a finite image capture time induce image blurring in CBCT projection views. For high resolution detectors, the image blur becomes more noticeable and reduces image resolution and contrast in the direction of gantry motion. To reduce gantry motion blur, effective exposure times or image capture times must be reduced by use of high frame rates and/or shorter x-ray pulses.

To demonstrate the effect of frame rates on gantry motion blur, a method of predicting gantry motion blur was investigated and experimentally verified. This method quantifies the amount of blur in individual projections based on geometry, gantry angular velocity and image capture time. The effects of frame rates are further explored with a simulated regular pattern phantom. Forward projections were acquired from the simulated phantom and the sinogram was blurred by averaging projections together. The simulated blurred projection frames were then reconstructed and compared to the original pattern phantom to make a qualitative and quantitative comparison of different frames rates.

4.2 Materials and Methods

4.2.1 Magnitude of Motion-Induced Blur Due to Gantry Rotation

Figure 4.1 shows a diagram of a point object rotating about the gantry isocenter at rotational speed ω . The diagram is in the rotational frame of reference to more clearly illustrate blurring effects and to simplify the derivation of gantry-motion blur. The figure illustrates how the movement of the point object during a single frame exposure moves the resultant projection across the detector and blurring the object.

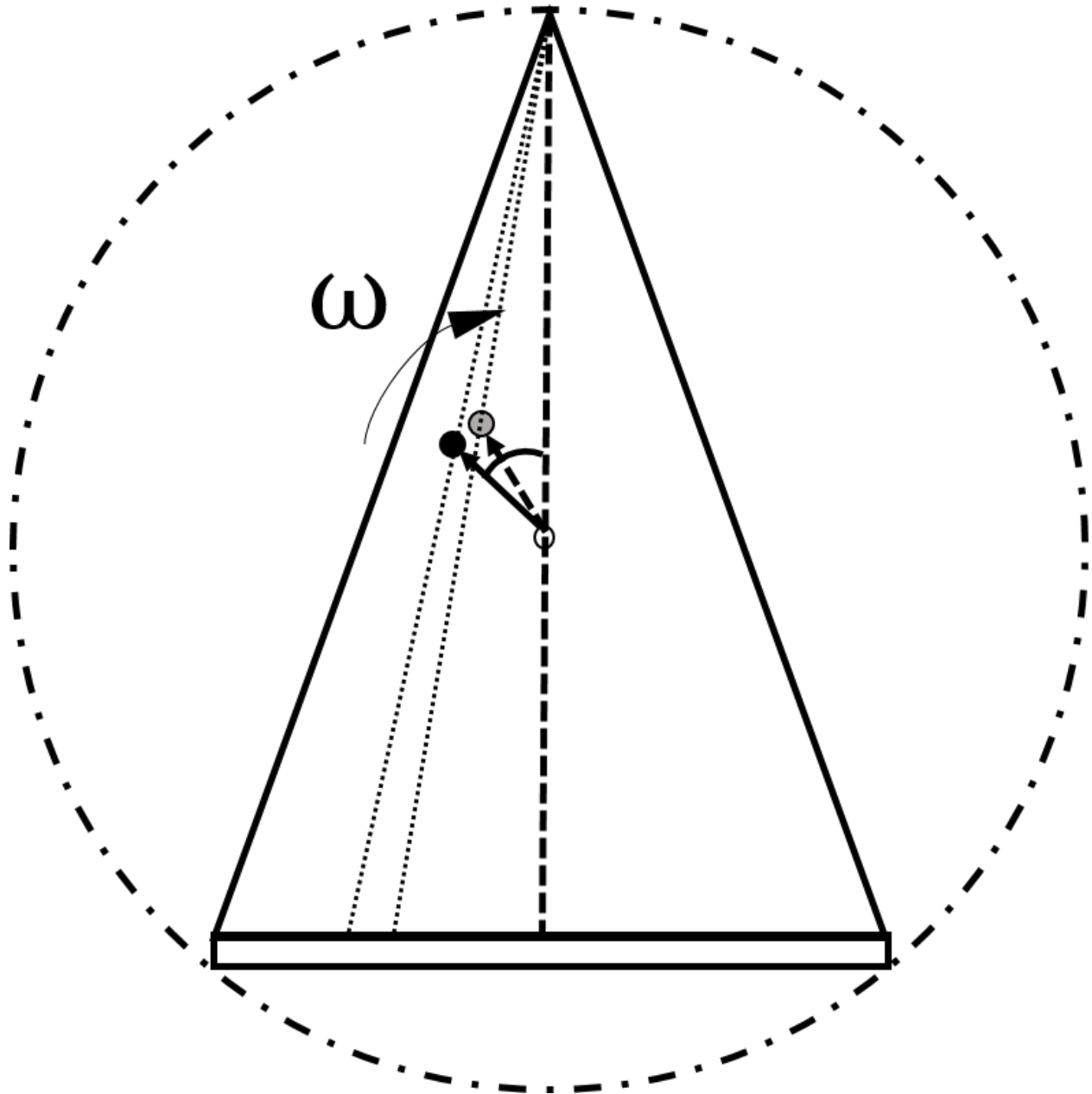


Figure 4.1: Diagram of a point object rotating about the gantry isocenter to illustrate gantry motion-induced blur in projection images.

The movement of an object's projection across the detector during image acquisition is directly responsible for the spatial blurring of that object's projection. The lateral distance of an object's projection can be calculated from the gantry geometry shown in figure 4.2.

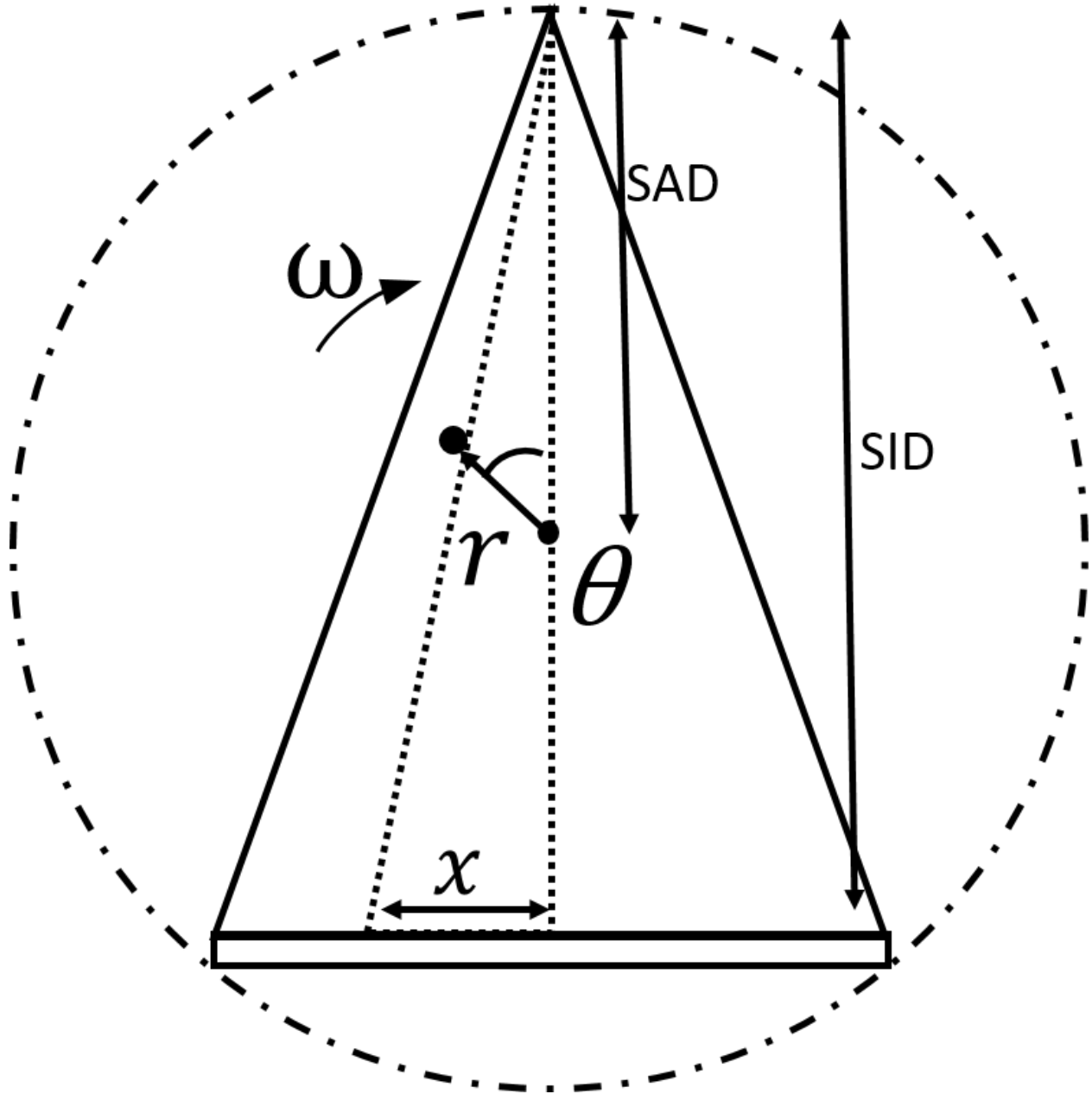


Figure 4.2: Diagram of a point object rotating about the gantry isocenter with the geometry labeled to facilitate calculating image projection blur.

In the above figure, ω is the gantry rotational velocity, r is the object's distance from the gantry's isocenter, θ is the angle between the position vector and the central axis, SAD is the source to rotational axis or isocenter distance, SID is the source to image distance, and x is the lateral distance of the object's projection from the detector center. x can be calculated using equation 4.1.

$$x = \frac{SID \cdot r \cdot \sin(\theta)}{SAD - r \cdot \cos(\theta)} \quad (4.1)$$

If the gantry rotates about the isocenter, then the object's position changes from θ_i to θ_f . Since blur can be quantified as $x_f - x_i$, the lateral distance can be used to quantify image blur according to equation 4.2 where θ_f has been replaced with $\theta_i + \omega t$ since $\Delta\theta = \omega t$.

$$Blur = SID \cdot \left(\frac{r \cdot \sin(\theta_i + \omega t)}{SAD - r \cdot \cos(\theta_i + \omega t)} - \frac{r \cdot \sin(\theta_i)}{SAD - r \cdot \cos(\theta_i)} \right) \quad (4.2)$$

The above equation can be expanded using trigonometric identities to equation 4.3.

$$Blur = SID \cdot \left(\frac{r \cdot \sin(\theta_i) \cos(\omega t) + r \cdot \cos(\theta_i) \sin(\omega t)}{SAD - r \cdot \cos(\theta_i) \cos(\omega t) + r \cdot \sin(\theta_i) \sin(\omega t)} - \frac{r \cdot \sin(\theta_i)}{SAD - r \cdot \cos(\theta_i)} \right) \quad (4.3)$$

Since ωt is small the value of $\cos(\omega t)$ can be approximated as 1 and $\sin(\omega t)$ can be approximated to ωt . Applying these approximations to equation 4.3, we can further expand blur to equation 4.4.

$$Blur = SID \cdot \left(\frac{r \cdot \sin(\theta_i) \cdot 1 + r \cdot \cos(\theta_i) \cdot \omega t}{SAD - r \cdot \cos(\theta_i) \cdot 1 + r \cdot \sin(\theta_i) \cdot \omega t} - \frac{r \cdot \sin(\theta_i)}{SAD - r \cdot \cos(\theta_i)} \right) \quad (4.4)$$

Further, since $r \cdot \sin(\theta_i) \cdot \omega t$ is small compared to the other terms in the denominator, the blur equation can be further simplified to equation 4.5.

$$Blur = SID \cdot \left(\frac{r \cdot \sin(\theta_i) + r \cdot \cos(\theta_i) \cdot \omega t}{SAD - r \cdot \cos(\theta_i)} - \frac{r \cdot \sin(\theta_i)}{SAD - r \cdot \cos(\theta_i)} \right) \quad (4.5)$$

Finally, since $SAD - r \cdot \cos(\theta_i) = SOD$ and since $\frac{SID}{SOD} = m$ where m is magnification, blur can be reduced to equation 4.6.

$$Blur = m \cdot [r \cdot \sin(\theta_i) + r \cdot \cos(\theta_i) \cdot \omega t - r \cdot \sin(\omega t)] = m \cdot r \cdot \omega t \cdot \cos(\theta_i) \quad (4.6)$$

The above equation was then experimentally verified. Verification was performed using a Canon interventional C-arm equipped with a Dexela high resolution detector ($75 \mu\text{m}$ pixels) to quantify minute changes in an object's spatial projection. Two small lead BBs and a thin platinum wire were suspended along the central axis above the gantry isocenter. The table height was adjusted to move the objects from 5 to 25 cm from the isocenter in 4 cm intervals. The gantry was rotated at the only available rotational speed of 20°s^{-1} . Images were acquired using a 34.2 ms exposure time, a current of 10 mA, and 50 kVp to maximize the object's contrast.

The gantry motion produced a blurred projection of the BBs and wire. The software package ImageJ⁵¹ was used to acquire grayscale profiles across the BB's center. The projection image dimensions were corrected for magnification and a line was fitted to the BB edges. The fitted line was extrapolated to the background grayscale level to get the total width of the BB. A sample line profile is shown below in figure 4.3.

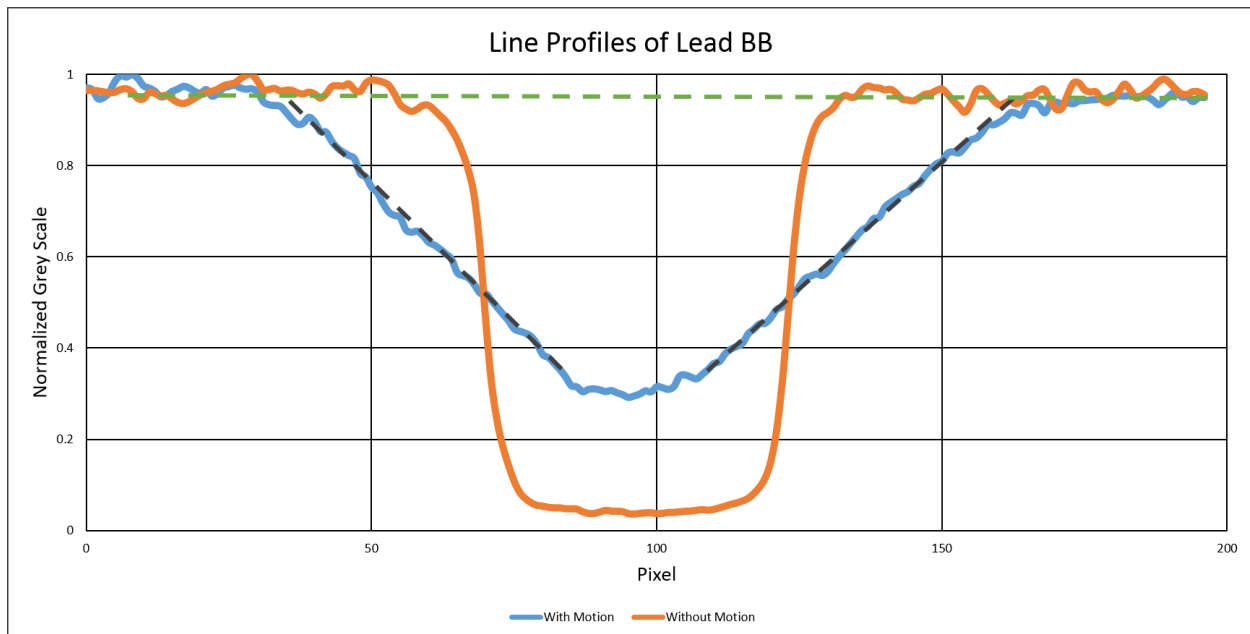


Figure 4.3: Sample line profiles acquired with and without gantry motion. The dashed green line shows the background grayscale level and the dashed gray lines approximate the lines fitted to the BB edges for measuring the blurred BB width.

The object width was measured for each blurred image and plotted against the BB's distance from isocenter and a line was fitted to the data using the linear regression method. Since the objects are imaged along the central ray, $\theta_i = 0$, and given that the blurred image dimensions have already been corrected for magnification, the blur equation becomes equivalent to equation 4.7.

$$Blur = r \cdot \omega t \quad (4.7)$$

The simplified linear equation can then be used to predict the slope of the fitted line in the experiment.

4.2.2 Gantry Rotational Motion-Induced Blur in Cone-Beam Computed Tomography

To measure the effect of projection blur on reconstructed images a 2-D phantom was simulated consisting of a pattern of squares, three pixels by three pixels, the centers of which were spaced 32 pixels apart in an image measuring 1024 by 1024 pixels. Simulated pixel size was set to 100 microns. The 9-pixel squares were assigned a value of one on a background assigned to a value of zero. The pattern was limited to a radius of 512 pixels to prevent artifacts in the reconstruction due to objects outside the field of view. The simulated pattern phantom is shown in figure 4.4.

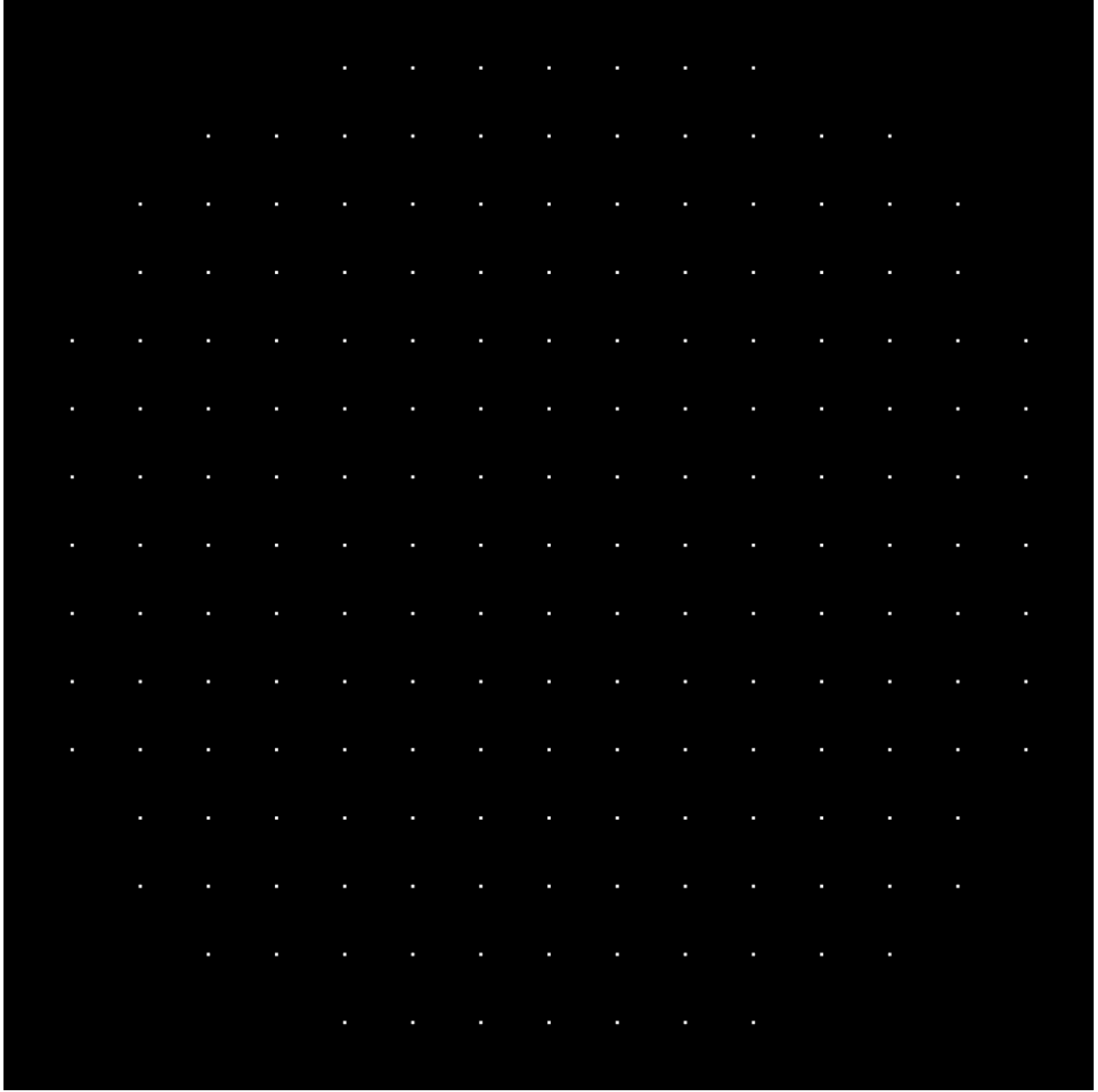


Figure 4.4: Simulated pattern phantom with fine features used to measure the effects of gantry motion blur on reconstructed images.

The phantom was rotated by tenths of a degree using a rotation matrix. Pixel values were assigned using the nearest neighbor method. Following the rotation, each column was summed to give a single detector element projection reading in the simulated detector using parallel beams for this demonstration. This process was repeated over a full 360-degree rotation to produce 3600 projection views. The resulting data was stored in a 1024 by 3600 sinogram shown in figure 4.5.

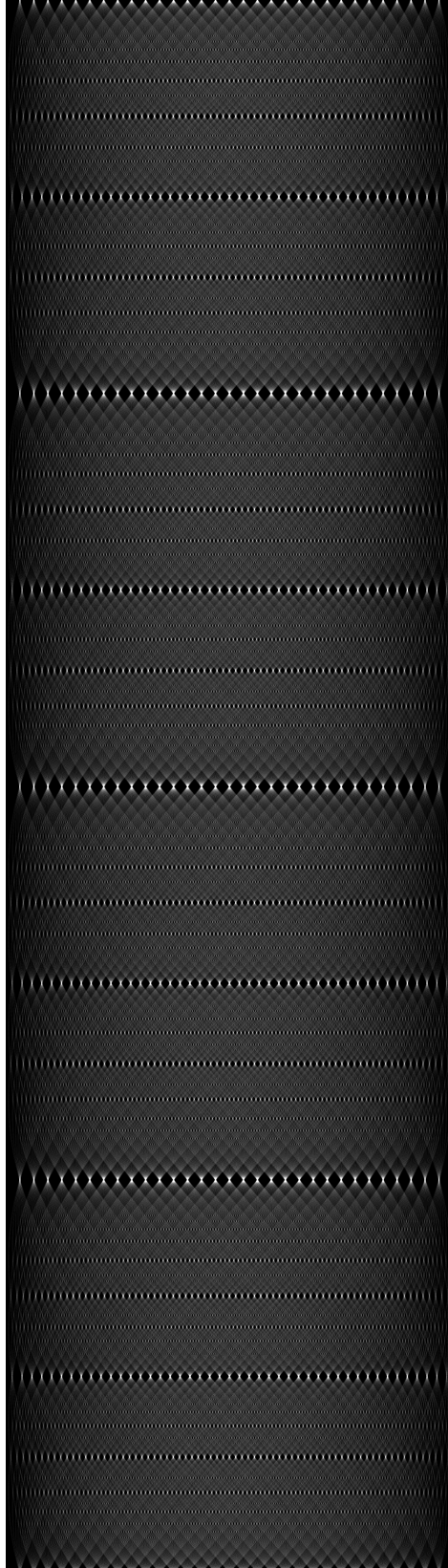


Figure 4.5: Sinogram of projections acquired every 0.1° from the simulated pattern phantom. Projection angles are along the vertical axis and detector values are along the horizontal axis.

To simulate blurring, N projections were averaged together simulating a continuous ‘on’ exposure with no dead time in the frame acquisition. N was determined from the simulated rotational speed of the gantry divided by the simulated frame rate and the angular step size (set at one tenth of a degree as stated above). The blurred projections were then stored in a separate sinogram whose dimensions were 1024 by $3600 / N$. Simulated gantry rotation speed was set to $60^\circ s^{-1}$ and three simulated frame rates were used: 30 fps, 60 fps, and 120 fps (with corresponding frame acquisition times of 33.3 ms, 16.7 ms, and 8.3 ms respectively).

For reconstruction, the projections were convolved with a Shepp-Logan filter before being backprojected. New angles corresponding to each blurred projection were calculated and the filtered backprojections were added to the reconstructed image using a linear interpolation, or nearest pixel, method.

Since the projections and reconstructions were made using a parallel beam geometry, for this demonstration the magnification is unity. Taking the derivative of equation 4.6 with respect to θ gives the maximum blur occurring at 0 and 180 degrees. Therefore the maximum predicted blur occurs when an object lies along the central axis. Simulated images were qualitatively compared for blur and the measured blur was compared to the maximum predicted blur of individual projections.

4.3 Results

4.3.1 Magnitude of Motion-Induced Blur Due to Gantry Rotation

Figure 4.6a is a sample image acquired during the validation experiment that demonstrates the magnitude of blur that can occur due to gantry motion, and how it might degrade image quality for high-resolution detectors. Compare the effects of image blurring to figure 4.6b in which no gantry motion enables the detector to capture very detailed images.

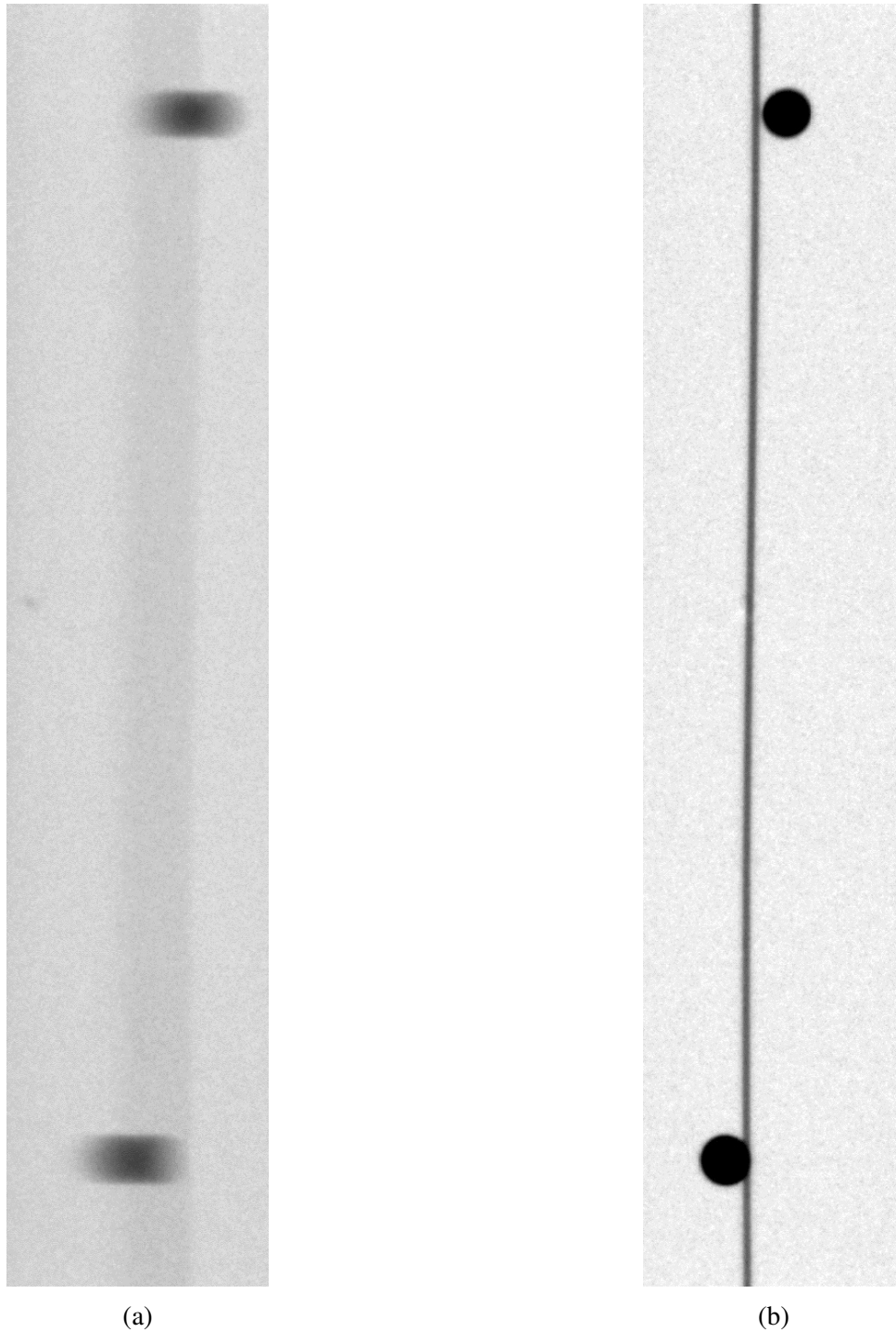


Figure 4.6: Images showing (a) the effect of motion blur along the direction of gantry rotational motion compared to (b) no gantry motion. Gantry rotational speed was fixed at $20^{\circ} s^{-1}$, with the object positioned 25 cm from isocenter with a frame length of 34.2 ms.

The magnitude of the blurred BB width is plotted as a function of the BB's distance from

isocenter in figure 4.7. A line was fitted to the data using the linear regression method. The equation for the fitted line is shown in the top left corner of the plot. The correlation coefficient confirms the linearity of the model. The predicted slope ωt was found to be within 4.2% of the experimentally obtained slope. The intercept of the plot is the theoretical unblurred diameter of the BB which was compared to the actual BB diameter as measured with calipers, the percent difference of these two measurements was found to be just 1.51%.⁵²

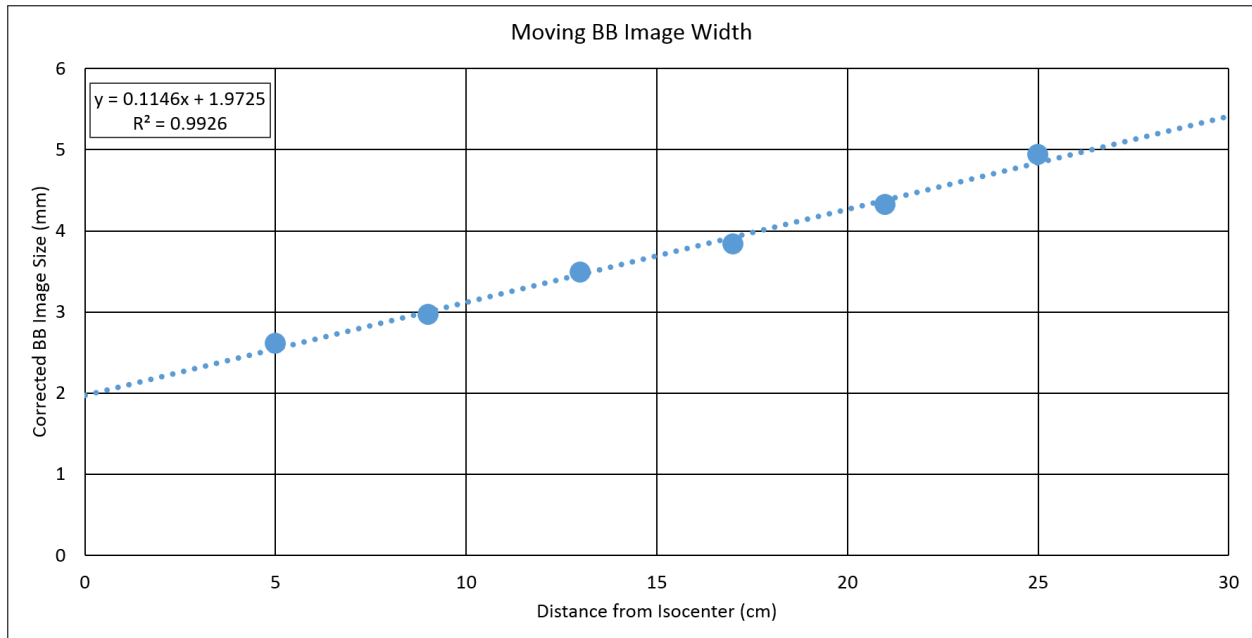


Figure 4.7: Magnitude of blurred BB width plotted as a function of distance from isocenter.

4.3.2 Gantry Rotational Motion-Induced Blur in Cone-Beam Computed Tomography

The number of projections averaged together was calculated according to equation 4.8 where N is number of projections to be averaged, ω is the gantry rotational speed, f_{ps} is the simulated frame rate, and $\Delta\theta$ is the is the 0.1° step used in the original simulated sinogram.

$$N = \frac{\omega}{f_{ps} \cdot \Delta\theta} \quad (4.8)$$

The simulated sinograms are shown in figures 4.8, 4.9, and 4.10 for simulated frames rates of

30, 60, and 120 fps respectively.

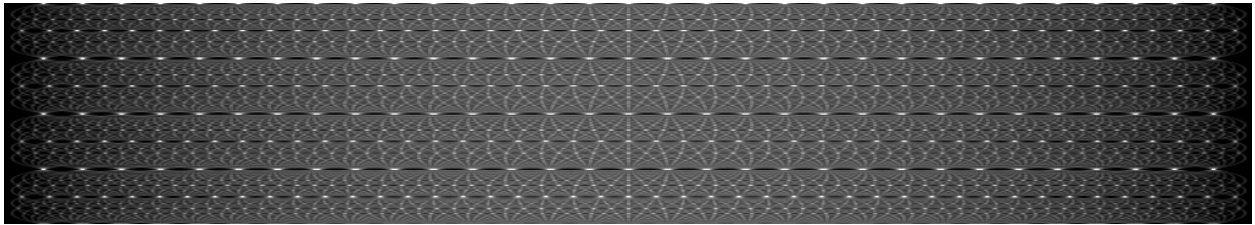


Figure 4.8: Simulated 30 fps (33.3 ms acquisition time) sinogram. Projection angles are along the vertical axis and detector values are along the horizontal axis.

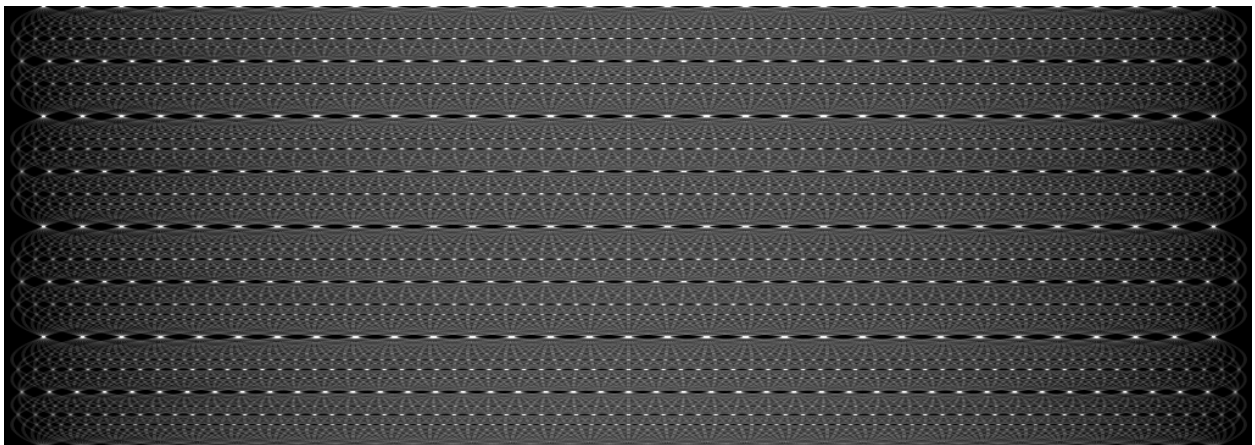


Figure 4.9: Simulated 60 fps (16.7 ms acquisition time) sinogram. Projection angles are along the vertical axis and detector values are along the horizontal axis.

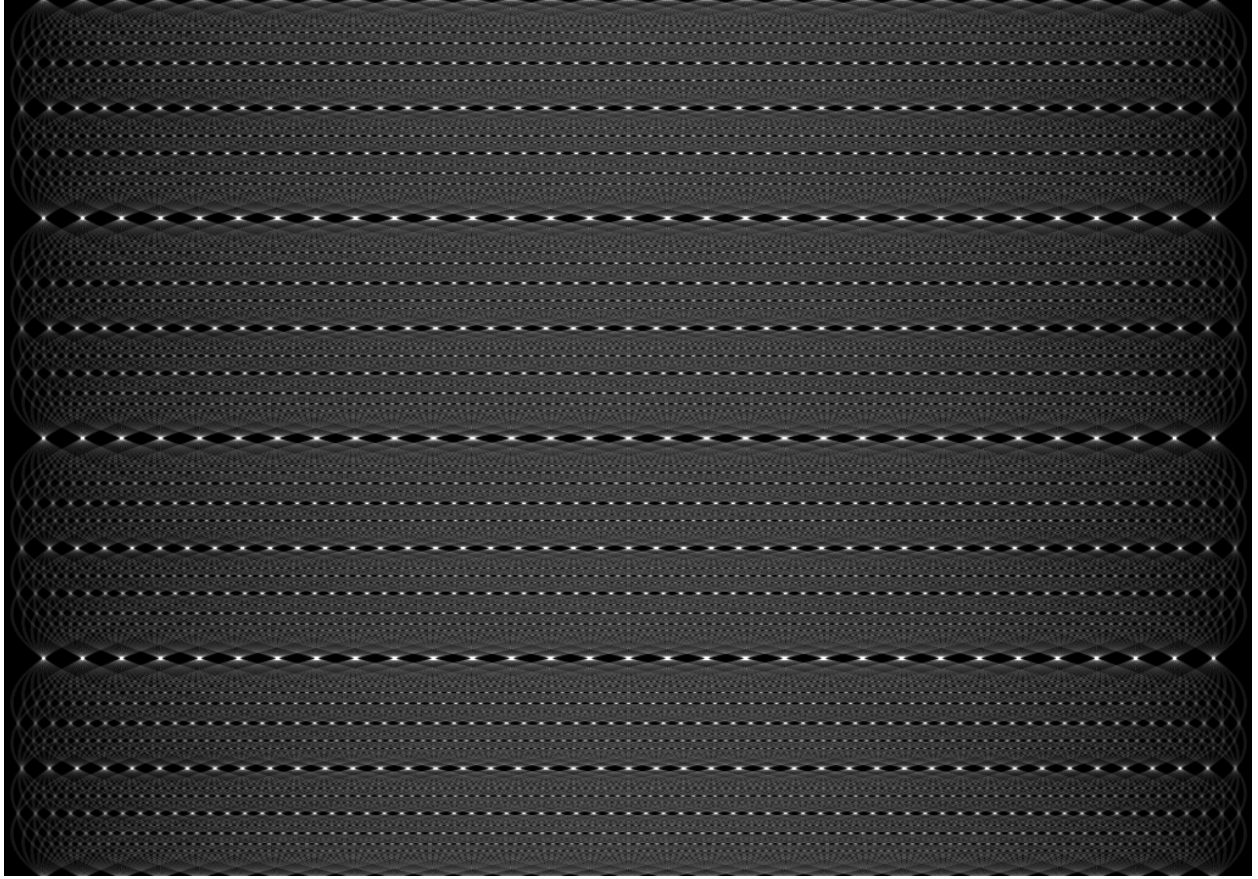


Figure 4.10: Simulated 120 fps (8.3 ms acquisition time) sinogram. Projection angles are along the vertical axis and detector values are along the horizontal axis.

Reconstructed images from the simulated blur sinograms are shown in figures 4.11, 4.12, and 4.13 for simulated frames rates of 30, 60, and 120 fps respectively.

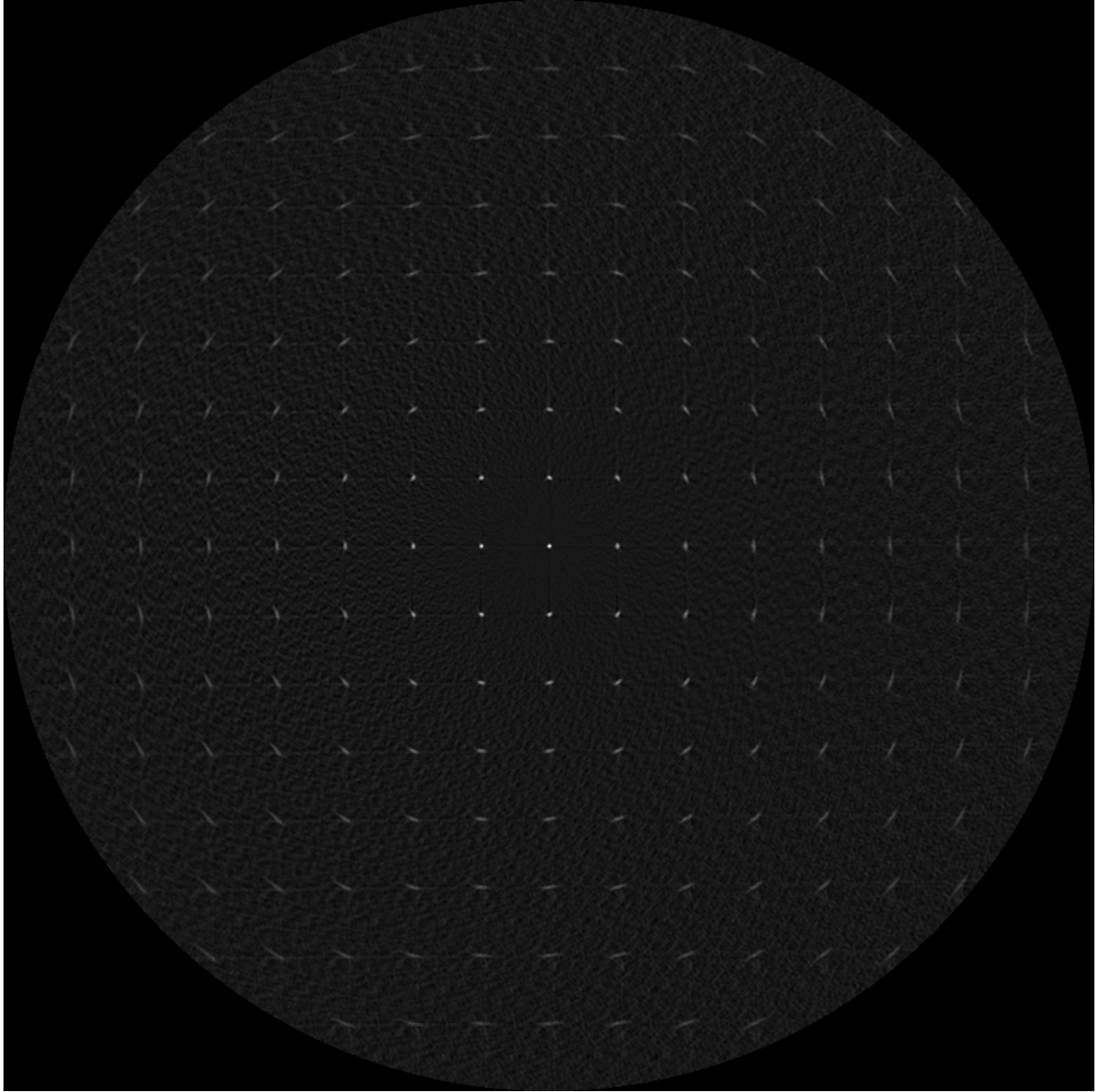


Figure 4.11: Reconstructed image using the simulated 30 fps (33.3 ms acquisition time) sinogram.

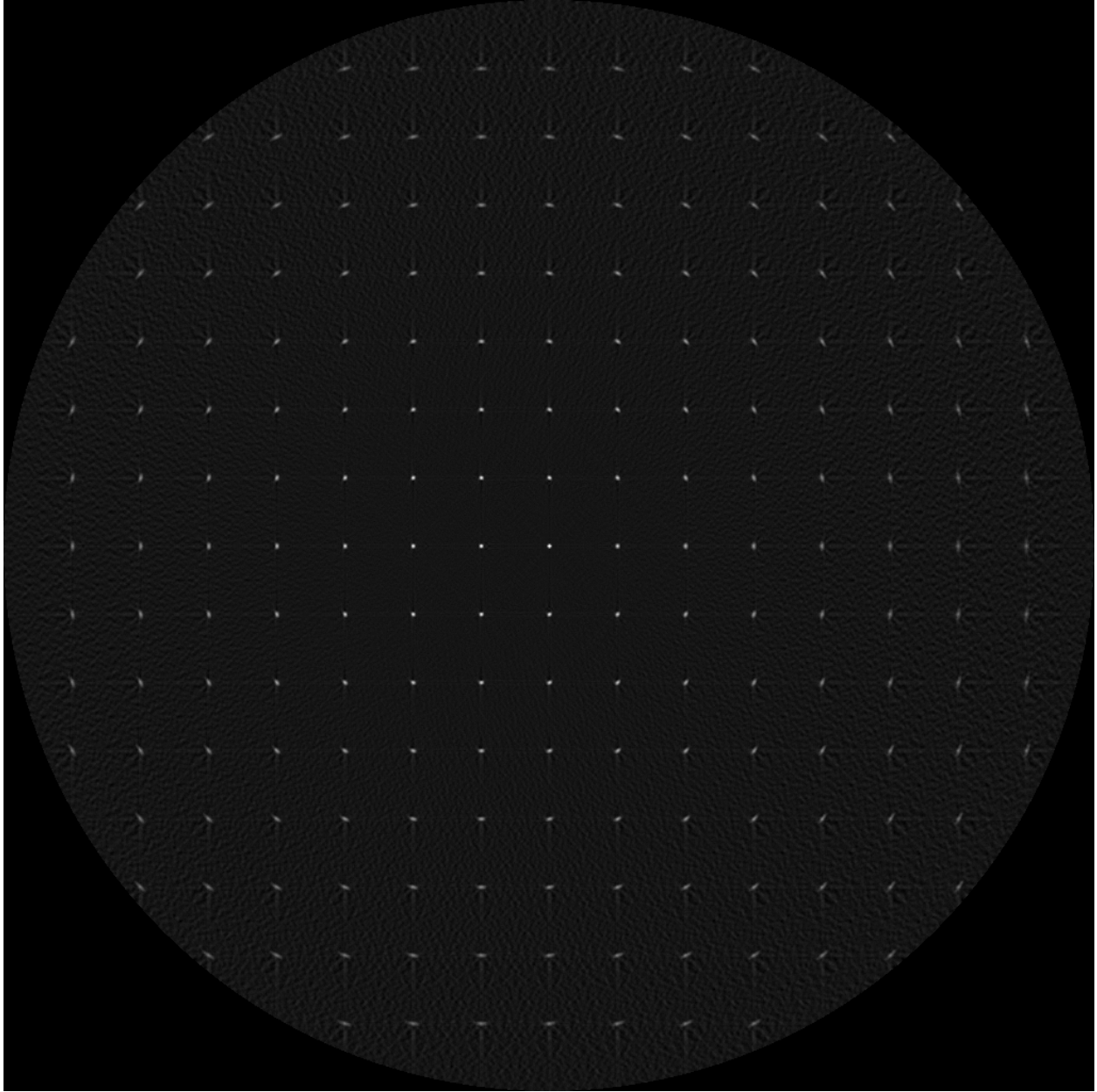


Figure 4.12: Reconstructed image using the simulated 60 fps (16.7 ms acquisition time) sinogram.

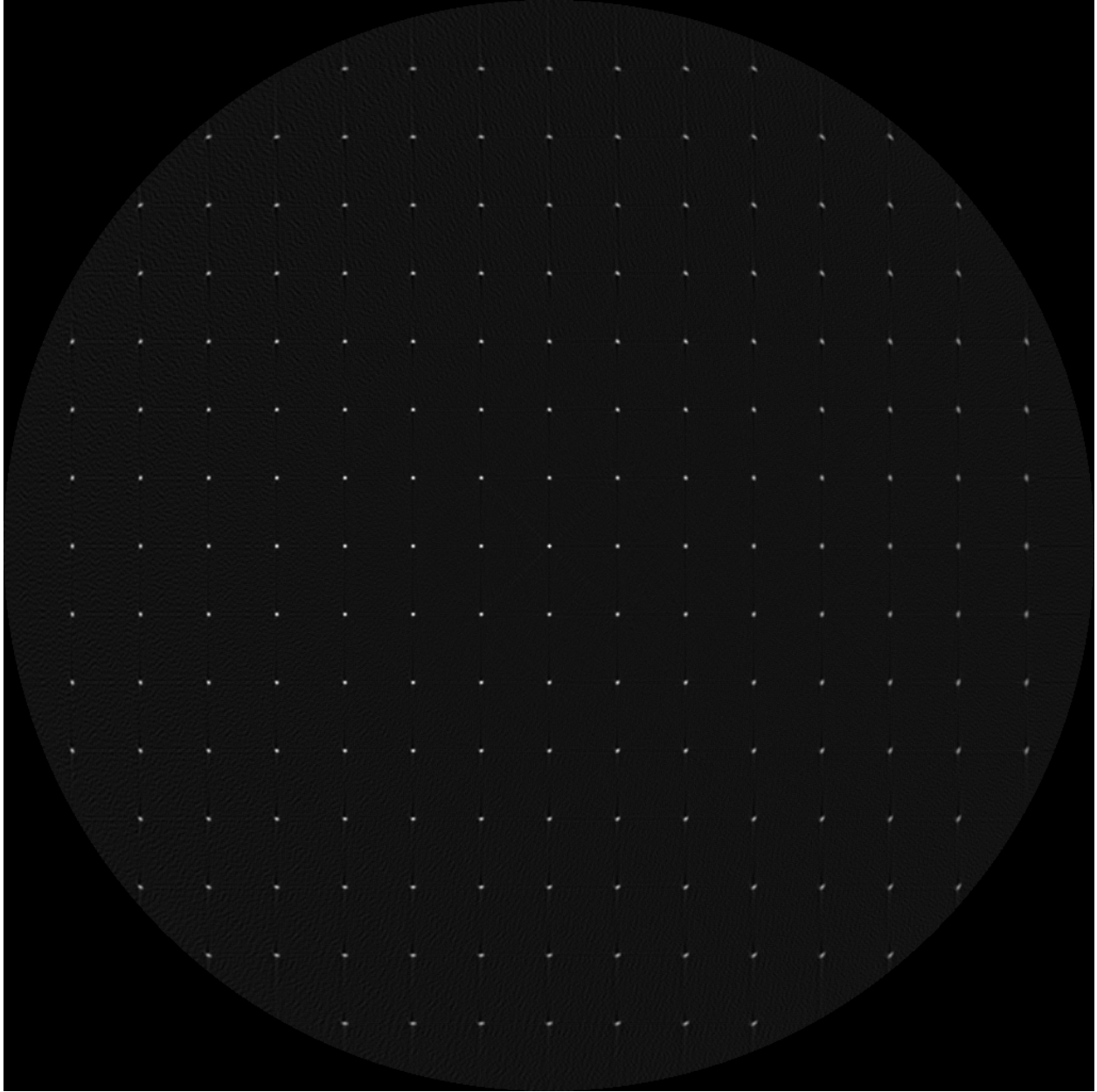


Figure 4.13: Reconstructed image using the simulated 120 fps (8.3 ms acquisition time) sinogram.

To further illustrate the gantry motion blur, upper left quadrants of the simulated phantom and the blurred reconstructions are shown in figure 4.14.

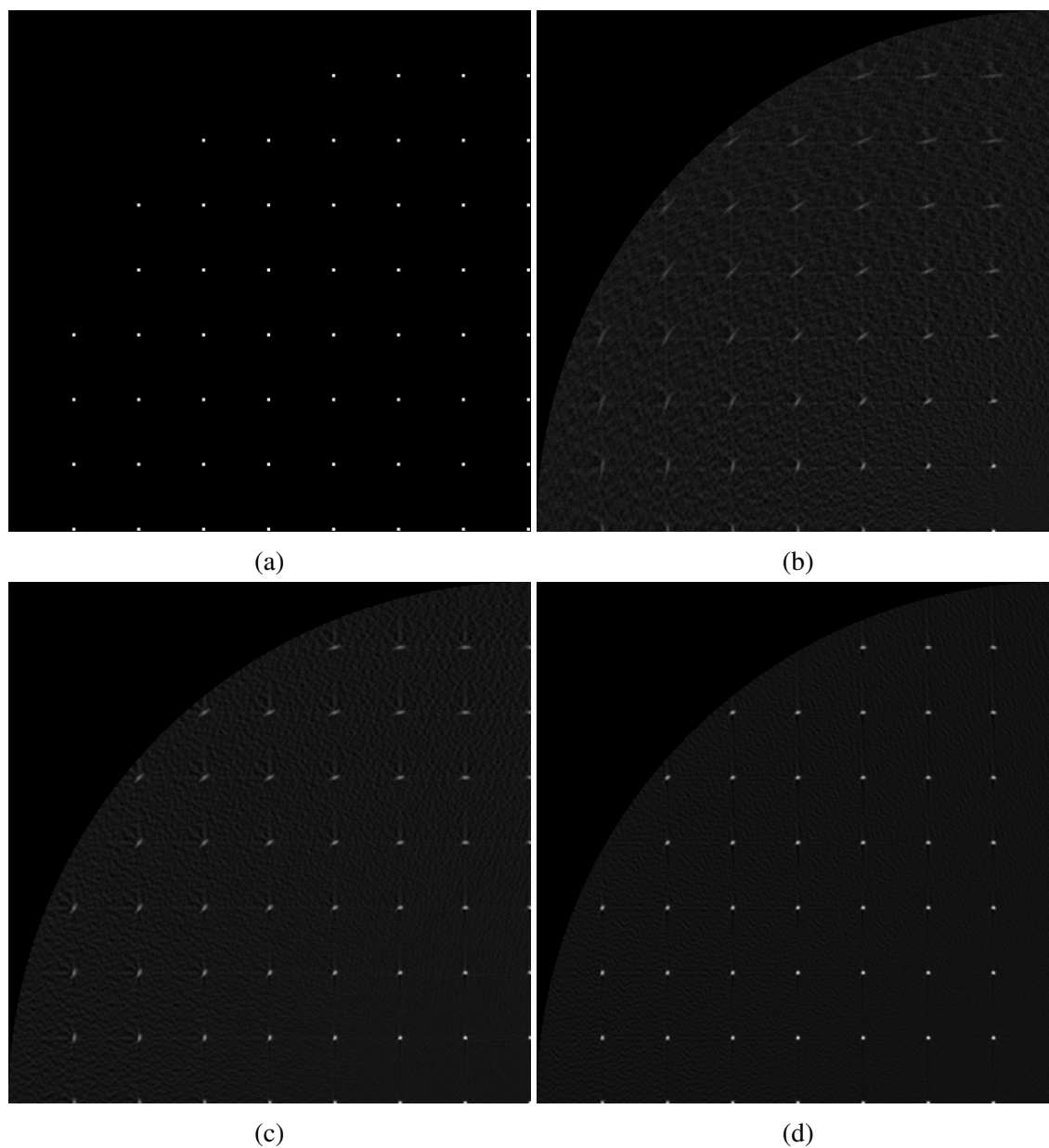


Figure 4.14: Images show upper left quadrants of (a) the simulated pattern phantom and the reconstructed images using (b) the simulated 30 fps sinogram, (c) the simulated 60 fps sinogram, and (d) the simulated 120 fps sinogram. The axis rotation corresponds to the bottom right corner of each image.

Qualitatively, the quadrants above can be compared to assess the degree of blurring. The gantry motion is notably lower in the reconstructions simulated with frame rates of 60 and 120 frames per second. However, much higher frame rates are possible with photon counting detectors such as the X-Counter Actaeon detector which has pixel sizes of $100 \mu\text{m}$.⁵³

For a quantitative comparison, line profiles were taken from columns in the blurred phantom features situated along the central row of the reconstruction. The amount of blur was again estimated by extrapolating along the blurred image back to the background. Below is a plot of the measured blurred BB diameters along with dashed lines showing the theoretical blur as predicted by equation 4.6. The average percent difference for measured blur vs maximum predicted blur was found to be 11.3%,⁵⁴ though artifacts, image noise, and pixelization may have negatively impacted this measurement.

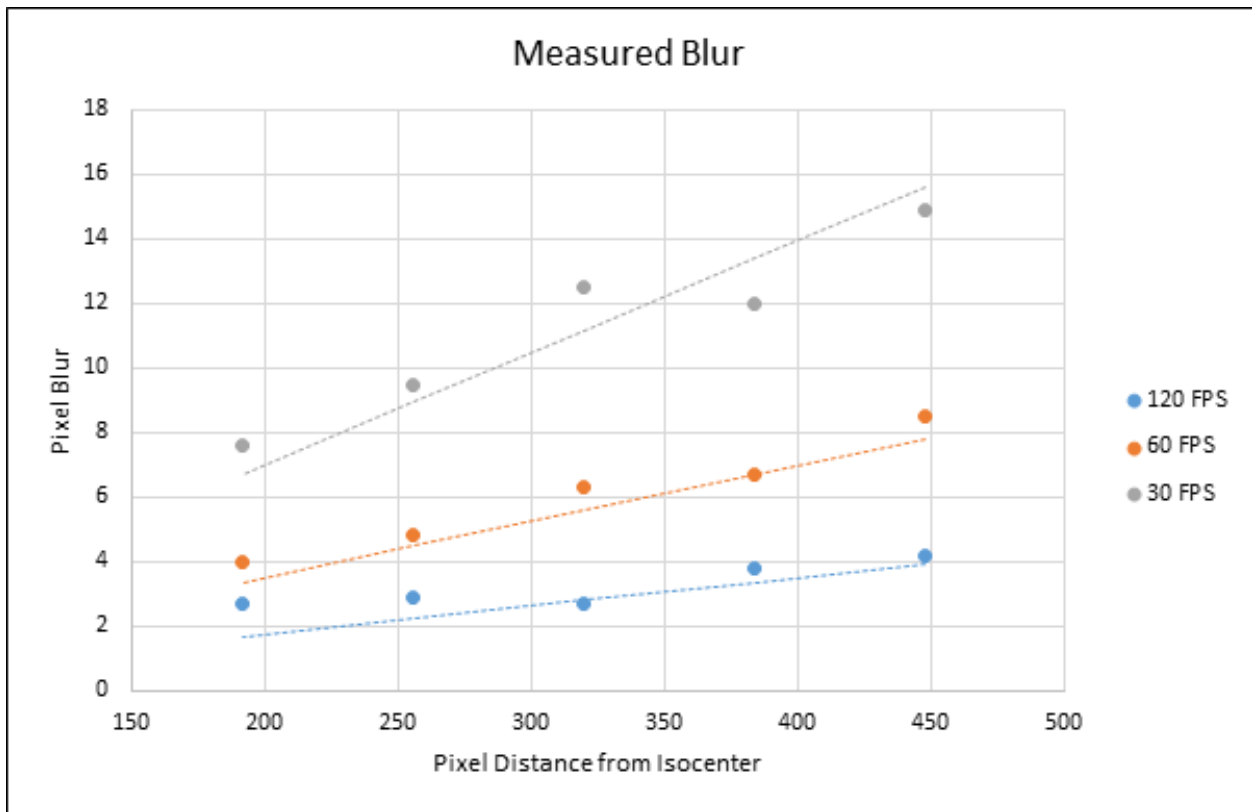


Figure 4.15: Blur measurements relative to simulated objects' distance from isocenter. Points are measured blur and dashed lines are the theoretically predicted blur values.

4.4 Discussion

Motion induced blur has the most severe impact on state of the art, high-resolution detectors when compared to most current detectors with large pixel sizes. For example, based on the same geometry from the experiment, for a frame exposure of 15 ms, a 3 cm distance from isocenter, and a 50°

s^{-1} angular velocity would result in an expected blur of around $400 \mu\text{m}$. For resolutions of 200 to $400 \mu\text{m}$ the blur would hardly be noticeable, for high-resolution detectors with 75 to $100 \mu\text{m}$ pixels that would amount to a blur across 4 to 6 pixels.

This work also points towards methods that may be used to minimize the effects of gantry motion-induced blur. Equation 4.6 points to several steps that may be taken, such as a reduction in frame acquisition time (through either shorter pulse lengths or high frame rates), positioning the region of interest as close to isocenter as is practical, and using lower gantry speeds whenever possible. Since patient centering and patient motion can be concerns during CT acquisition, moving the region of interest towards isocenter and lower gantry speeds may not always be advisable. Shorter x-ray pulses and higher frame rates should be suitable to accommodate most circumstances.

4.5 Conclusion

High resolution imaging may be critical during neuro-vascular and other interventions. The problem of blur due to rotational motion of a c-arm during CBCT with high resolution imagers has been analyzed and a model for predicting image blur has been developed. This model identifies key parameters that affect image blurring due to gantry motion, namely: gantry rotational speed, frame capture times/x-ray pulse duration, and magnification. Careful selection of the aforementioned parameters should reduce the impact of blurring in CBCT projections. The model has also been experimentally verified, showing good agreement between predicted blur and measured data.

The model was further applied to CT acquisition in which a regular pattern phantom was simulated, projection data was acquired, and projections were intentionally blurred for 3 simulated frame rates. The blurred sinograms were used to reconstruct the pattern phantom using filtered backprojection for all three data sets. A qualitative comparison showed significantly less blurring for higher frame rates. It was also shown that the blur can be predicted quantitatively with some error due to noise, reconstruction artifacts, and pixelization.

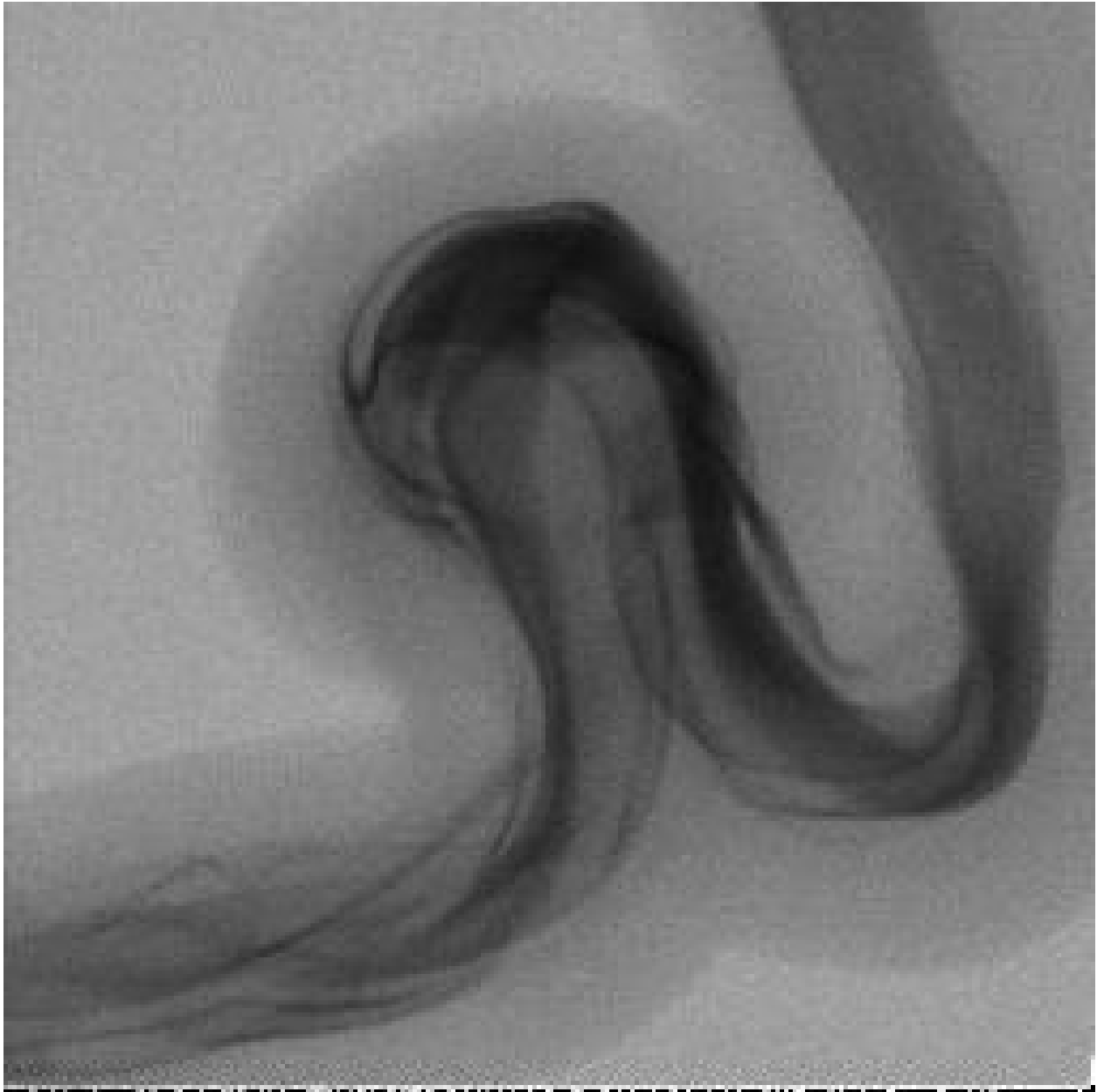
Chapter 5

Initial Investigations of 1000 FPS High Speed Angiography (HSA) and the Use of HSA in Endovascular Image Guided Interventions

5.1 Introduction

Hemodynamics contain important information that could impact neuro-interventional decisions and improve outcomes.⁵⁵ Conventional FPDs operating at 30 to 60 fps offer limited visualization of aneurysmal flow patterns due to insufficient temporal resolution. Many studies investigating the hemodynamics of intracranial arteries have made use of computational fluid dynamic (CFD)⁵⁶ simulations which use complex algorithms to recreate flow patterns as opposed to measuring them directly. While still extremely useful for displaying detailed hemodynamics, CFD is an approximation of flow conditions built on a number of assumptions and requires large amount of computational time to run simulations. There are currently no known methods for measuring patient blood flow detail during the course of an intervention. In this chapter we present a method that makes use

of High-Speed Angiography (HSA) to visualize the details of intracranial arterial hemodynamics during a neuro-interventional procedure. Video 5.1 shows an example of HSA image sequences that allow for the observation of blood flow patterns.



Video 5.1: Example of high speed images acquired at 1000 fps using HSA. Video also available at: <https://youtu.be/Urb0COsh-xw>.

The methods developed and presented in this chapter have been used to image detailed blood flow patterns in a variety of 3D printed aneurysm phantoms. A new high-speed, high-resolution

detector from Direct Conversion was used in conjunction with a mobile C-arm to image blood flow details in vascular phantoms with the use of iodine contrast. Efforts were made to maximize the number of frames that could be acquired and demonstrations are presented that illustrate the utility of HSA and its application to vascular flow imaging.

During this work we will focus on the disruptions to hemodynamics in and around aneurysms or stenotic vessels. One demonstration that will be presented herein is how the deployment of a flow diverter impacts blood flow in and around a saccular aneurysm. Exposure to the detector will be discussed briefly and the measured dose per frame (DPF) will be compared to other imaging procedures.

5.2 Materials and Methods

5.2.1 XCounter's Actaeon Detector

The detectors discussed previously in this work have been energy integrating detectors (EID). In an EID the signal in a pixel is proportional to the total energy ($\sum E \cdot N(E)$) collected by the light sensitive portion of the detector array. Energy integration results in loss of energy-dependent information such as the attenuation coefficients of different tissue types. EIDs also add electronic noise to images as well as swank noise⁵⁷ which degrade image quality. One final disadvantage of EIDs is that low energy photons that carry more contrast information than high energy photons are weighted less than high energy photons resulting in reduced contrast and a further increase in noise.⁵⁸

The detector used for this work is the XCounter Actaeon detector (Direct Conversion AB, Danderyd, Sweden), a photon counting detector (PCD) shown in figure 5.1. PCDs count individual photons incident on the detector and use pulse height analysis to discriminate between energy thresholds. Thus PCDs preserve some of the energy-dependent information and could enable simultaneous imaging of multiple contrast mediums if the detectors have four or more energy windows.⁵⁸ Although electron and swank noise are still present in PCDs they only affect the mea-

sured energy and not the signal intensity.⁵⁹ Finally, since events are counted instead of integrated, contrast is improved in PCDs.⁶⁰

PCDs do have some flaws. Due to limited pulse resolving times, nearly coincident photons can generate overlapping pulses that may be counted as a single event with energy equivalent to the sum of the two events. This error is known as pulse pileup and can result in lost counts and a distortion of spectral data.⁶¹ Other factors such as charge sharing and charge trapping can degrade the spatial and spectral response of PCDs.^{62,63,64} The Actaeon detector uses its high speed camera and software to compensate for some of these flaws such as with its anti coincidence circuitry (ACC) mode.



Figure 5.1: XCounter's Actaeon detector (Source: Direct Conversion).

The Actaeon is also a direct detector with an active layer of 0.75 mm thick CdTe layer. The CdTe layer has a density of 5.82 gm/cm^3 and 100% fill factor providing excellent intrinsic efficiency due to the high attenuation of CdTe. The Actaeon pixel pitch is $100 \mu\text{m}$, providing high spatial resolution, and the active area is a 256 by 256 pixel readout giving a total field of view of 1 inch by 1 inch. The Actaeon has two independent energy thresholds enabling dual energy acquisition. The readout is a complementary metal oxide semiconductor (CMOS) with readout

speeds of up to 1000 fps (the key feature of this detector). The manufacturer has listed the DQE(0) as greater than 80% for an RQA5 spectrum and an MTF of 80% at 2 lp/mm and 45% at 5 lp/mm. This group has further quantified much of the performance of the Actaeon detector.^{65,66,67,68} Due to the nature of the detector it is capable of low noise, high spatial resolution, and high temporal resolution images.

The Actaeon detector has various operating modes for imaging including High Sensitivity with ACC on, High Sensitivity with ACC off, High Flux without ACC, and High Power.⁶⁹ These modes enable the detector to operate at different photon flux rates with higher frame rates having reduced spectral accuracy. The detector can also be triggered with either a software trigger or an external pulse (to coincide with x-ray pulses). Other aspects of the imaging systems can be modified such as the number of energy windows recorded (one or two thresholds) and bit depth.

5.2.2 3D Printed Phantoms

Patient specific vascular phantoms have been used by this group for physician testing, training, and practice for patients with challenging anatomies.⁷⁰ Current methods used by this group make use of additive manufacturing (3D-printing) to rapidly produce patient-specific neuro-vascular phantoms used for endovascular surgical procedure planning and endovascular device research.

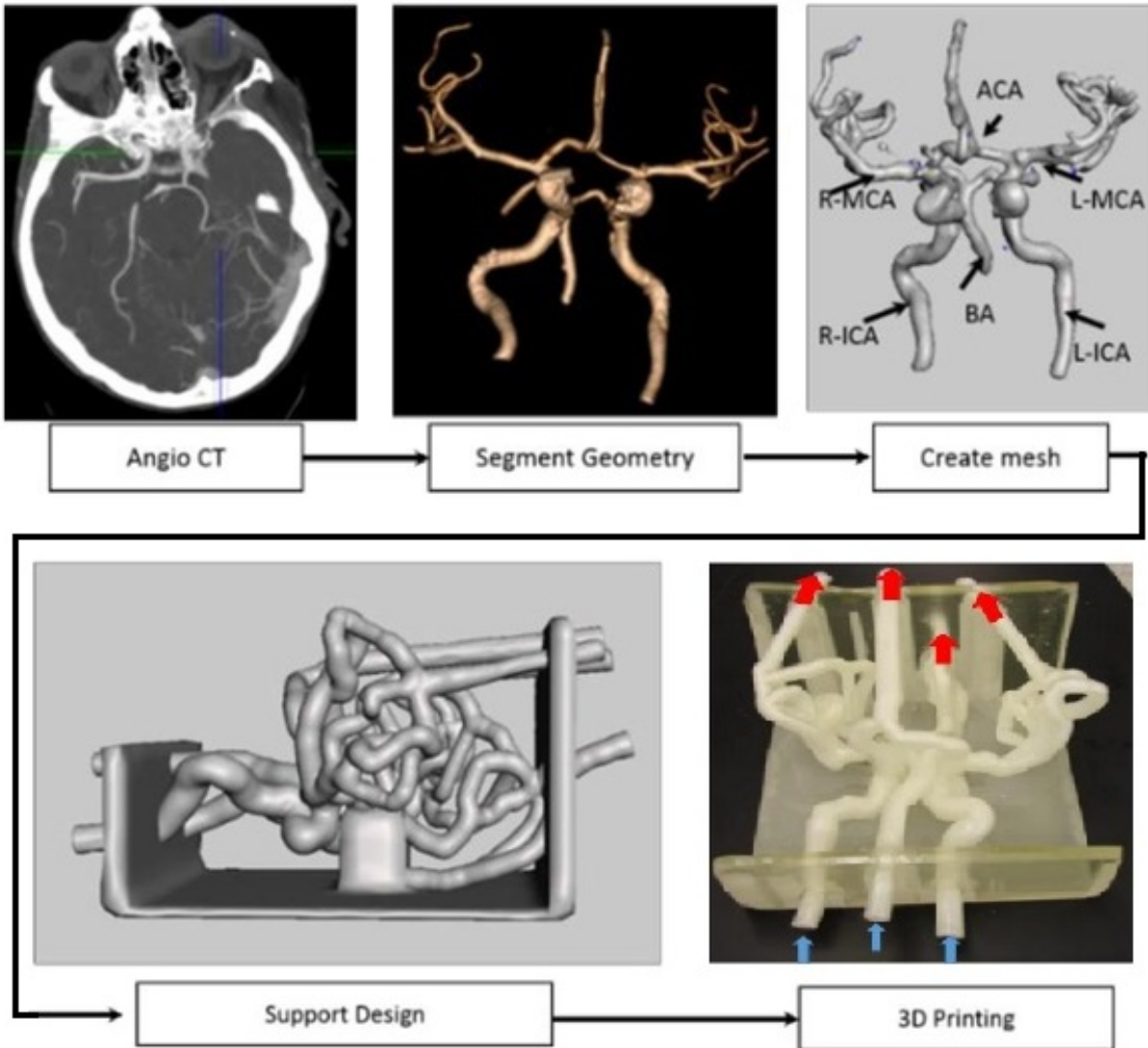


Figure 5.2: Flow chart illustrating the steps used to print patient specific phantoms.

The process for manufacturing 3D-printed phantoms⁷¹ begins by acquiring patient data via either CT, MRI, or CBCT scans of the relevant patient anatomy. The acquired patient data is then loaded into a Vitrea 3D station (Vital Images, Inc., Minnetonka, MN) for rendering and processing. The relevant anatomy can then be segmented from surrounding structures and simplified by removing smaller, superfluous vessels. These models are then imported into a mesh manipulation software (www.MeshMixer.com) to merge inlets and outlets for practical use in a flow loop. Vessel wall thickness and vessel lumen diameter can then be altered to meet design requirements

and a support structure may be added if needed. Once the model is complete, the phantom is printed on an Objet Eden 260V Polyjet 3D printer (Objet-Stratasys Inc., Eden Prairie, MN).⁷² For convenience this process has been illustrated in figure 5.2.

The Objet Polyjet printer (shown in figure 5.3) is capable of printing up to 17 different materials with layers as thin as 16 μm for rigid materials and 32 μm for flexible materials. The patient-specific vascular phantoms are printed in semi-transparent elastic material called Tango+ with VeroClear used to provide support when necessary.



Figure 5.3: Objet Eden 260V Polyjet 3D printer (Source: Stratasys).

For this experiment, five 3D printed phantoms were used to examine flow patterns. These phantoms are shown in figure 5.4 and are listed as followed: (A) patient-specific bifurcated carotid artery, (B) patient-specific internal carotid artery with idealized (artificially added partial sphere) saccular aneurysm, (C) patient-specific internal carotid artery with wide-necked saccular aneurysm, (D) patient-specific basilar-tip saccular aneurysm, (E) and idealized (this geometry was generated manually with cylindrical tubes and hollow spheres) basilar-tip saccular aneurysm.

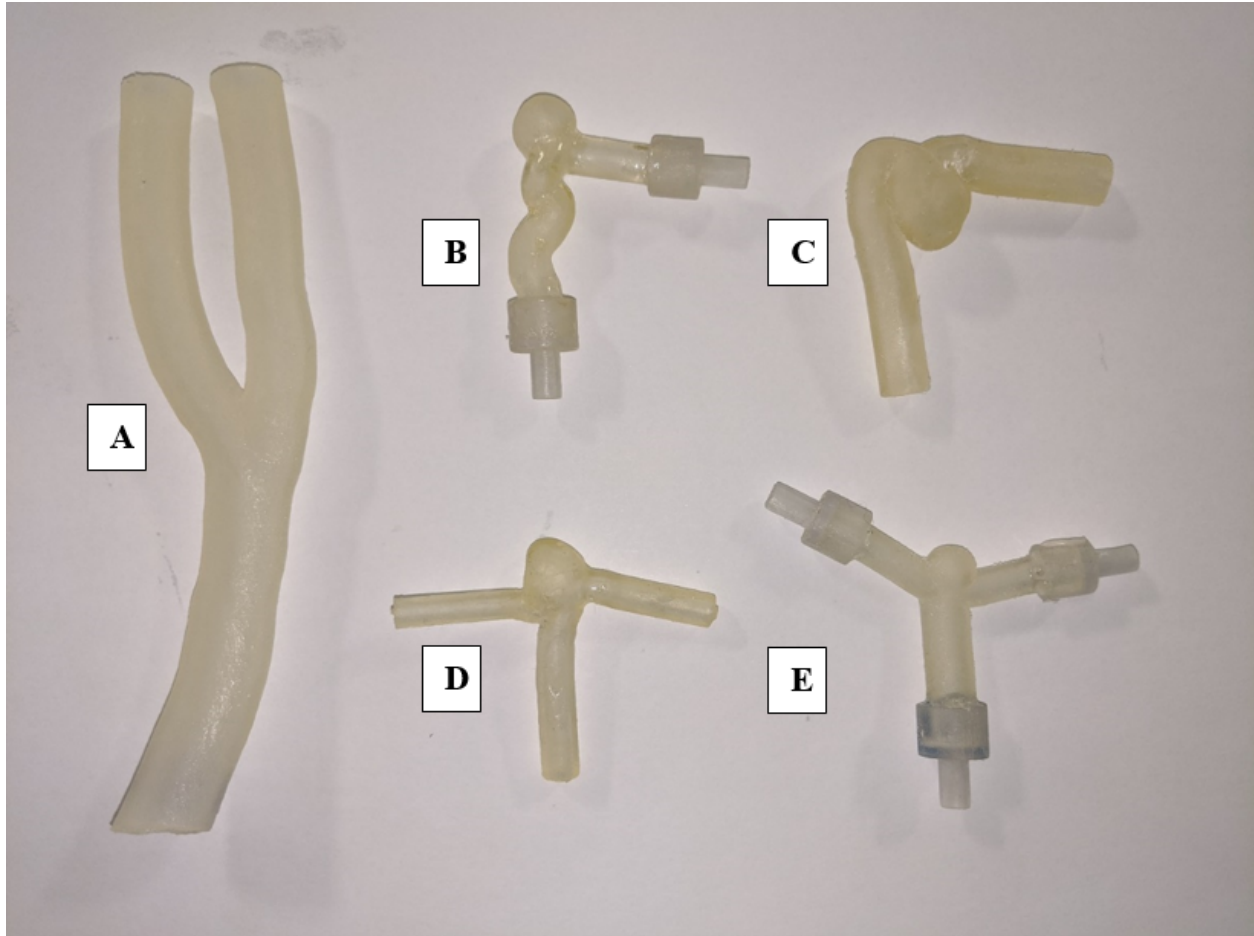


Figure 5.4: 3D printed phantoms used to illustrate flow patterns using HSA imaging. Phantoms are described in the text above.

5.2.3 Experimental Setup

The 3D printed phantoms were placed on plastic platform to prevent movement and placed below the Actaeon detector at a 1.1 x magnification phantom. Phantoms were placed in a flow loop using water as the blood simulating fluid. The phantom was connected to a fluid reservoir, a pump, and dampeners using rubber tubing with pressure clamps added to adjust the flow pressure and velocity to clinically relevant values. A diagram of an example flow loop is shown in figure 5.5. For the majority of this experiment a cardiac pump was used to drive flow, though occasionally a constant-flow, peristaltic pump was also used.

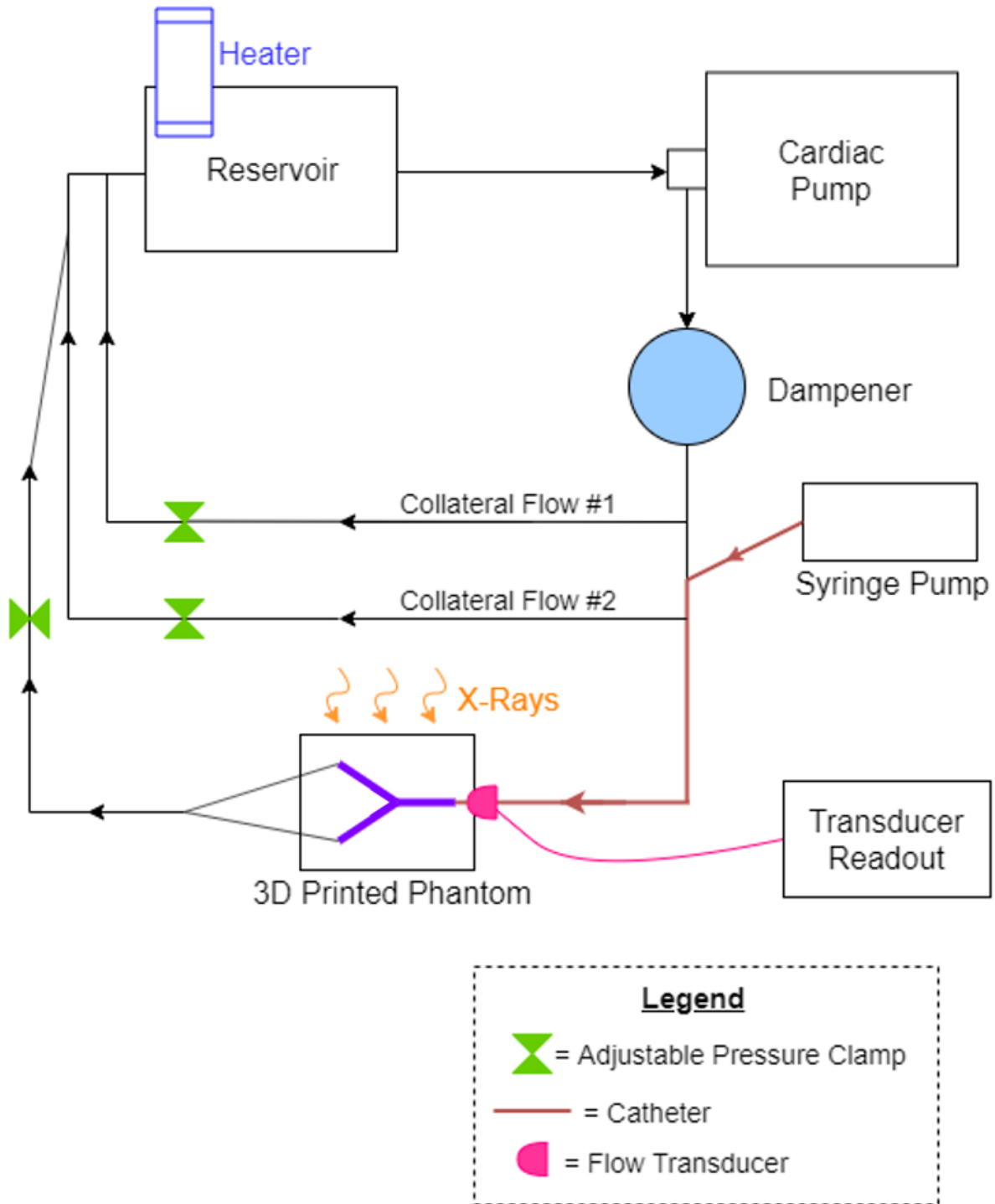


Figure 5.5: 3D printed phantoms used to illustrate flow patterns using HSA imaging.

The x-ray source in this experiment was either a Surginix SXT-2000A mobile C-Arm (Canon Medical Systems Inc, Otawara, Japan) or an Alphenix INFX-8000V (Canon Medical Systems

Inc, Otawara, Japan). Digital Angiography (DA) technique parameters were adjusted along with detector settings to maximize the number of acquired frames and achieve optimal imaging of flow patterns. Iodine contrast was injected either manually or using an autoinjector (Medrad PPD11060507, Medrad Inc, Warrendale, PA) via a catheter proximal to the region of interest.

The Actaeon detector was triggered manually in its High Sensitivity without Anti-Coincidence Circuitry mode. Images were stored and flat-field corrected for display when flat-field images were available.

5.3 Results

5.3.1 Initial Visualization of Flow Patterns Using 1000 FPS HSA

Initial images were acquired using the Infinix C-arm using a DSA protocol with a maximum exposure pulse width of 100 ms with a medium focal spot. Some early images acquired with the Actaeon detector have a line showing the division between detector modules. Images acquired later took steps to correct for this and other artifacts. Following image acquisition, 100 consecutive 1 ms frames were averaged together to provide a comparison between 1000 fps HSA and its equivalent DA image. A single frame from each acquired images is shown in figure 5.6 and shows differences in quantum noise. Figure 5.6a demonstrates that HSA images display noise characteristics similar to those of fluoro images, but the temporal resolution of these images is substantially better when compared to its DA counterpart shown in figure 5.6b which shows significant motion blur due to contrast movement.

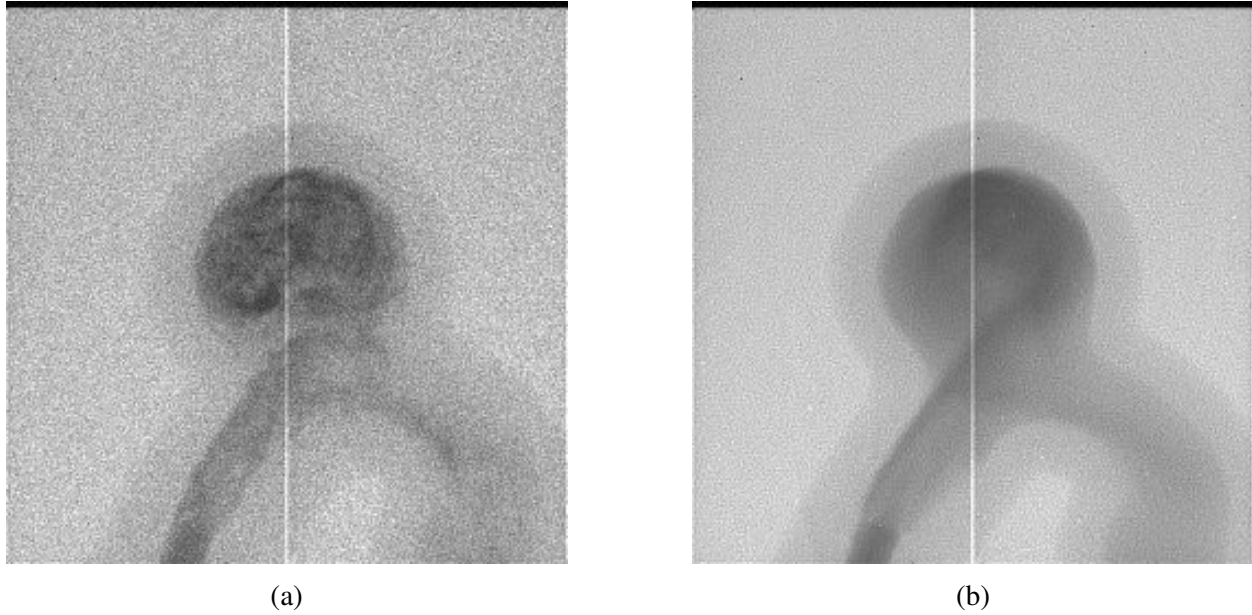
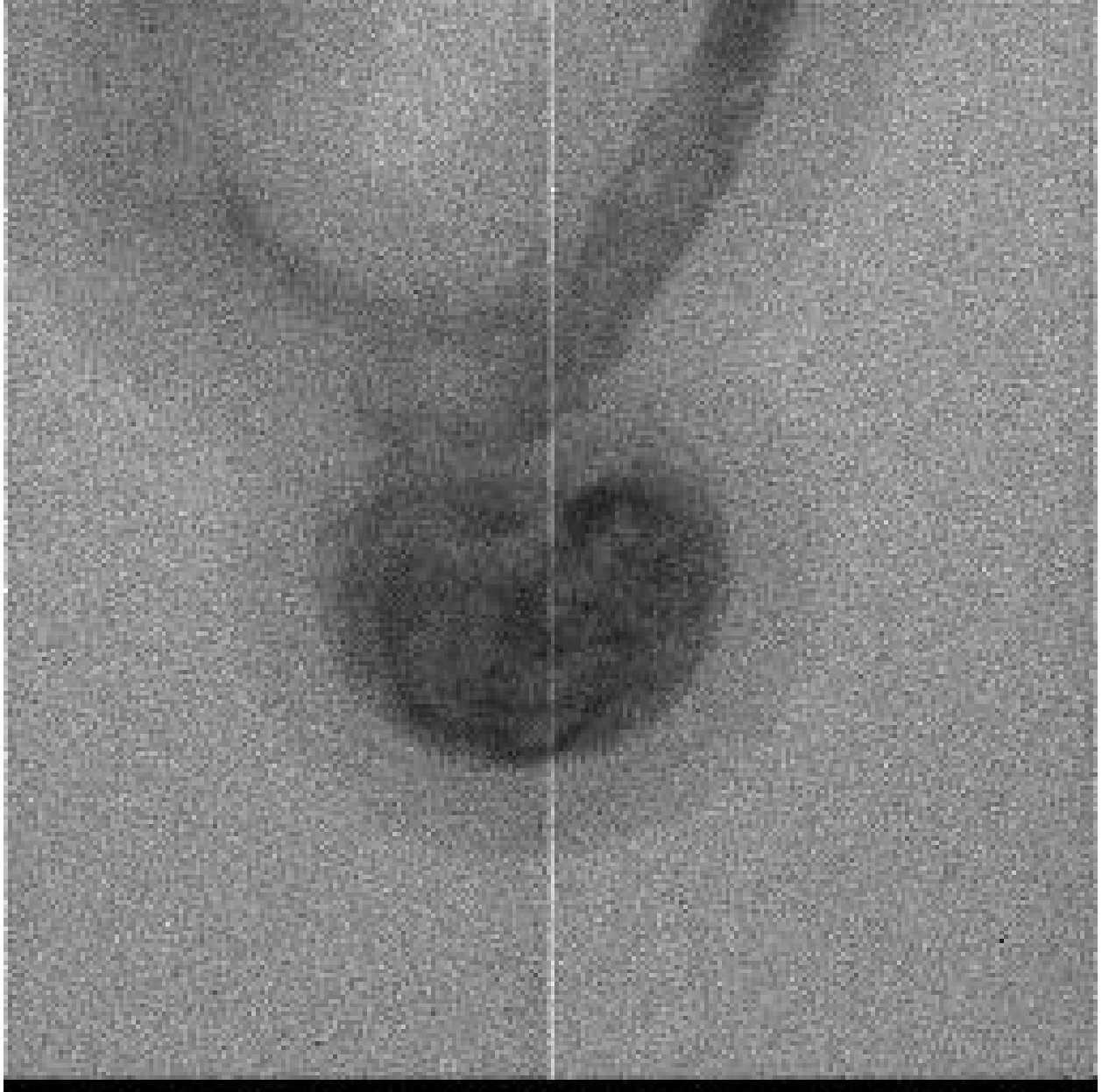
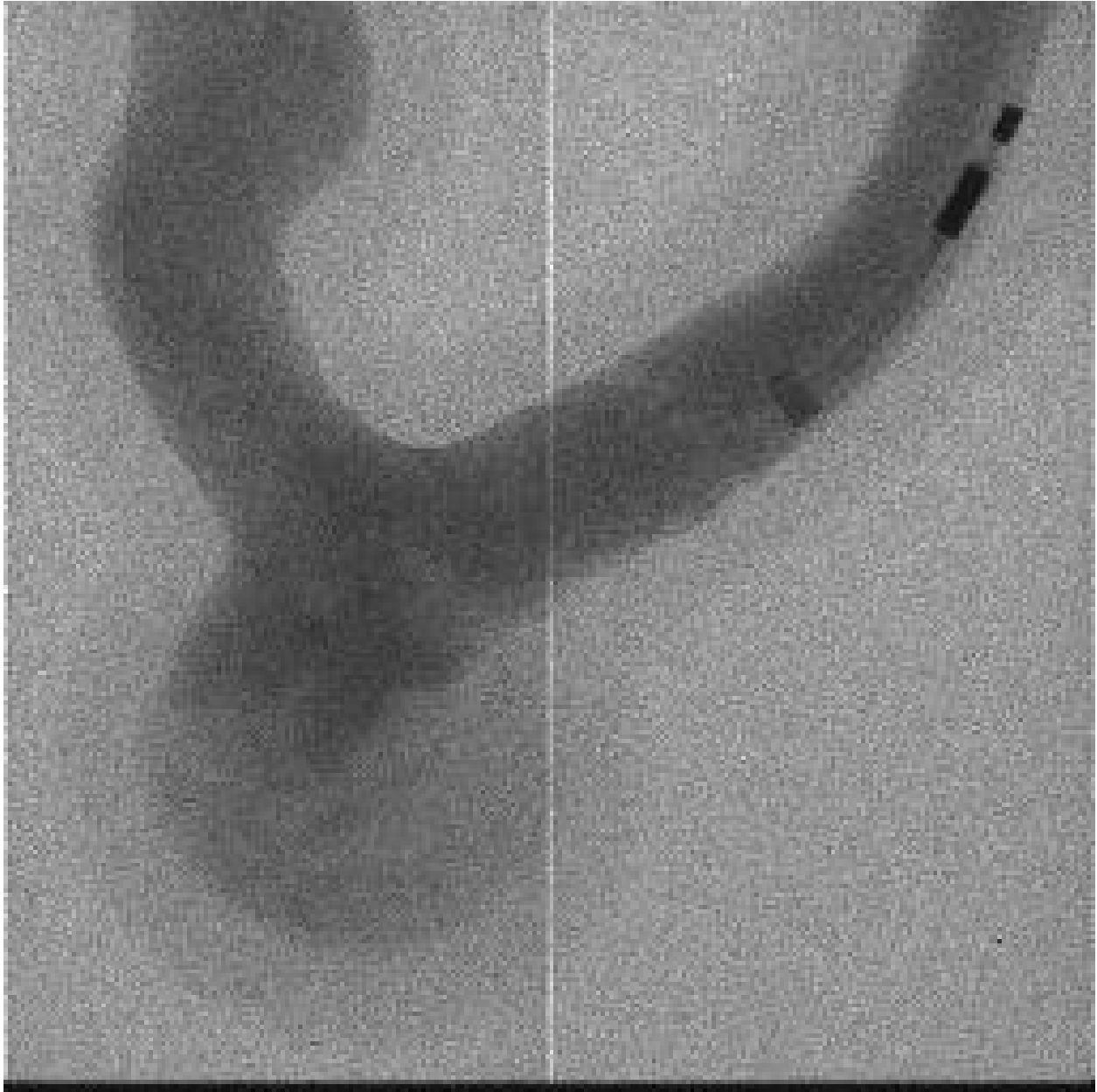


Figure 5.6: Images showing (a) a single frame acquired at 1000 fps HSA and (b) a DA image simulated by integrating 100 consecutive HSA frames.

To observe the effects of a deployed interventional device on vascular flow a flow diverting pipeline stent was deployed across the neck of a 3D printed saccular aneurysm phantoms (phantom B from figure 5.4). HSA images were acquired using the method described above. Since the pulse length was limited to 100 ms the following images sequences are also limited to just 100 frames. Video 5.2 shows the flow detail in the phantom before stent deployment and video 5.3 shows the flow detail following the deployment of the pipeline stent. Without the flow diverter in place 1000 fps HSA clearly shows flow into the aneurysm with the development of vortices of contrast in the aneurysmal sack. Images acquired with a flow-diverter in place show more diffuse flow of contrast into the aneurysm with lower apparent flow velocities and delayed development of vortices in the aneurysm sac.⁷³



Video 5.2: 1000 fps HSA video showing blood flow detail in a saccular aneurysm phantom before treatment. Video also available at: <https://youtu.be/7vMbosANtFg>.



Video 5.3: 1000 fps HSA video showing blood flow detail in a saccular aneurysm phantom after treatment with a pipeline embolization device flow-diverter. Video also available at: <https://youtu.be/kJ3zjgIsIA4>.

5.3.2 Increasing Imaging Timing Window

Due to hardware limitations and a need to manually trigger x-ray exposure, contrast injection, and image capture time, HSA sequences were limited to 100 ms continuous imaging windows interspersed between sections of no x-ray exposure. These short timing windows prevent the un-

interrupted observation of flow details over long injections, or over full cardiac cycles. In order to increase the timing window a new source and further experimentation with the Actaeon's onboard memory were employed.

The new source used is the Surginix SXT-2000A mobile C-Arm from Canon. This mobile C-arm was capable of producing a 3s continuous x-ray burst at 70 kVp and 100 mA. Limitations in on-board detector memory further limits the total number of images that can be acquired at 1000 fps. Making use of both energy thresholds and the highest bit depth of the x-ray detector (16 bits) available enables up to 1200 images to be acquired at 1000 fps. By adjusting imaging parameters the number of acquired images can be increased further to ensure the entire cardiac cycle is captured. Table 5.1 lists the number of images that can be acquired for various imaging parameters.⁷⁴

1000 FPS HSA		
# Energy Thresholds	Image Bit Depth	Max Number of Frames
2	16-bit	1200
2	8-bit	2400
1	16-bit	2400
1	8-bit	4800

Table 5.1: Limitations on the number of frames due to current limitations in the Actaeon's on-board memory.

Through experimentation it was found that 8-bit was often insufficient, as it limited counts to 255 maximum. Given that this team is not making use of the dual energy capabilities of the Actaeon for this project the combination of 1 energy threshold at 16-bit image depth was ideal for maximizing the use of the Actaeon's current on-board memory.

Videos 5.4 and 5.5 contain 0.25 s of HSA data acquired with both pulsed and continuous x-ray exposure. The videos demonstrate the impact that a longer timing window can have on the proper visualization of vascular flow detail. Video 5.4 shows the images acquired with a DSA sequence with 83 ms pulse width followed by 83 ms between x-ray pulses. Between x-ray pulses much

flow information is lost that may serve to further inform interventionalists' decisions. Video 5.5 however shows the full flow detail that can be acquired using a continuous exposure.



Video 5.4: 1000 fps HSA video showing blood flow detail in a saccular aneurysm phantom. Flow dynamic visualization limited by short x-ray pulses (83 ms) and limited duty cycle (50%). Video also available at: <https://youtu.be/gL1LV7wZfQo>.



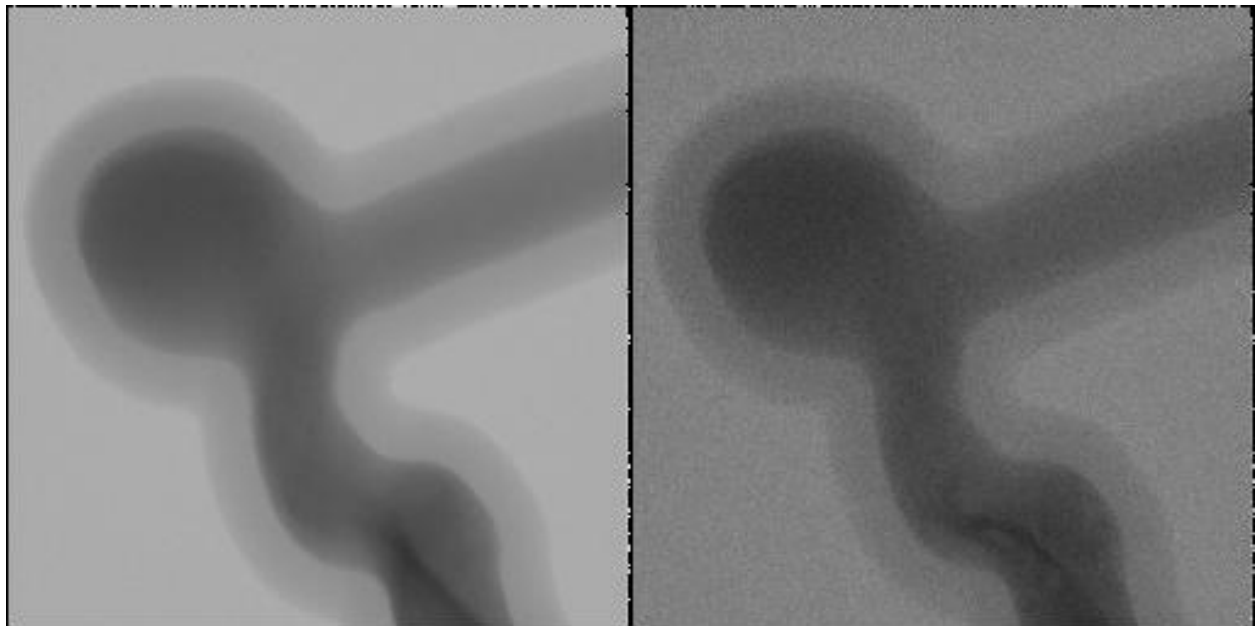
Video 5.5: 1000 fps HSA video showing blood flow detail in a saccular aneurysm phantom. Flow dynamic visualization improved by continuous x-ray exposure for 3 s. Video also available at: <https://youtu.be/1pIksOL11P8>.

5.4 Discussion

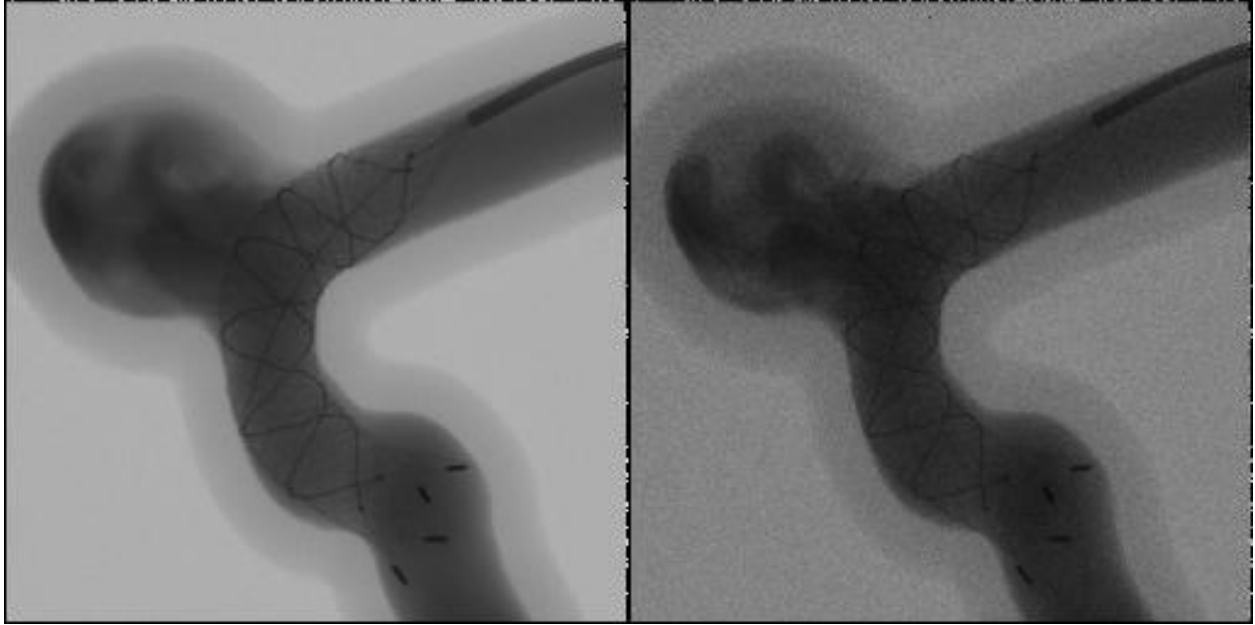
1000 fps has several advantages over conventional digital angiographic methods, the greatest advantage being the ability to view vascular flow detail that may help guide interventionalists' deci-

sions during a procedure. Dose for HSA images was measured to be in the range of 100s of nGy to a few μGy per frame at the detector surface depending on the amount of attenuating material in the beam. Furthermore, since images were acquired using DA and DSA sequences the total dose to a patient would also be equivalent to a DA or DSA sequence as well while still providing fluoro quality images.⁷⁵

Though HSA capable detectors are not widely available there is still the potential to implement HSA in the clinic. As mentioned in Chapter 2, this group has in the past made use of separate detectors that could be moved in and out of the x-ray beam field to enable high resolution fluoroscopy (HRF). A similar method could be used to deploy a small field HSA enabled detector during an interventional procedure. The data acquired by the HSA enabled detector could also be used to produce conventional DA/DSA sequences by integrating HSA frames, thus providing both HSA and DA/DSA data simultaneously.⁷⁶ Videos 5.6 and 5.7 show simultaneously acquired HSA and DA data of a 3D printed aneurysm phantom before and after treatment with a pipeline flow-diverter.



Video 5.6: HSA and DA images acquired simultaneously using the Actaeon detector. HSA images displaying flow details in the 3D printed aneurysm before treatment are shown in the images to the left while the right shows the DA images simulated from the HSA images and are played simultaneously for comparison. Video also available at: <https://youtu.be/m8wkeYdCqoY>.



Video 5.7: HSA and DA images acquired simultaneously using the Actaeon detector. HSA images displaying flow details in the 3D printed aneurysm after treatment are shown in the images to the left while the right shows the DA images simulated from the HSA images and are played simultaneously for comparison. Video also available at: <https://youtu.be/rBc3qCOD08U>.

5.5 Conclusion

High-speed imaging, enabled by this new detector, allows clinicians to observe detailed flow patterns in the 3D printed phantom, including changes in flow patterns for treated aneurysms. These gains in temporal information could inform treatment decisions by allowing clinicians to assess flow patterns in real time. At the time of treatment, clinicians assess adequacy of stent placement by looking for indirect signs of flow diversion, such as evaluating for wall apposition and looking for contrast status within the aneurysm sack. Detailed visualization of changes in flow dynamics could allow clinicians to directly assess factors that have been shown to improve efficacy of flow diverters, such as decrease in flow vortices. Other potential clinical use cases include the detection of endoleaks near an aneurysm, identification of residual flow that could cause an aneurysm to regrow, blood impingement patterns that could lead to coil compaction, and diversion of jets into an aneurysm at locations where flow may be less intuitive (such as a bifurcation).⁷³

Given the state of current technology HSA may soon be integrated into the clinic for simultaneous use during DA and DSA image acquisition. However, new developments in x-ray tube technology may enable long exposures, allowing for extended observations of detailed vascular flow with high spatial and temporal resolution throughout a contrast injection. While the cost in exposure to the patient may appear substantial, this group believes that the flow information provided by short HSA image acquisitions could improve diagnosis, treatment planning, and assessment of device deployment during interventional procedures.

Chapter 6

Quantification of Blood Flow Velocities

Acquired with HSA Sequences

6.1 Introduction

As minimally invasive image-guided endovascular interventions continue to replace invasive surgical procedures, quantification of parameters for impact evaluation such as blood velocity distributions and their changes due to the deployment of interventional devices become more important. Computational flow dynamics (CFD) has often been used to provide insight to physicians in planning and performing treatment of certain neurovascular diseases. However, CFD is computationally expensive and is not used for most patient planning. Furthermore, the time required for a full CFD simulation is impractical for emergency situations where flow detail could be of even greater import. This group has been working to develop unique methods using high spatial and high temporal resolution detectors to analyze 1000 fps HSA sequences and measure such blood velocities in intracranial vessels.

Three methods for measuring blood flow have been used. The first makes use of manually tracking of positional data of Iodine contrast as it moves through vessels to calculate blood flow velocity. The second method uses radio-opaque particles that are manually tracked through the

vessel. The third and final method, improves on the second by automating the tracking of the radio-opaque particles to quickly (and in a very computationally inexpensive method) provide real time data regarding flow in vessels. These methods are currently limited to 2D velocity measurements. The final method was used to assess the impact of varying frame rates on the accuracy of flow measurements. Though still in the early stages of development, these methods show potential to aid physicians in making difficult decisions.

6.2 Materials and Methods

All of the methods for quantifying blood flow use the same experimental setup. The same Surginix SXT-2000A mobile C-Arm (Canon Medical Systems Inc, Otawara, Japan) used for HSA experiments in chapter 5 was used for the experiments in this chapter. Iodine contrast was injected through a catheter using an auto-injector (Medrad PPD11060507) and the radio-opaque particles were manually injected through a catheter. 3D printed phantoms were placed in a flow-loop to simulate blood flow in vascular phantoms with adjustable pressure clamps to approximate vascular pressure and flow velocity. A dampener was also added to the flow-loop to reduce the periodicity of the cardiac pump and remove air from the system. The Actaeon XCounter was used to acquire HSA image sequences to quantify blood flow.

6.2.1 HSA Quantitative Flow Analysis

A patient specific 3D printed internal carotid artery phantom with idealized saccular aneurysm (figure 6.1) was used to image flow effects in this experiment. Contrast was injected into the phantom using the auto-injector approximately 5 cm proximal to the aneurysm to reduce the impact of the catheter and injection on vascular flow. HSA images were acquired using 1000 fps and images were flat-field corrected and stored.



Figure 6.1: Picture of the 3D printed aneurysm phantom used to develop methods for flow measurements.

Temporally successive images were subtracted to provide a difference image that highlights the movement of contrast as shown in figure 6.2. Subtracting successive frames created images in which darker regions correspond to sections into which contrast has moved and lighter regions correspond to sections from which contrast has left.

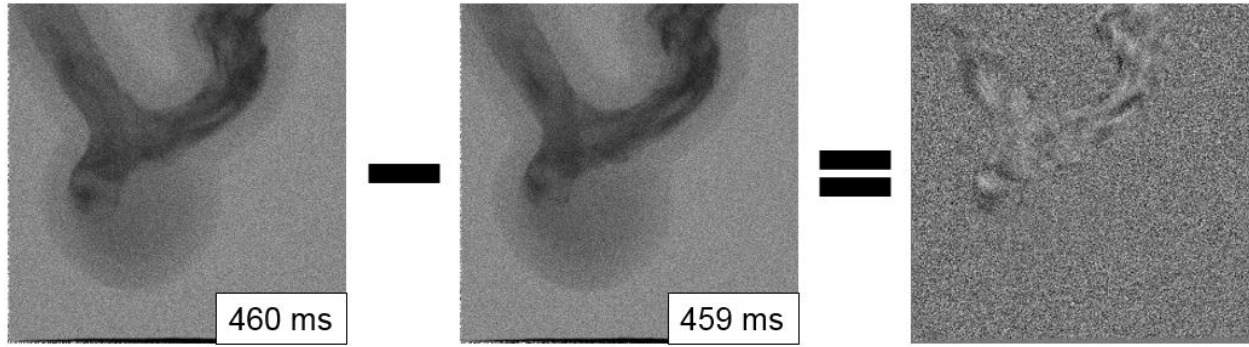


Figure 6.2: Method for producing difference images in which successive images are subtracted from one another to highlight the flow of iodine contrast.

In order to measure velocity the dark sections of contrast were tracked. The approximate center of the contrast front was manually selected. The sequences was a few frames and the center of the same contrast front was estimated again. The positional data was stored along with the frame number. Measurements were taken across the entire geometry of the vascular phantom. The euclidean distance, magnification, and change in frames was used to calculate the velocity of the contrast wave according to the following equation:

$$v = \frac{100\mu m \cdot \sqrt{(x_2 - x_1)^2 + (y_2 - y_1)^2}}{m \cdot (t_2 - t_1)} \quad (6.1)$$

where (x_1, y_1, t_1) is the initial measured position and time, (x_2, y_2, t_2) is the final measured position and time, and m is the geometric magnification of the x-ray image. The velocity data was then mapped to the x-ray image for display.

6.2.2 Performing X-Ray Particle Image Velocimetry (X-PIV) with HSA

Particle image velocimetry (PIV) is an optical method for measuring fluid flow. In PIV experiments a fluid is seeded with tracer particles that are tracked between two frames separated by very little time. X-ray particle image velocimetry (X-PIV) makes use of similar principles to image radio-opaque particles that are injected into the phantom.

The radio-opaque particles were Embospheres (Merit Medical Systems, South Jordan, Utah). These particles are small gelatinous spheres measuring 700-900 μm in diameter and are used clin-

ically to embolize vessels connected to cancerous tumors. To prepare the particles (which have radiographic properties similar to tissue) for injection, they were placed in undiluted iodine contrast (300 mgI/ml) for a minimum of 3 days. The particles were then loaded into a syringe with minimal contrast agent and saline solution. In order to preserve the particles' radio-opacity, particles need to be injected quickly after being removed from the iodine contrast agent. Particles were again injected approximately 5 cm proximal to the site of interest to reduce the impact of the injection on particle velocities.

Images were again acquired at 1000 fps and flat-field corrected. Recorded images were used to measure vascular flow via two methods: manual particle tracking and automated particle tracking.

For manual particle tracking the corrected images were loaded into a custom application where a user could navigate between frames and track the center of individual particles through consecutive frames as they moved through the vessel. This particle positional and temporal data was used to calculate blood flow velocities according to equation 6.1 again. This velocity data was again mapped to the x-ray image for display.

For automated particle tracking, particles were tracked using the open-source code trackpy.⁷⁷ The trackpy code was added to another custom application that allowed users to window and level particle images and adjust variables (minimum particle brightness, particle size, particle travel threshold, and track memory) used by trackpy on the fly to optimize the application's ability to identify the particles for each sequence. Trackpy identified particles and, using user provided parameters, connected identified particles between frames into trajectories. This particle tracking method yielded thousands of individual velocity measurements across the entire phantom for the image sequences which was once again mapped to the x-ray image for display.

Histograms of velocity data acquired using manual and automatic measurement methods were compared to verify the automated velocity measurement data.

6.2.3 Impact of Frame Rates on X-PIV

To assess the impact of frame rates on the accuracy of X-PIV four additional frame rates were simulated beyond the initial 1000 fps for the internal carotid artery with wide-necked aneurysm phantom. To simulate the frame rates two, three, four, or five consecutive frames were summed together. This produced identical image sequences of 1000, 500, 333, 250, and 200 frames per second. X-PIV was performed on the 1000 fps image sequence to measure the ground truth of the image sequence.

X-PIV was then performed for each of the lower frame rate sequences. A qualitative comparison was made between velocity maps. Average velocities were calculated for all space and time and histograms were plotted comparing the relative frequency of velocity measurements made for the different frame rates relative to the ground truth (1000 fps X-PIV).

6.3 Results

6.3.1 HSA Quantitative Flow Analysis

The image sequence used for HSA quantitative flow analysis is shown in video 6.1. Video 6.2 shows the corresponding difference image sequence used to measure flow analysis.

232 individual measurements were sampled from the image sequence corresponding to different points of time and different locations throughout the phantom having varying vessel diameter using the method laid out in the materials and methods section. The data was filtered to remove extreme outlier velocity measurements resulting in 191 individual velocity measurements. These velocity measurements were then plotted on a x-ray image of the aneurysm phantom with arrow length corresponding to velocity magnitude. For this study, the average measured velocity for points sampled from the inflowing portion of the vessel was found to be 91.7 cm/s while for the outflow vessel the average velocity was 135.3 cm/s due to its reduced diameter. Points measured within the aneurysm sac had an average velocity of 80.0 cm/s, though directionality was highly

dependent on location.⁷⁸ The image with plotted velocity measurements is shown below in figure 6.3.

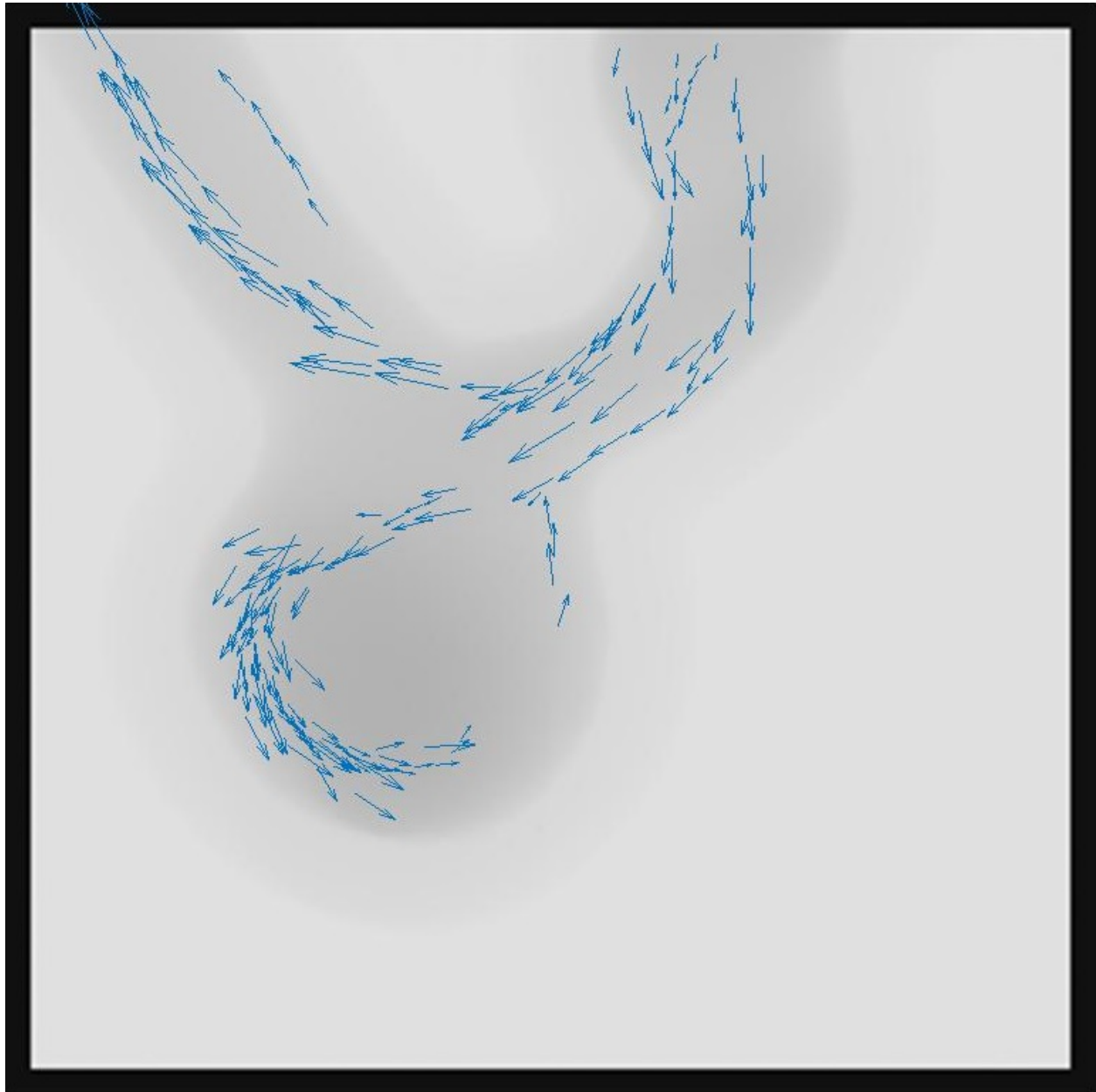
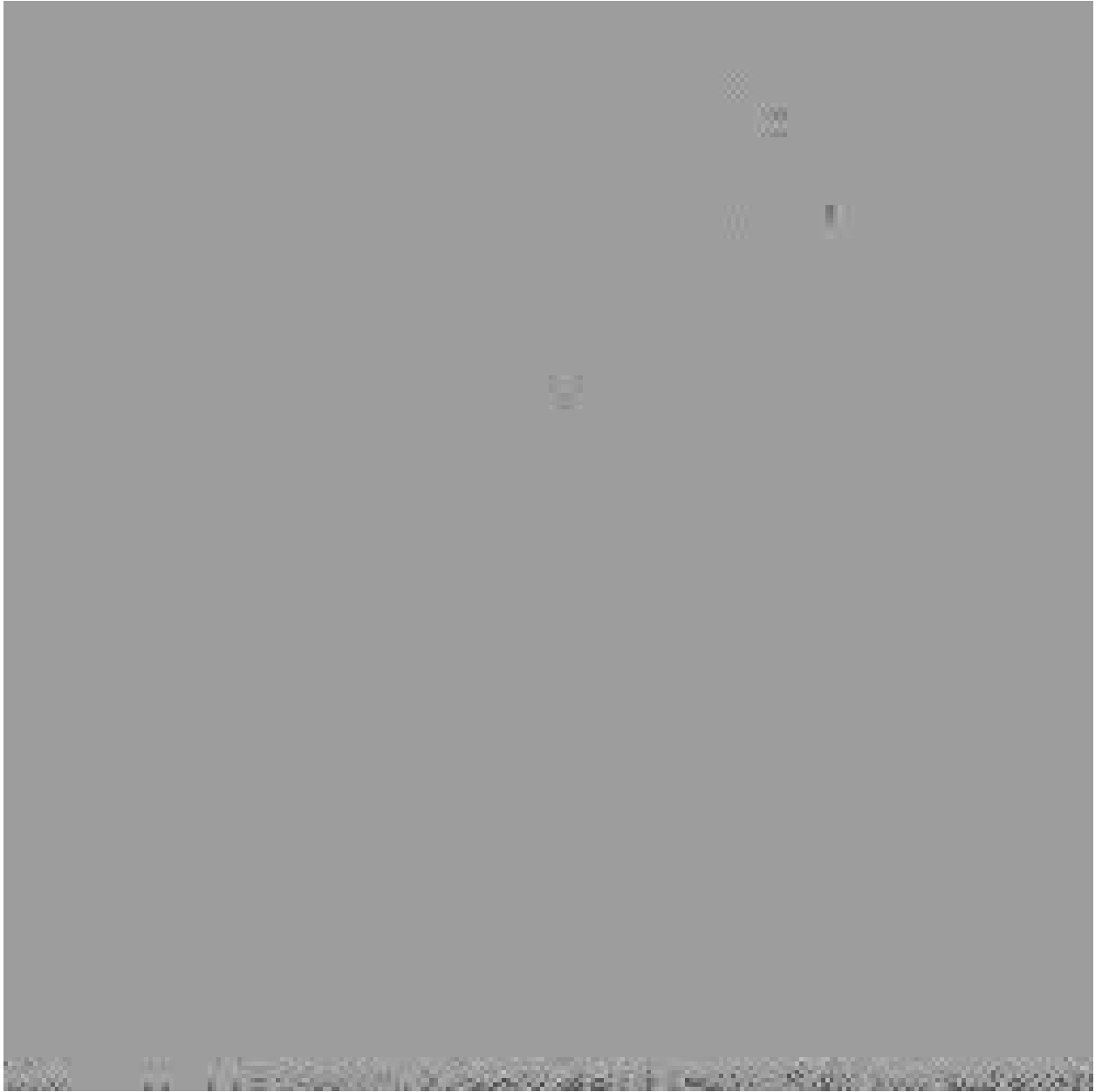


Figure 6.3: Velocity vectors plotted on projection image of 3D printed aneurysm phantom.



Video 6.1: HSA sequence used to quantify blood flow using manual measurements of difference images obtained during iodine contrast injection. Video also available at: <https://youtu.be/rm53uyBDubQ>.



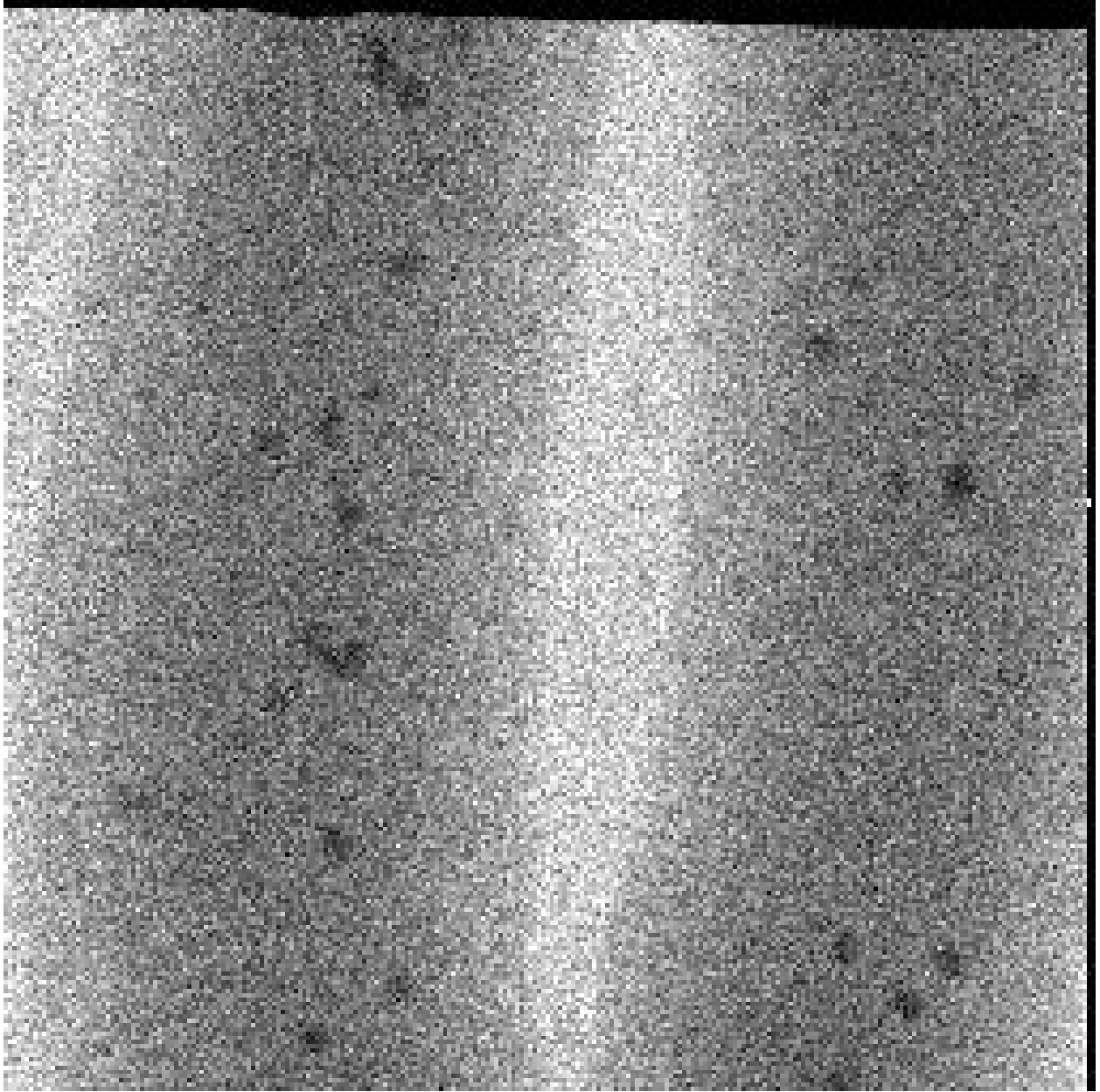
Video 6.2: HSA sequence used to quantify blood flow using manual measurements of difference images obtained during iodine contrast injection. Video also available at: <https://youtu.be/ww79pD6amBg>.

6.3.2 Performing X-Ray Particle Image Velocimetry (X-PIV) with HSA

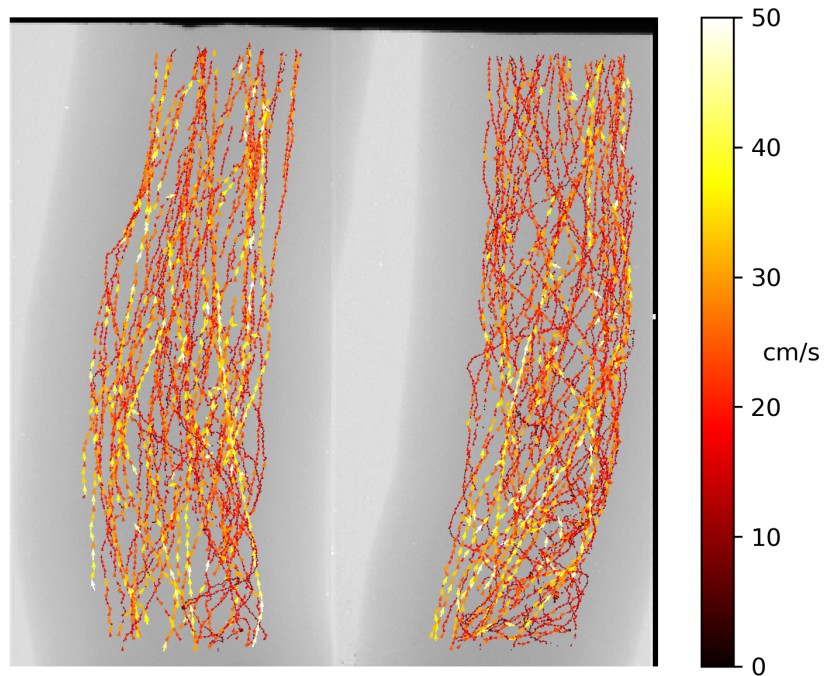
Figure 6.4 shows the automated measurements of flow in the bifurcated carotid phantom (see figure 5.4A) made using the trackpy software. Arrow length and brightness indicate velocity magnitude.

Figure 6.4a shows raw velocity measurements and contains 11277 individual velocity measure-

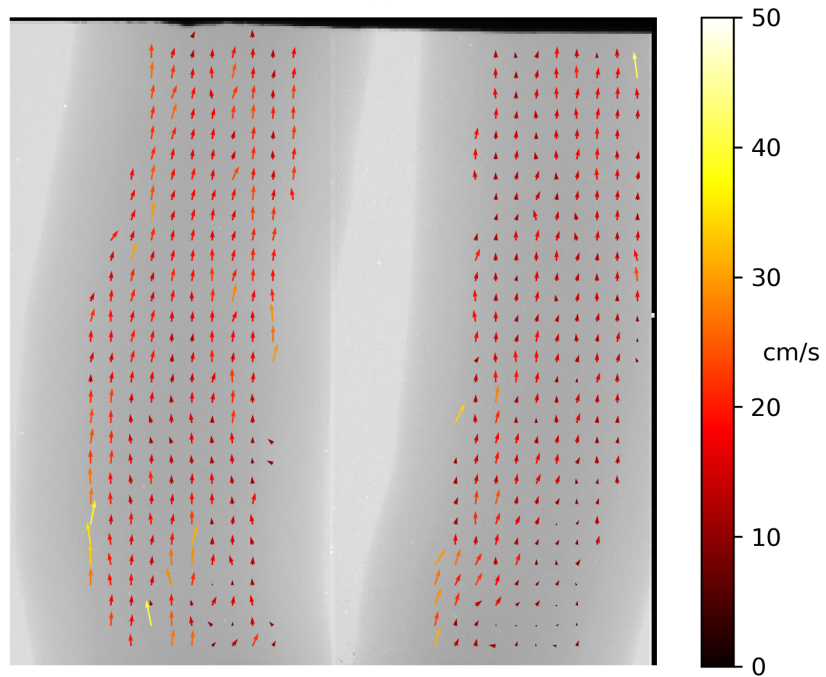
ments tracing dozens of individual particle paths. By averaging the velocity measurements across different regions of interest it was found that the average blood flow velocity in the vessel to the left was 19.2 cm/s and the average velocity in the vessel to the right was 16.3 cm/s with a global average velocity of 17.6 cm/s. In figure 6.4b, the raw velocity data was averaged over space in 8 pixel by 8 pixel regions to remove the noise caused by variation in individual particle paths and to provide a cleaner image for viewing.⁷⁹ This same method of binning to smooth velocity data was applied to all X-PIV measurements and is shown in part b of figures 6.4, 6.7, 6.10, 6.12, and 6.14. A histogram of automated velocity measurements is shown in figure 6.6 and shows velocities measured in the left and right vessels of the carotid vessel over the full image sequence.



Video 6.3: HSA sequence of the bifurcated carotid artery phantom used for manual and automated X-PIV measurements. Video also available at: <https://youtu.be/cieH8w70sMs>.

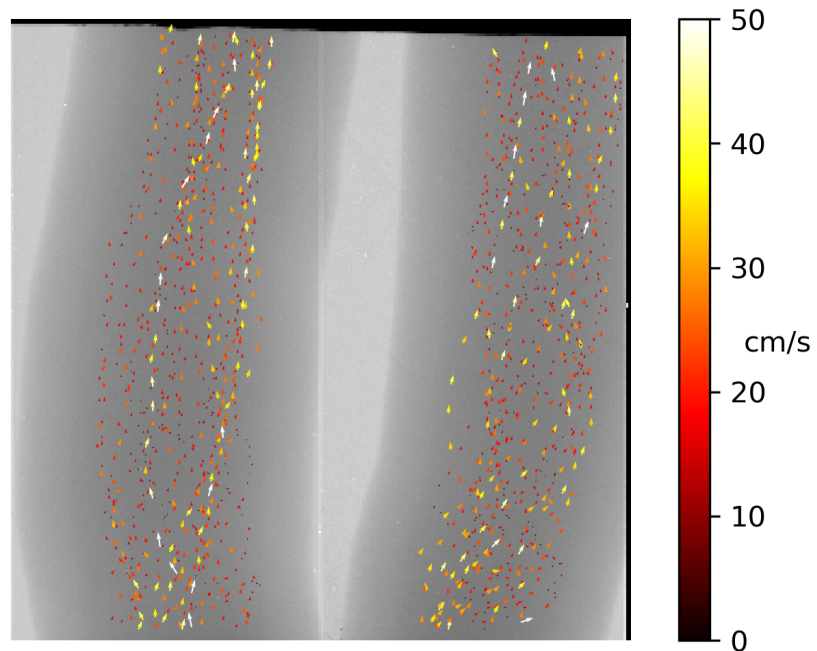


(a)

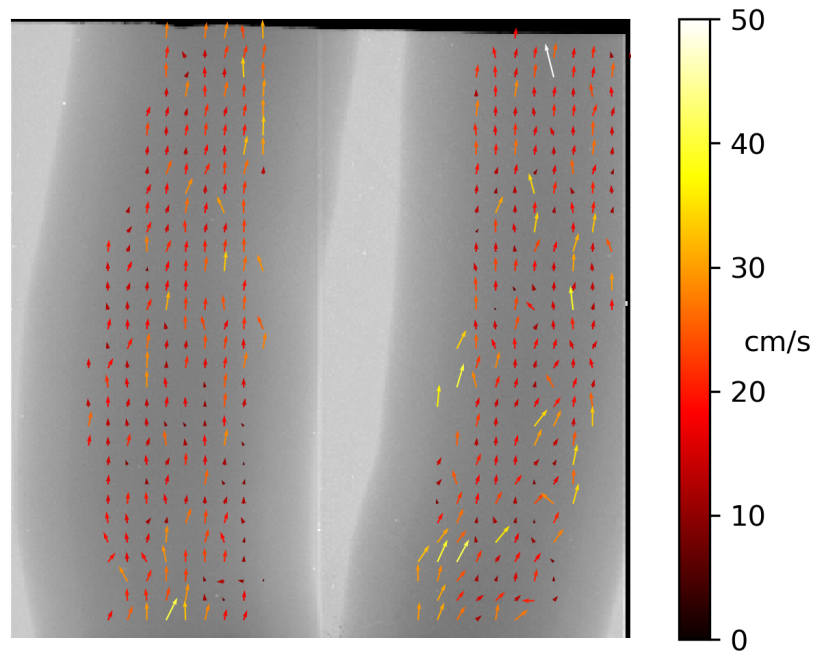


(b)

Figure 6.4: X-PIV measurements in the bifurcated carotid artery phantom made using the automated trackpy software with (a) being the raw velocity data measurements and (b) being the smoothed velocity data.



(a)



(b)

Figure 6.5: X-PIV measurements in the bifurcated carotid artery phantom made using the manual tracking method with (a) being the raw velocity data measurements and (b) being the smoothed velocity data.

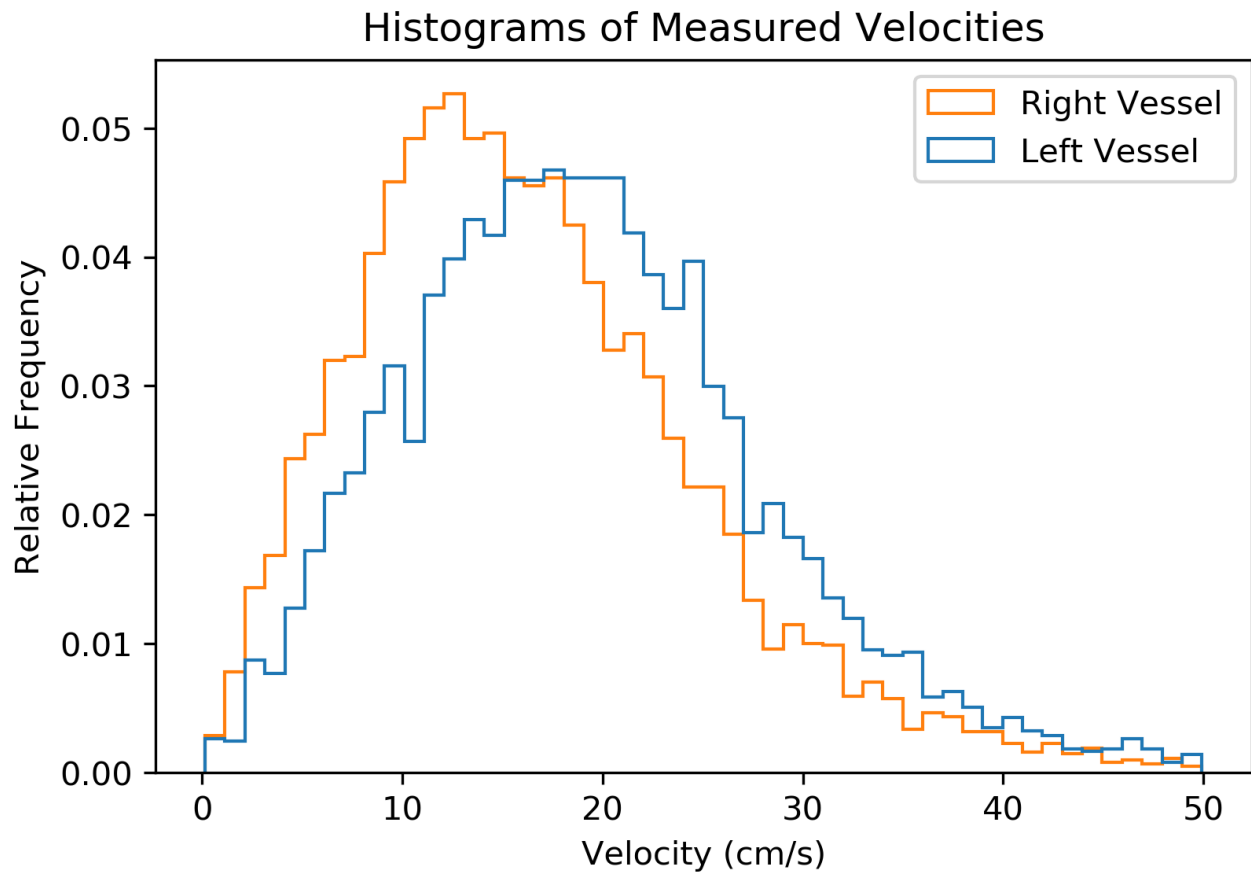
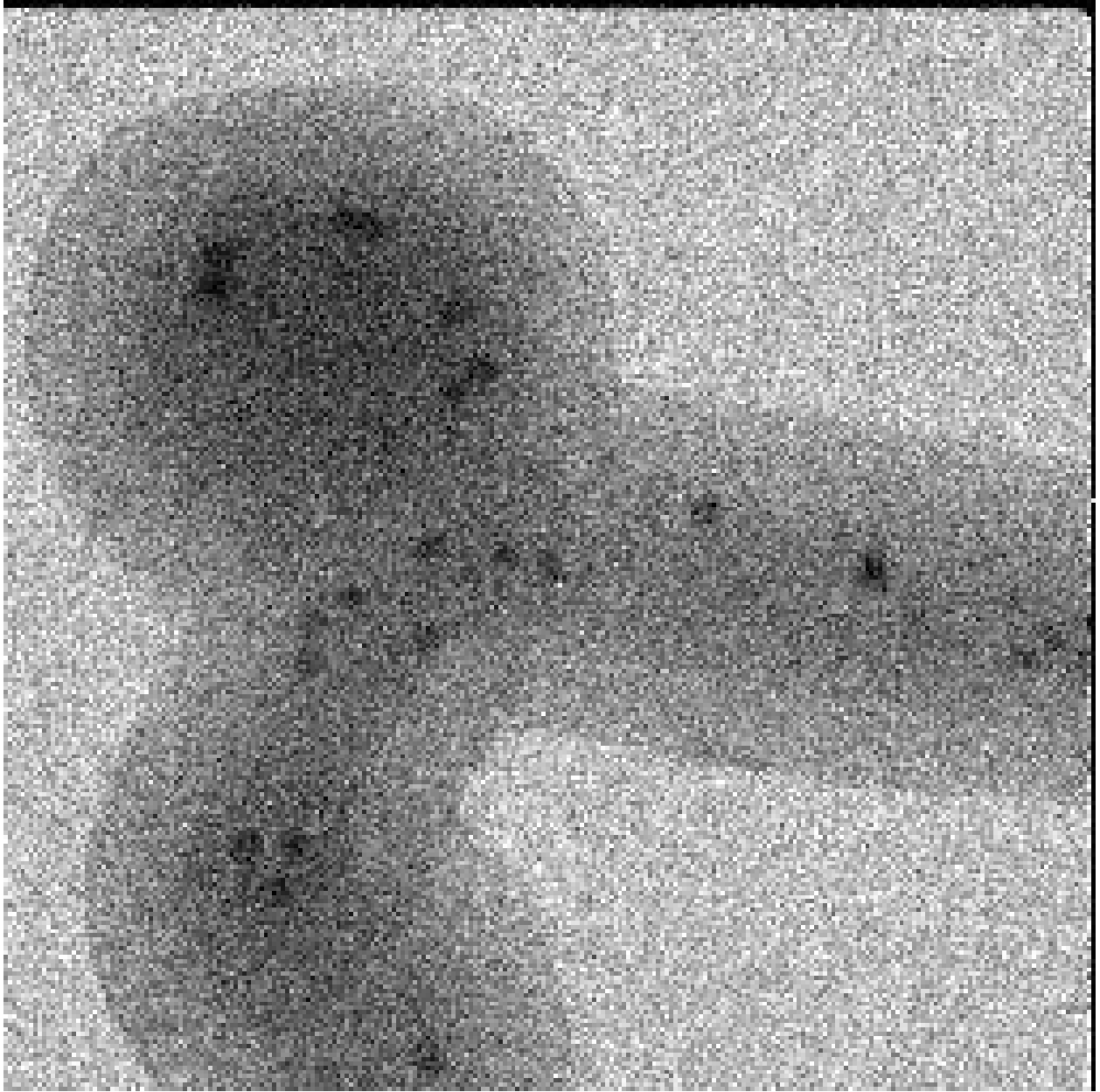
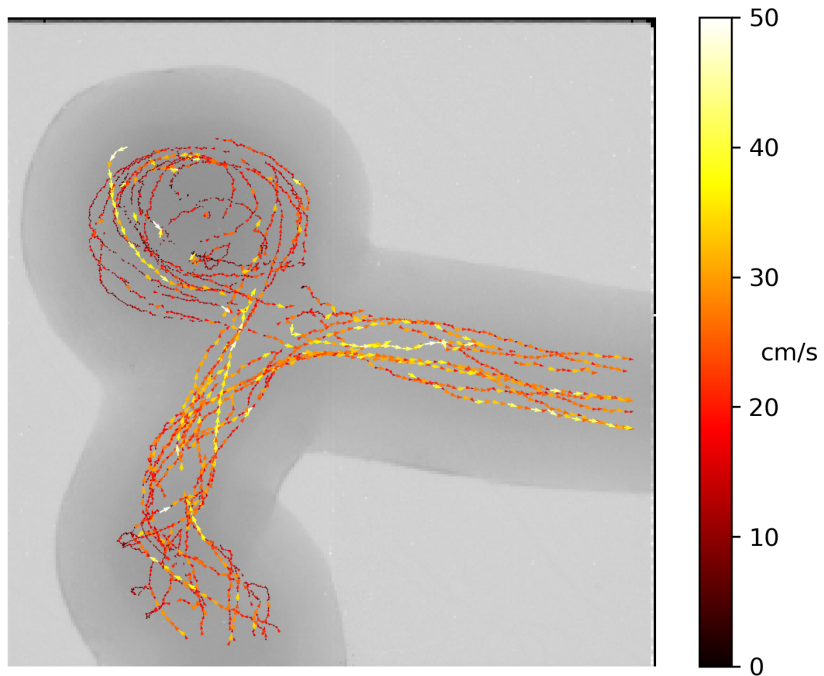


Figure 6.6: Histogram velocities measured in the bifurcated carotid artery phantom.

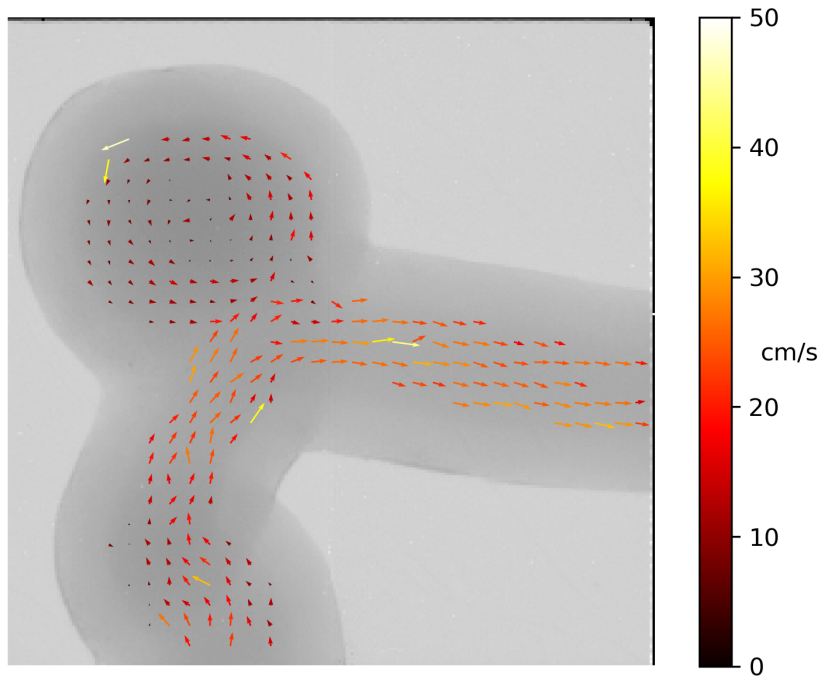
Figure 6.7 shows the automated measurements of flow in the internal carotid artery with an idealized saccular aneurysm phantom (see figure 5.4B). Figure 6.9 shows a histogram of automatically measured velocities for regions confined to the inflow vessel, outflow vessel, and aneurysm sac. Using the X-PIV method the average blood flow velocity in the inflow vessel was found to be 19.2 cm/s with an average velocity of 25.8 cm/s, an increase caused by a narrowing of the vessel. However, within the aneurysm sac the velocity was found to be much lower with an average blood flow velocity of 13.6 cm/s. Also, of note is the formation of what appears to be a vortex pattern within the aneurysm sac, which generates stress on the walls of the aneurysm.⁷⁹



Video 6.4: HSA sequence of the internal carotid artery with idealized saccular aneurysm phantom used for manual and automated X-PIV measurements. Video also available at: <https://youtu.be/JwsmM-cEYHk>.

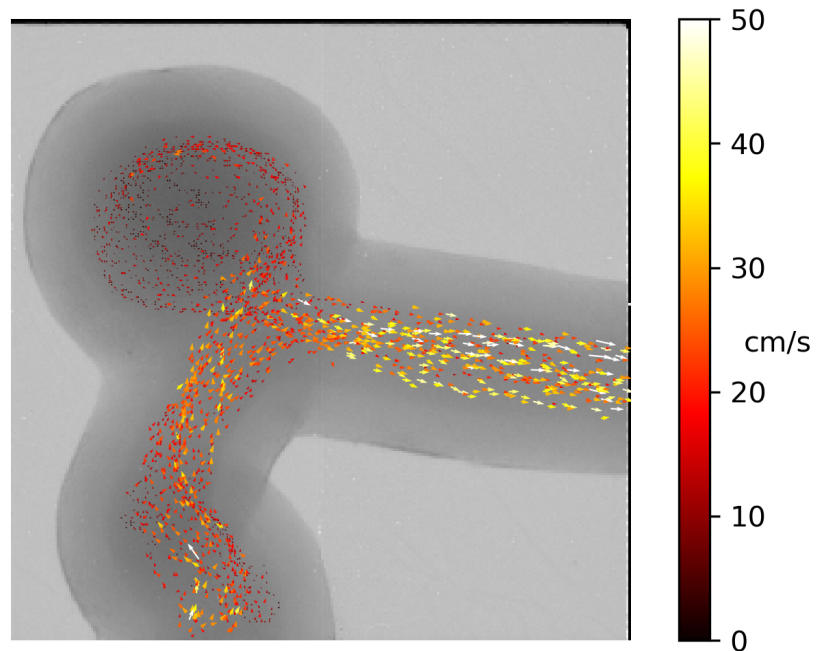


(a)

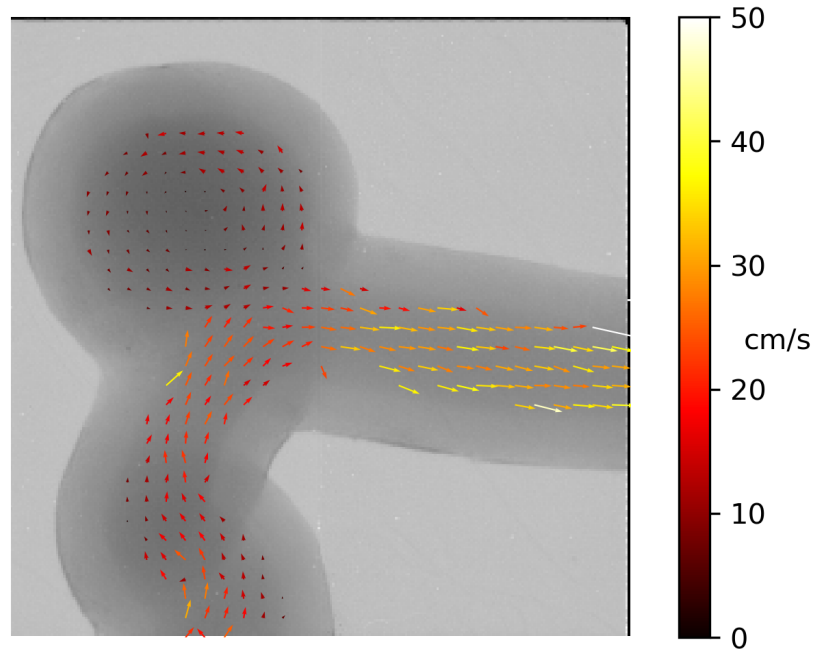


(b)

Figure 6.7: X-PIV measurements in the internal carotid artery with idealized saccular aneurysm phantom made using the automated trackpy software with (a) being the raw velocity data measurements and (b) being the smoothed velocity data.



(a)



(b)

Figure 6.8: X-PIV measurements in the internal carotid artery with idealized saccular aneurysm phantom made using the manual tracking method with (a) being the raw velocity data measurements and (b) being the smoothed velocity data.

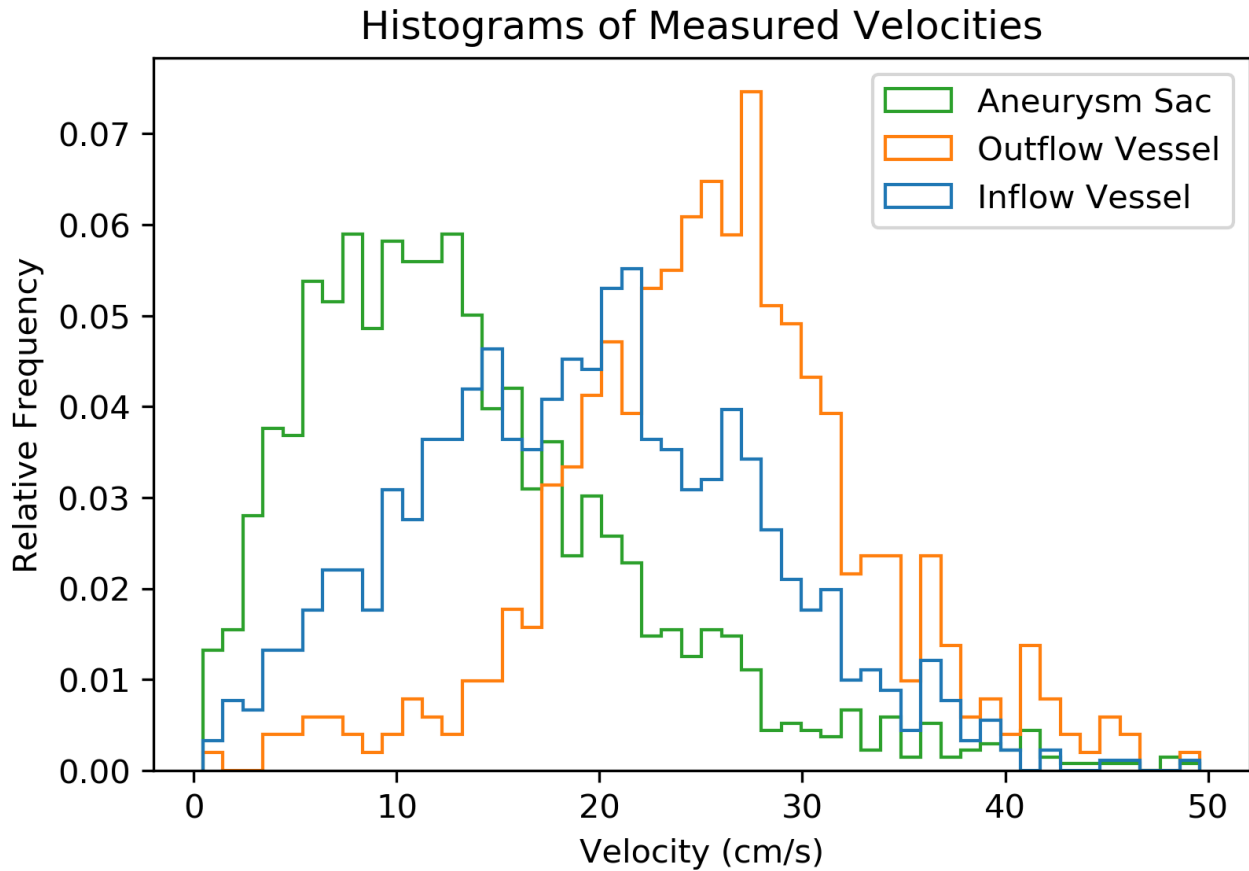
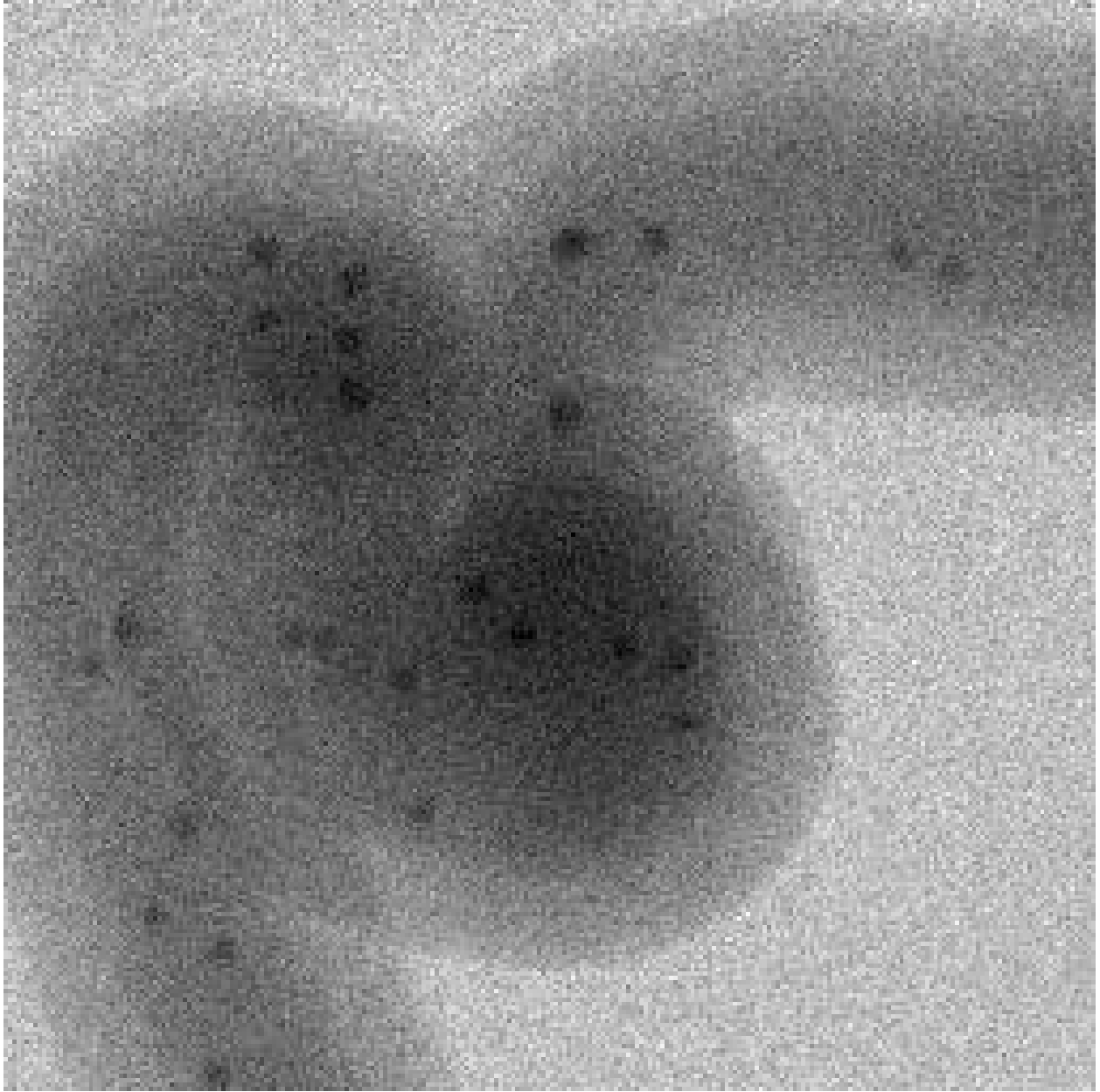
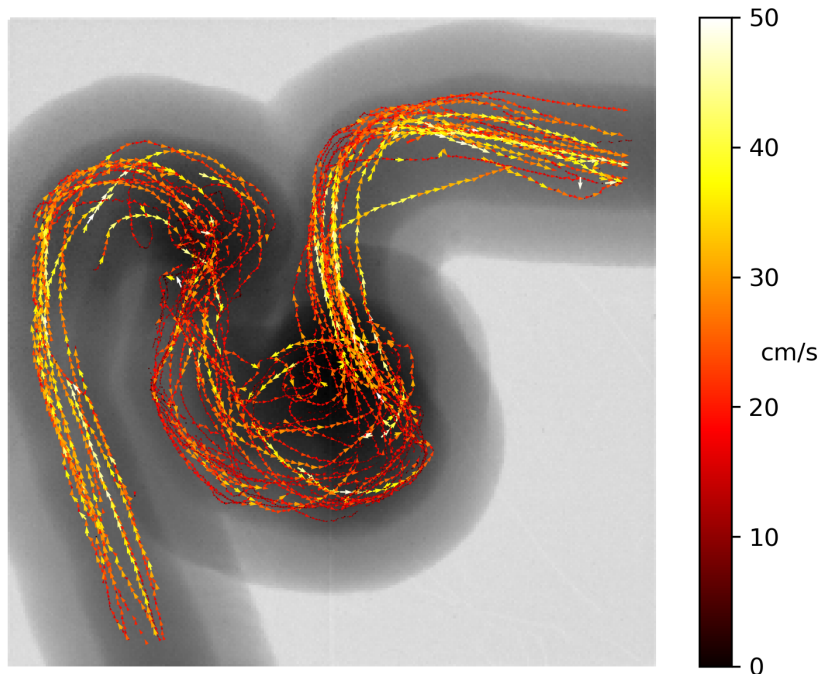


Figure 6.9: Histogram velocities measured in the internal carotid artery with idealized saccular aneurysm phantom.

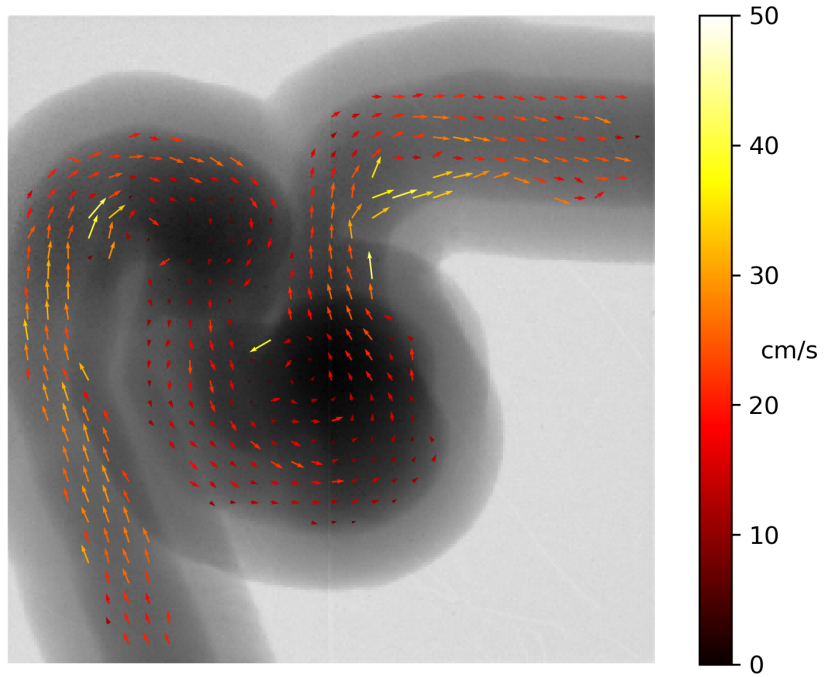
Figure 6.10 shows the automated measurements of flow in the internal carotid artery with a wide necked saccular aneurysm phantom. Figure 6.11 shows a histogram of the automated flow measurements in the inflow vessel, outflow vessel and aneurysm sac. Average blood flow velocity was found to be 21.6 cm/s across the inflow vessel, but drops sharply to 14.8 cm/s as flow moves through the first bend of vessel. After passing through the second bend and entering the region of the aneurysm sac blood flow was measured to be 16.3 cm/s on average. Finally, flow exiting through the outflow rose again to 22.4 cm/s on average. The aneurysm is difficult to see from the angle used for imaging, but the flow velocity measurements and particle tracks clearly show the formation of a vortex in the location of the aneurysm sac.⁷⁹



Video 6.5: HSA sequence of the internal carotid artery with wide-necked saccular aneurysm phantom used for manual and automated X-PIV measurements. Video also available at: <https://youtu.be/IrnfxnoxRT4>.



(a)



(b)

Figure 6.10: X-PIV measurements in the internal carotid artery with wide-necked saccular aneurysm phantom made using the automated trackpy software with (a) being the raw velocity data measurements and (b) being the smoothed velocity data.

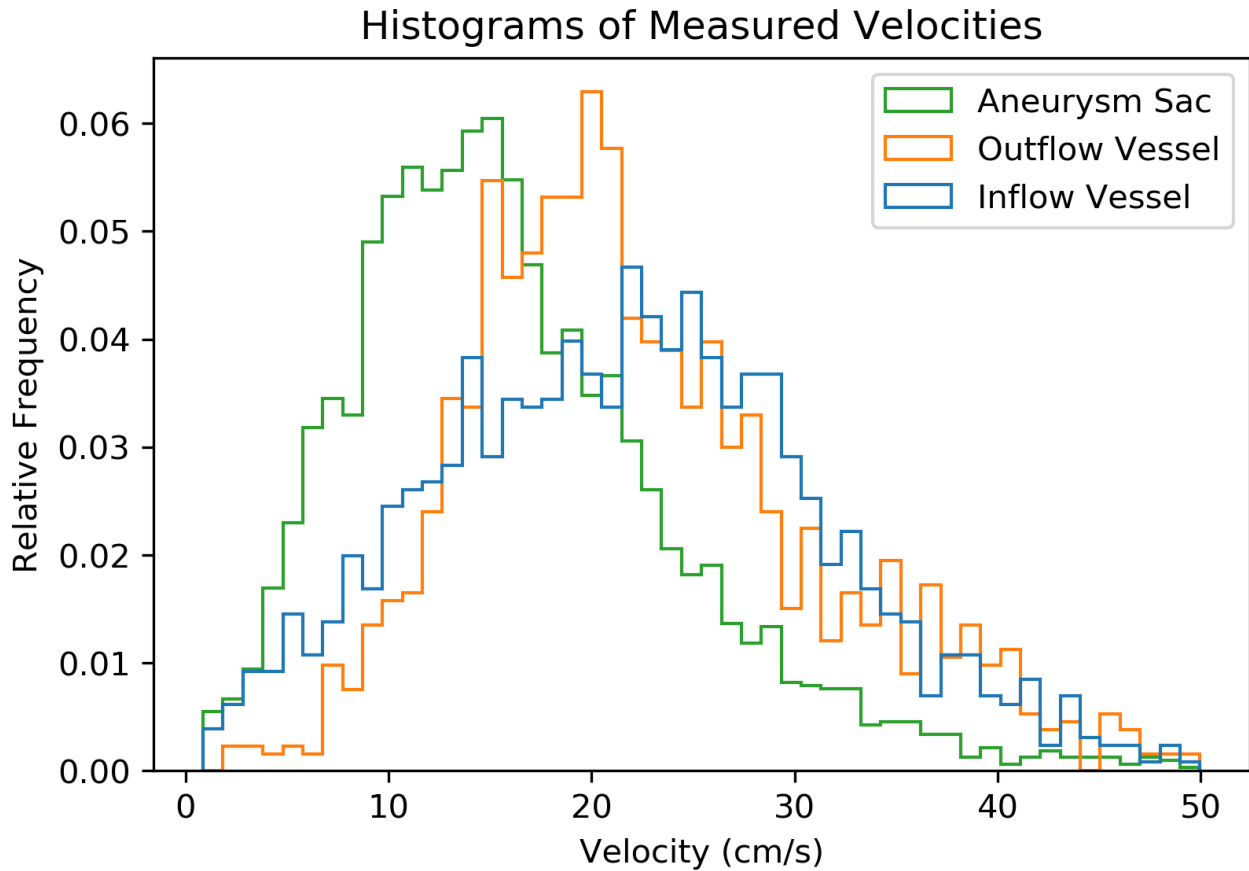
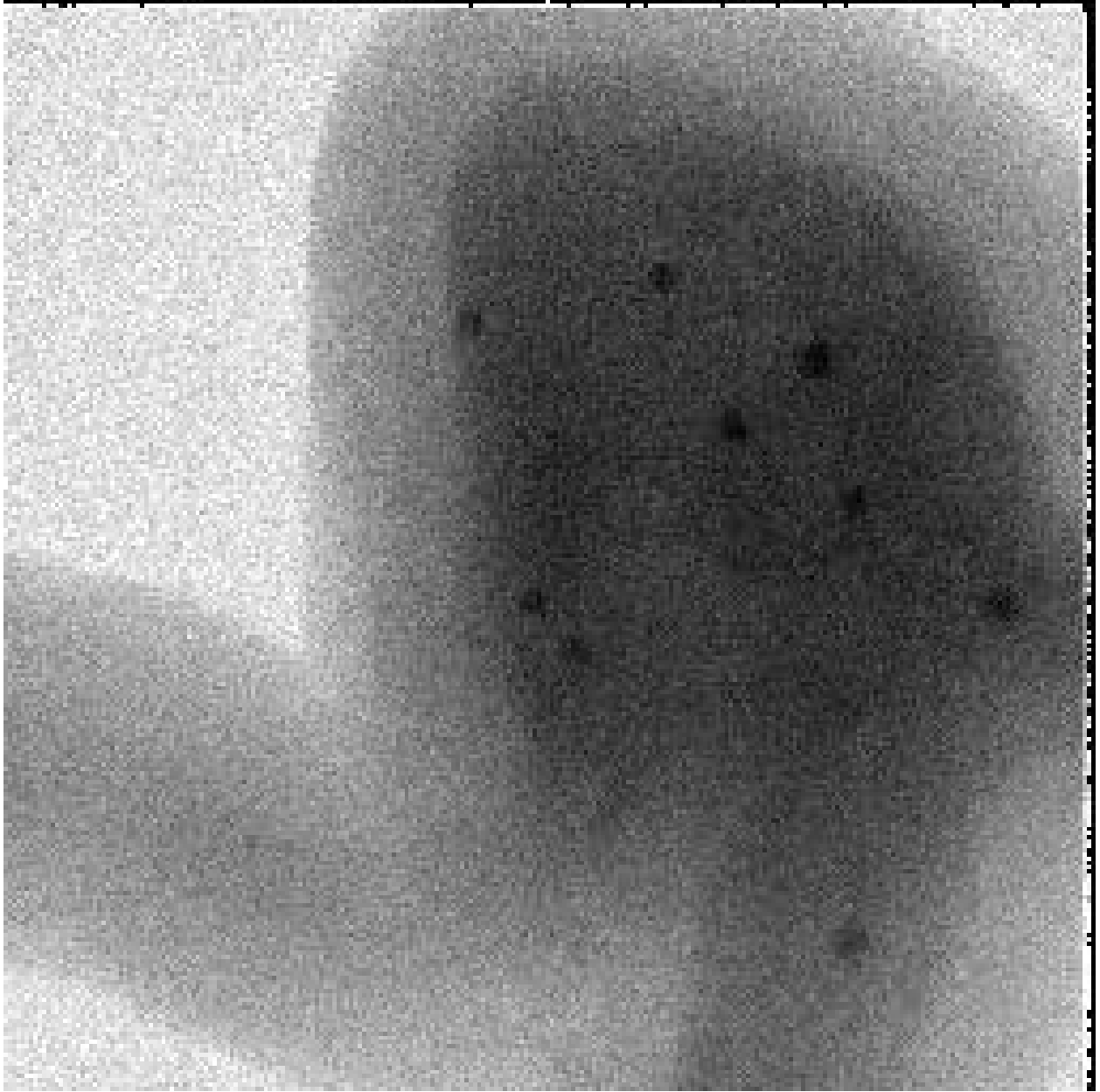
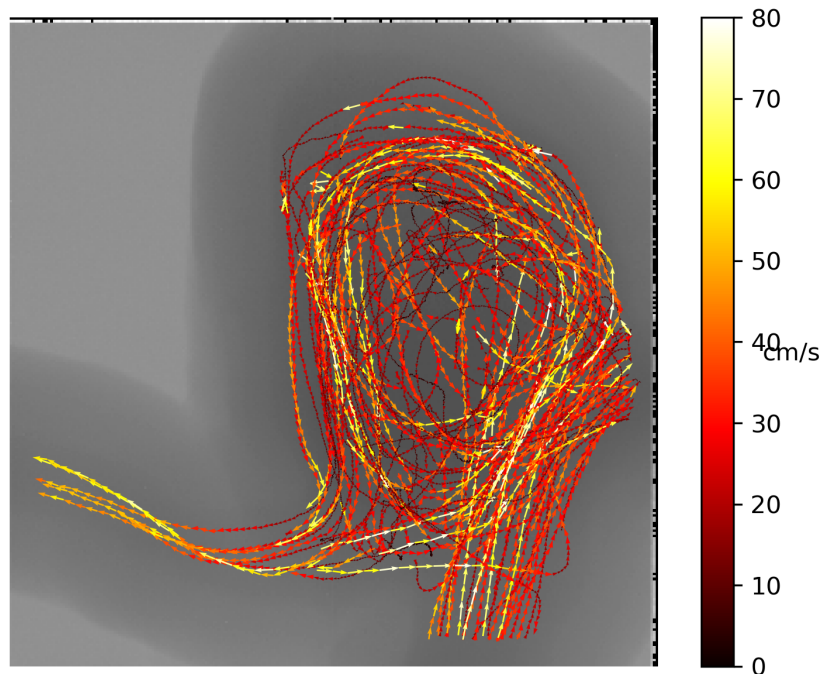


Figure 6.11: Histogram velocities measured in the internal carotid artery with wide-necked saccular aneurysm phantom.

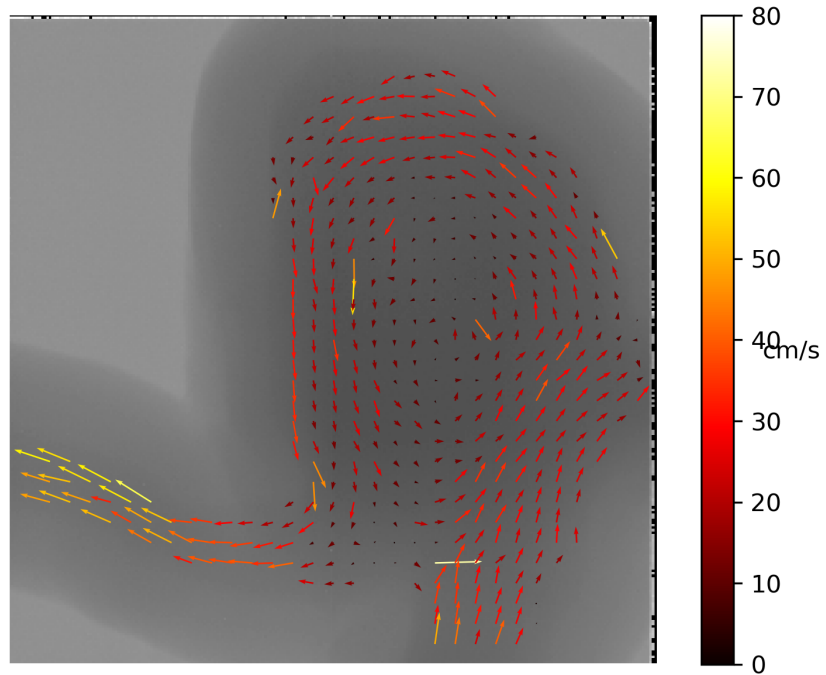
Figure 6.12 shows the automated measurements of flow in the basilar apex saccular aneurysm phantom. Figure 6.13 shows a histogram of automated velocity measurements in regions covering the inflow vessel, left outflow vessel, and aneurysm sac. Average blood flow velocity in the inflow vessel was found to be 30.4 cm/s, with the left and right branches of the bifurcated basilar having measured flow velocities of 39.4 cm/s and 22.0 cm/s respectively. Within the aneurysm sac, average velocities were measured at 21.7 cm/s. Particle tracks indicate a bias towards the vessel on the right of the image, with some backflow indicated in the raw velocity measurements. The vessel on the left was also far narrower and resulted in much higher velocity measurements than in the vessel on the right as can clearly be seen in the binned velocity image.⁷⁹



Video 6.6: HSA sequence of the basilar apex saccular aneurysm phantom used for manual and automated X-PIV measurements. Video also available at: <https://youtu.be/Kk4qxSdJXnE>.



(a)



(b)

Figure 6.12: X-PIV measurements in the basilar apex saccular aneurysm phantom made using the automated trackpy software with (a) being the raw velocity data measurements and (b) being the smoothed velocity data.

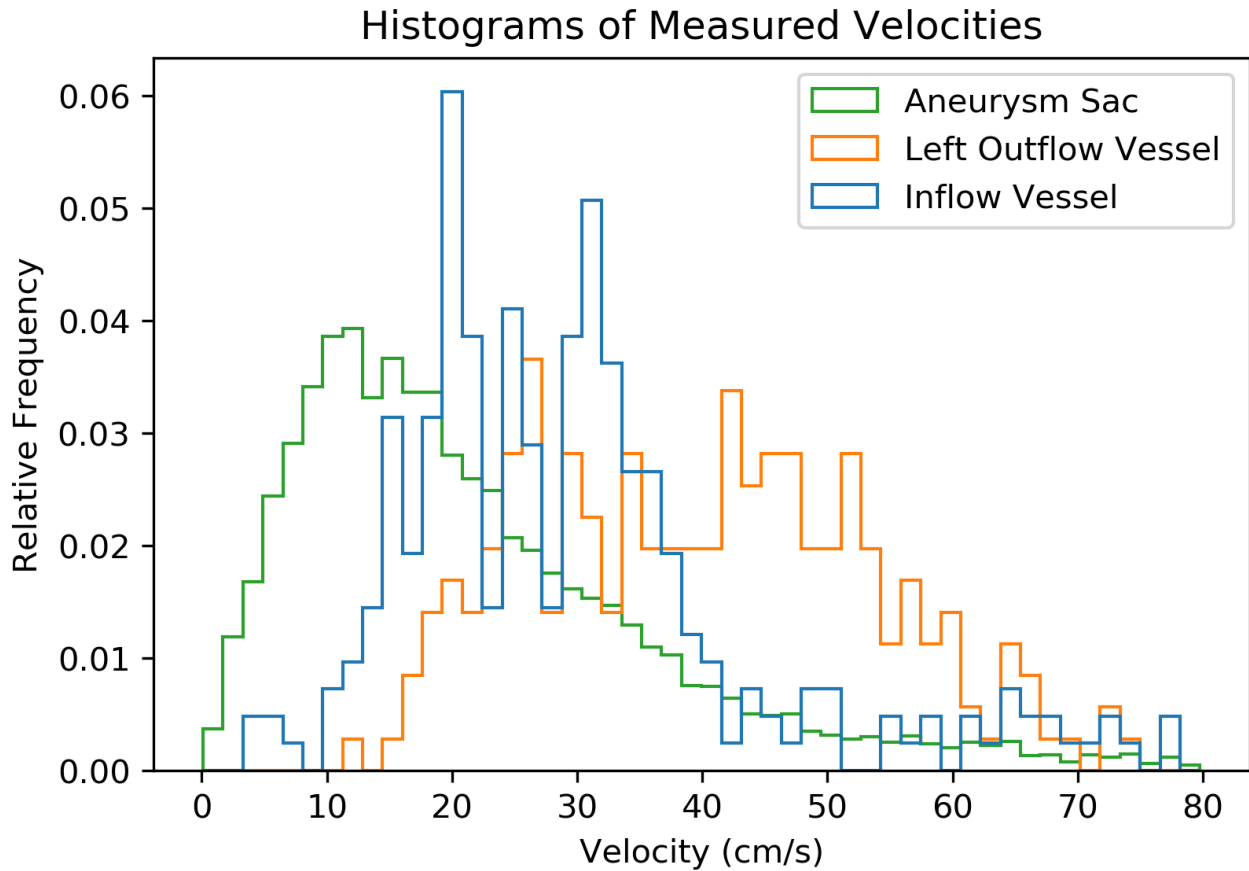
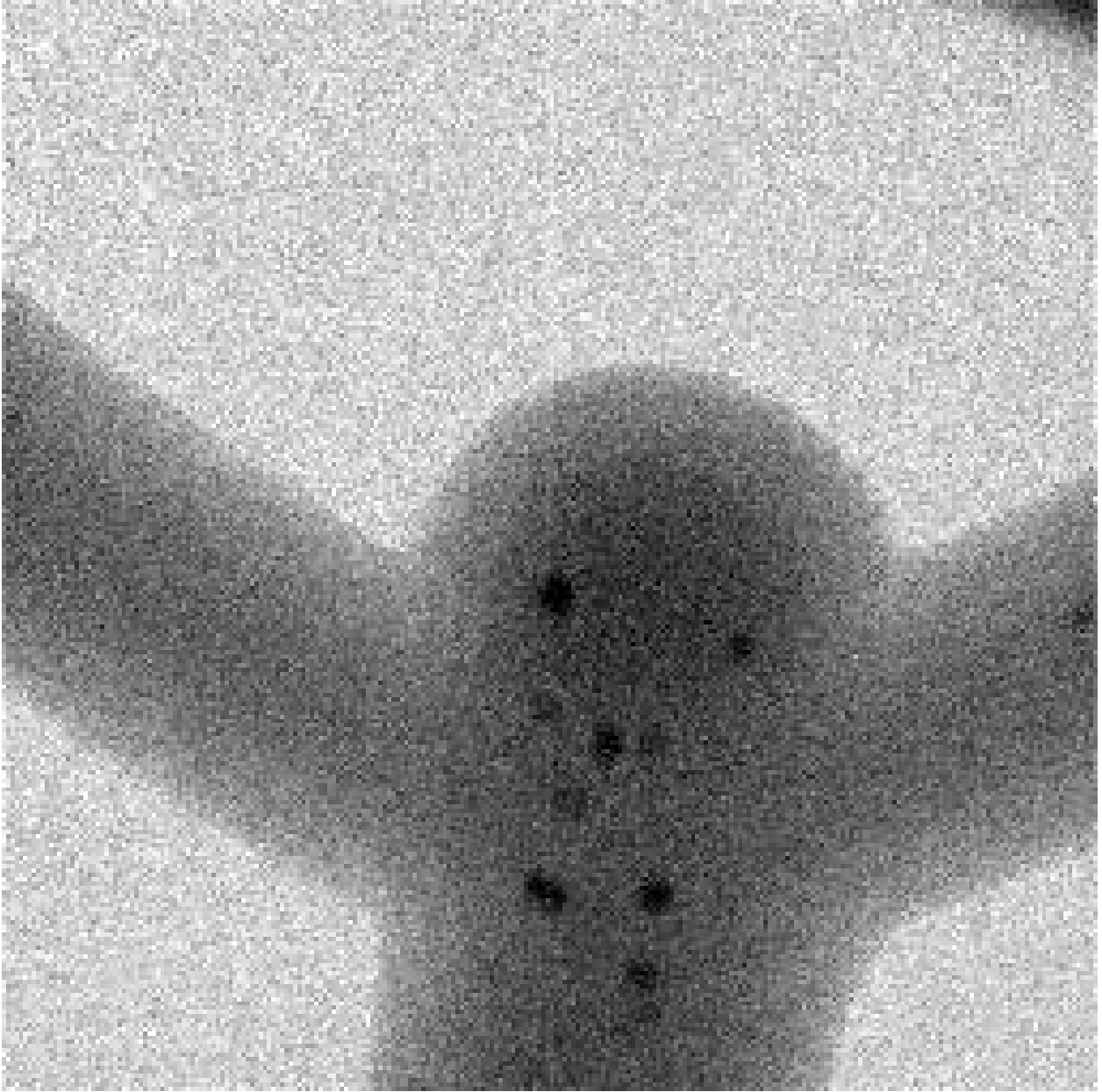
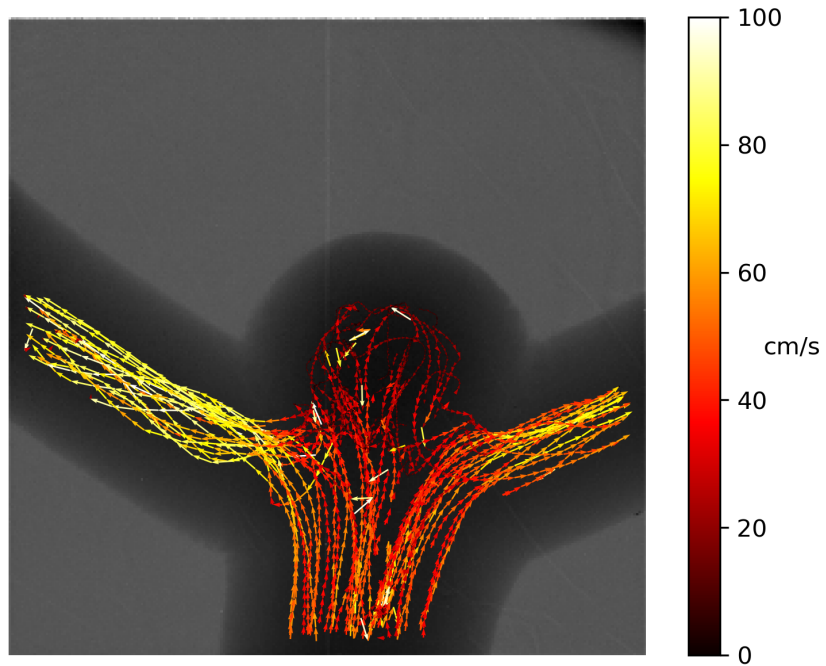


Figure 6.13: Histogram velocities measured in the basilar apex saccular aneurysm phantom.

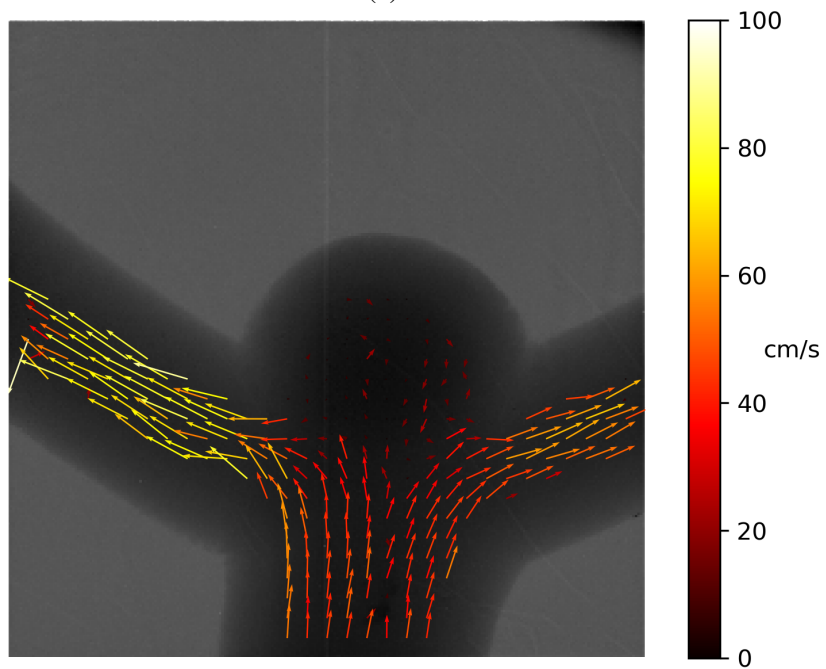
Figure 6.14 shows the automated measurements of flow in the idealized basilar apex saccular aneurysm phantom. Figure 6.15 shows a histogram of velocity measurements in regions covering the inflow vessel, left outflow vessel, and aneurysm sac. Average blood flow velocity in the inflow vessel was found to be 32.9 cm/s before slowing to 21.4 cm/s in the aneurysm sac. Flow leaving the phantom through the left and right branches of the bifurcated basilar artery had a measured average blood flow velocity of 70.9 cm/s and 56.1 cm/s respectively. Flow in the aneurysm sac is extremely erratic, this is believed to be due to the idealized nature of the phantoms as opposed to aneurysms that form naturally due to perturbed flow.⁷⁹



Video 6.7: HSA sequence of the idealized basilar apex saccular aneurysm phantom used for manual and automated X-PIV measurements. Video also available at: <https://youtu.be/rkmWNf0tCbc>.



(a)



(b)

Figure 6.14: X-PIV measurements in the idealized basilar apex saccular aneurysm phantom made using the automated trackpy software with (a) being the raw velocity data measurements and (b) being the smoothed velocity data.

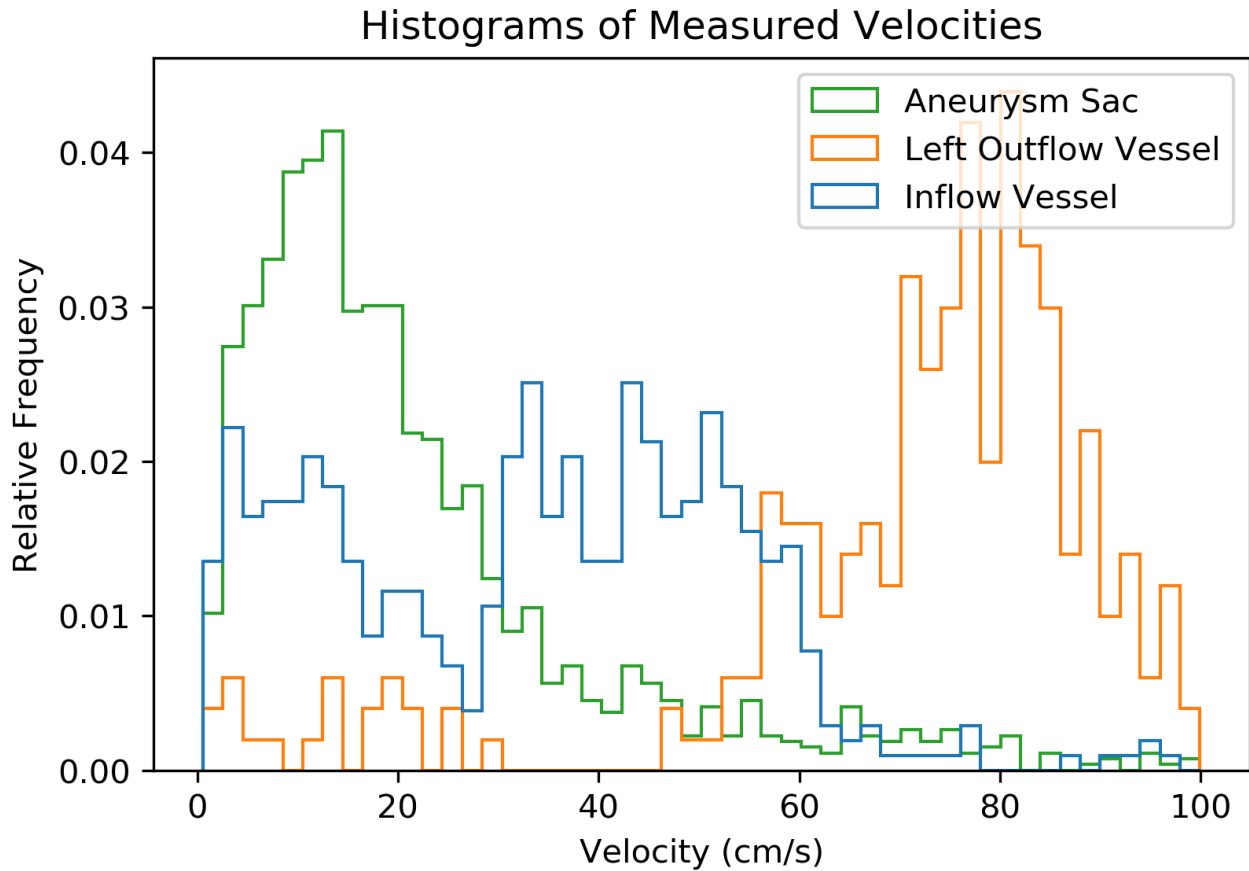


Figure 6.15: Histogram velocities measured in the idealized basilar apex saccular aneurysm phantom.

Figures 6.5a, 6.5b, 6.8a, and 6.8b show velocity measurements acquired manually as a method to verify the automated flow measurements of figures 6.4a, 6.4b, 6.7a, and 6.7b respectively. These figures display several hundred velocity measurements for each model, tracking dozens of individual particles, and covering the full vessel geometry. A side-by-side comparison of the manually measured flow velocity and the automated flow velocity maps show that the overall shape of flow appears consistent between the two methods. The average measured velocity in figure 6.5 was found to be 19.4 cm/s, which is 9.7% greater than the 17.6 cm/s average flow velocity measured with the automated method, likely due to far fewer measurements being made with the manual method. The average measured velocity across all space shown in figure 6.8 was found to be 17.8 cm/s, which has a difference of just 1.13%, compared to the automated average velocity measurement of 17.6 cm/s. A further comparison of the two methods is shown in the histograms comparing

measured velocities for the bifurcated carotid artery phantom and internal carotid artery with idealized saccular aneurysm phantom in figures 6.16 and 6.17 respectively, which show great similarity in velocity measurements between both manual and automated methods.⁷⁹

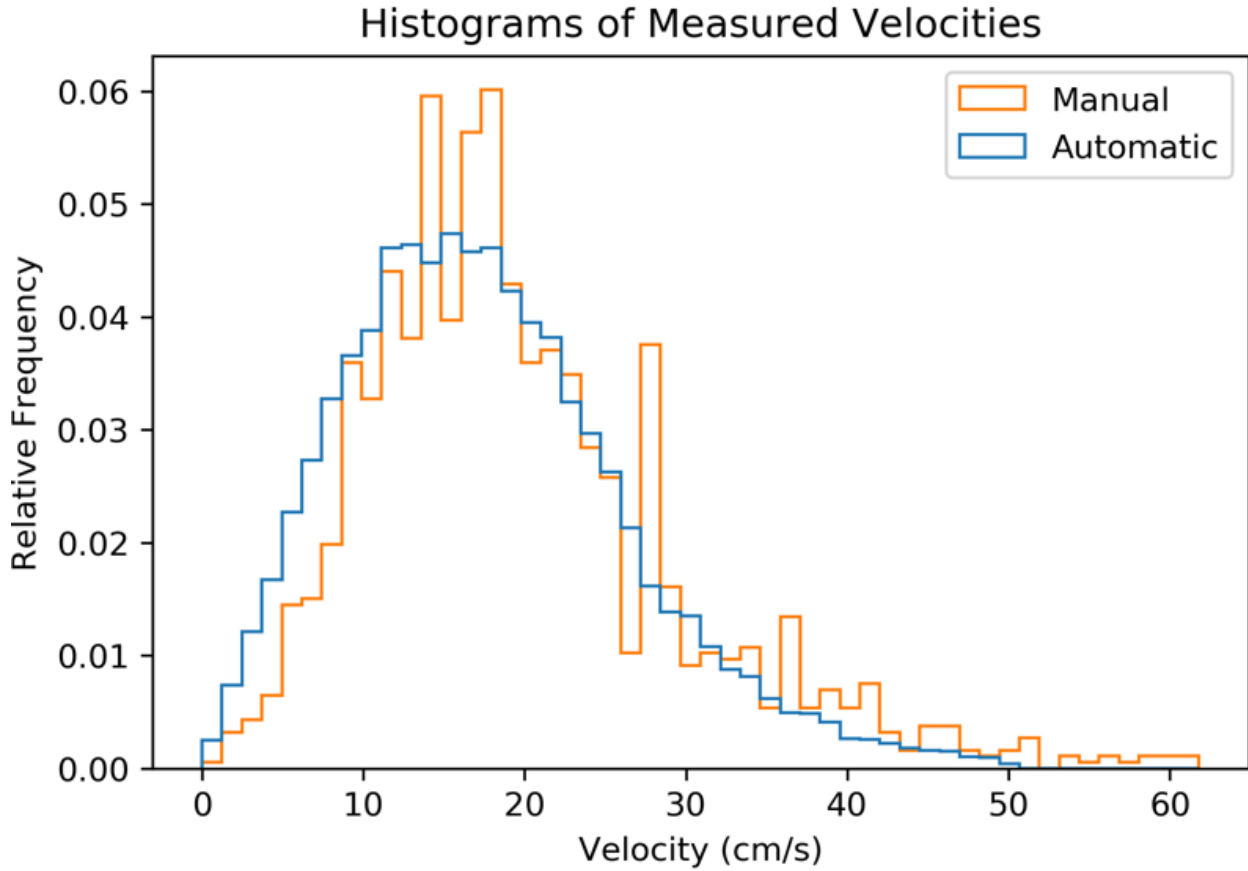


Figure 6.16: Histogram comparing manual and automated X-PIV measurements for the bifurcated carotid artery phantom.

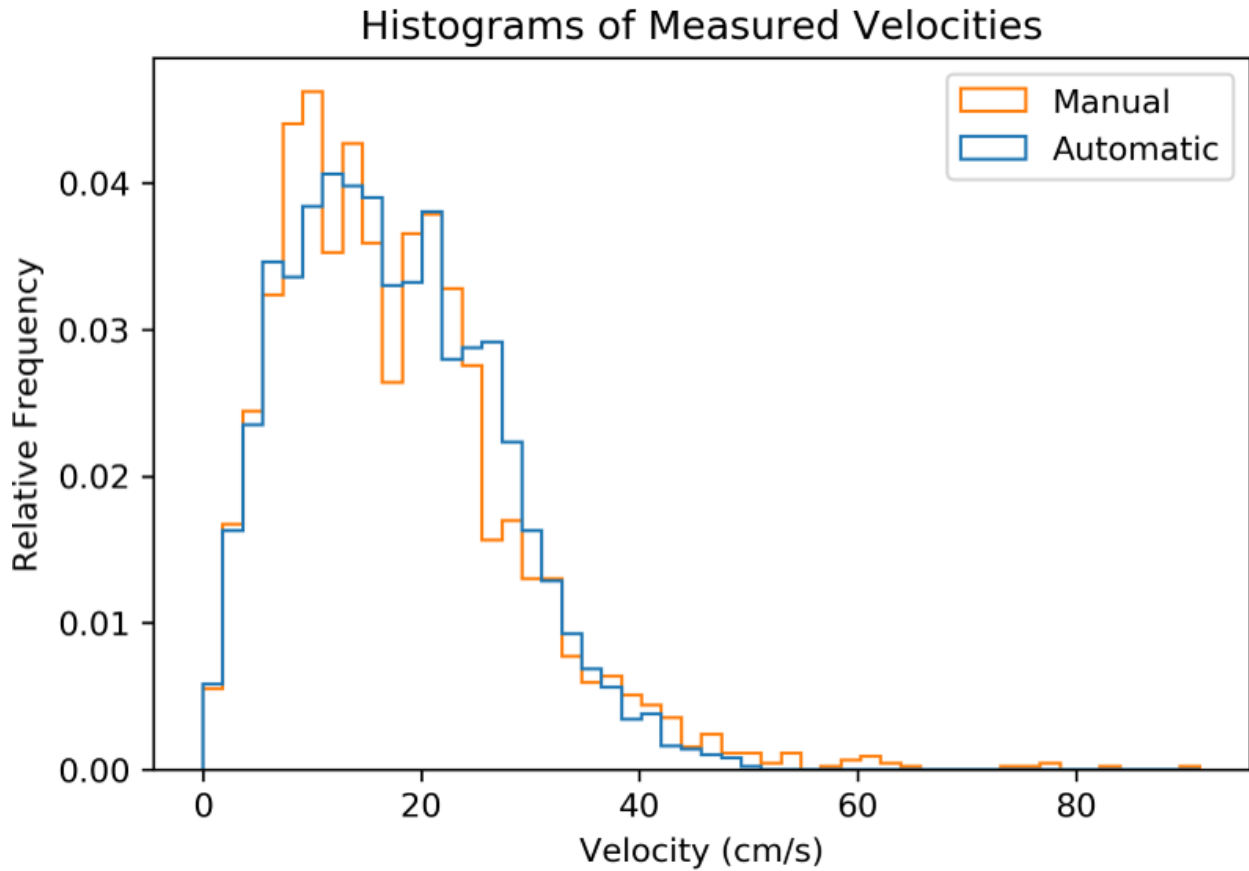


Figure 6.17: Histogram comparing manual and automated X-PIV measurements for the internal carotid artery with idealized saccular aneurysm phantom.

6.3.3 Impact of Frame Rates on X-PIV

Figures 6.18 and 6.19 show the raw and averaged velocity measurements made using X-PIV for the simulated frame rates and can be compared to the 1000 fps velocity maps in figure 6.10. From the figures it can be seen that the number of velocity measurements quickly begins to drop off going from 7684 velocity measurements for the 1000 fps image sequence, to 4205 for the 500 fps image sequence, to 2735 for the 333 fps image sequence, to 2041 for the 250 fps image sequence, to just 1259 for the 200 fps image sequence. This is due in part to fewer frames, but is also evident in the lack of velocity measurements in regions of higher flow velocity, such as the in-flow vessel. These higher velocities with low frame rates cause a blurring of particles, making them more difficult to detect.

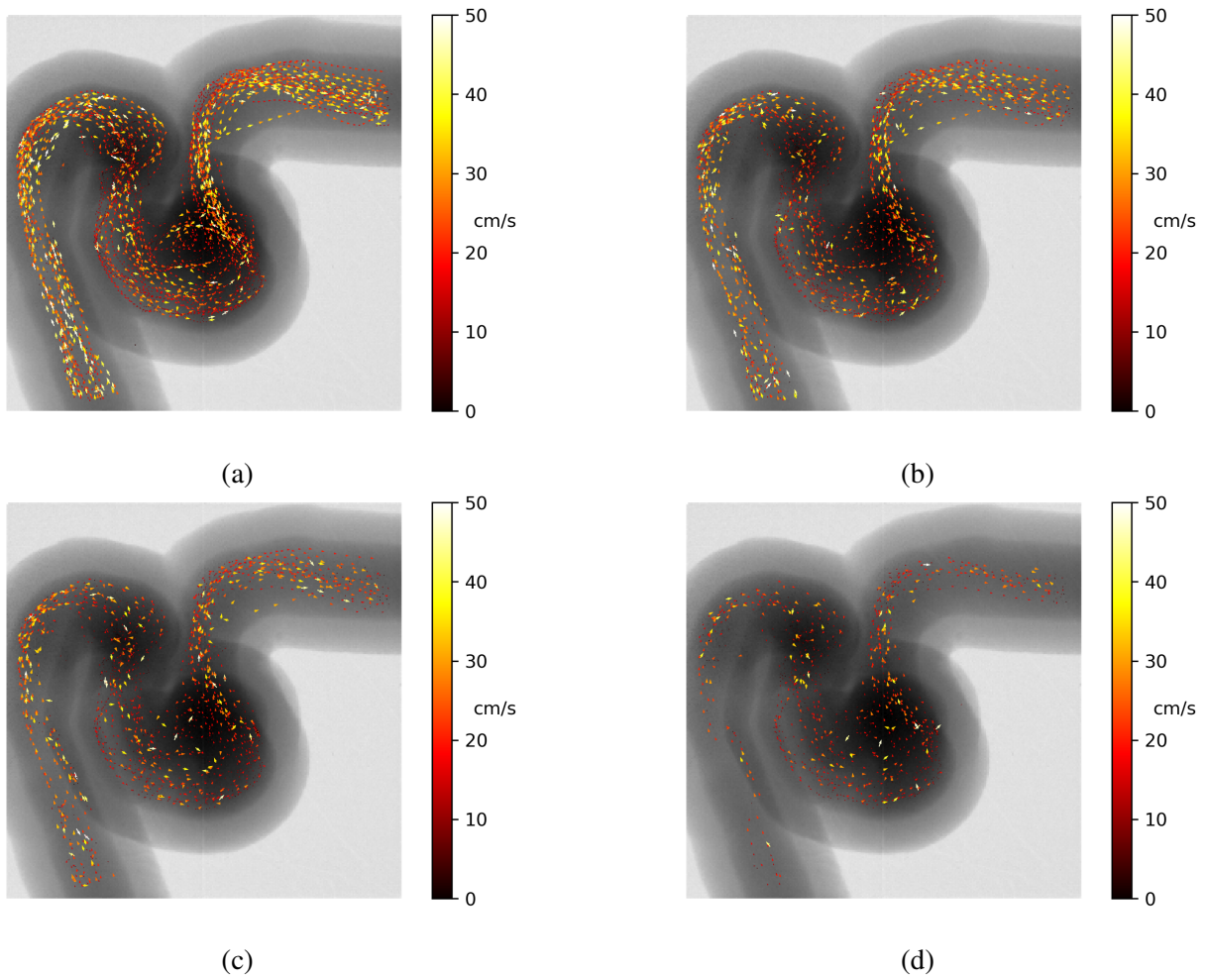


Figure 6.18: X-PIV measurements in the internal carotid artery with wide-necked saccular aneurysm phantom made using the automated trackpy software for (a) 500, (b) 333, (c) 250, and (d) 200 fps image sequences.

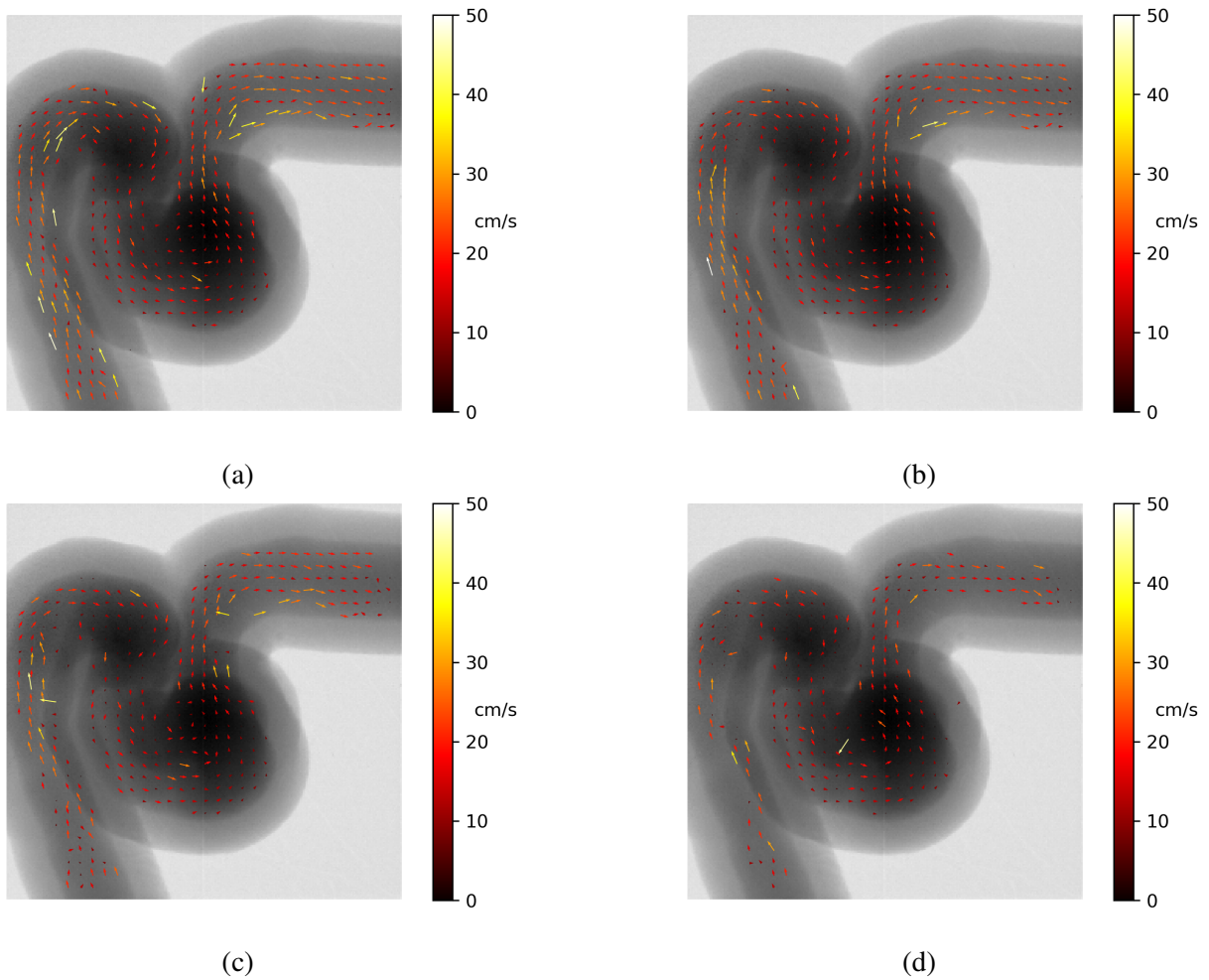


Figure 6.19: Averaged X-PIV measurements in the internal carotid artery with wide-necked sacular aneurysm phantom made using the automated trackpy software for (a) 500, (b) 333, (c) 250, and (d) 200 fps image sequences.

Furthermore, the average measured velocity changes as frame rate changes as well. For the 1000 fps image sequence the average velocity for all time and space was 20.3 cm/s, but as the frame rate was dropped that changed to 19.2 cm/s for 500 fps, 17.9 cm/s for 333 fps, 16.8 cm/s for 250 fps, and finally 14.7 cm/s for 200 fps. This effect is due primarily to a lack of higher velocity measurements as can be seen from figures 6.20 through 6.23 in which histograms the relative frequency of measured velocities for simulated frame rates are compared to the ground truth. As can be seen from the figures, the average velocity gradually shifts towards the lower end as fewer high speed velocities are measured due to blurred particles becoming less visible.

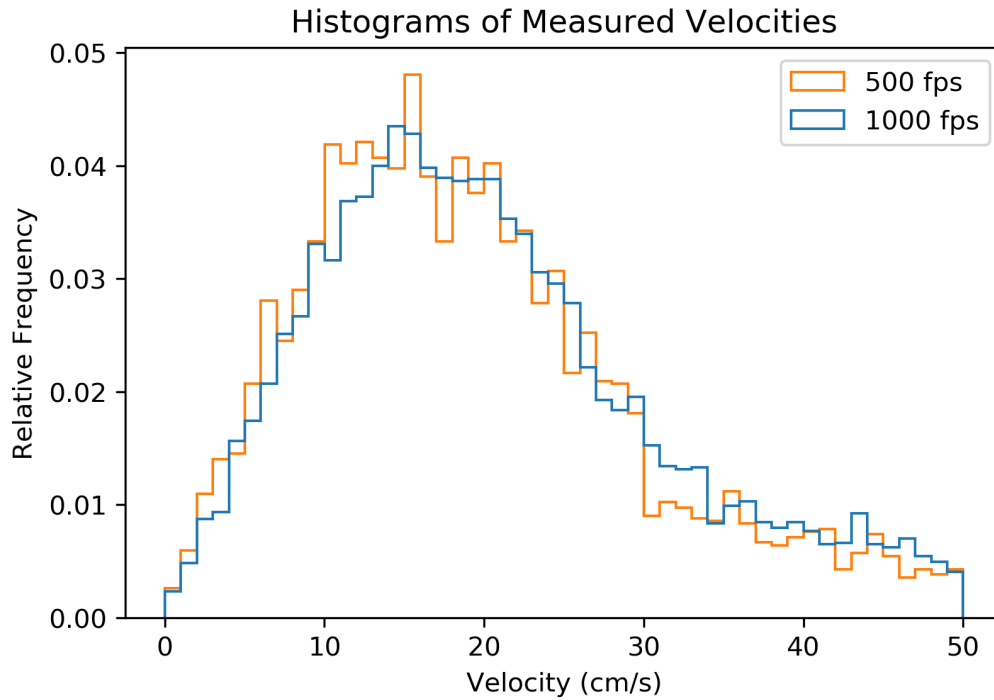


Figure 6.20: Histogram comparing the relative frequency of measured velocities for simulated 500 fps are compared to the ground truth. Both measurements were made via trackpy X-PIV.

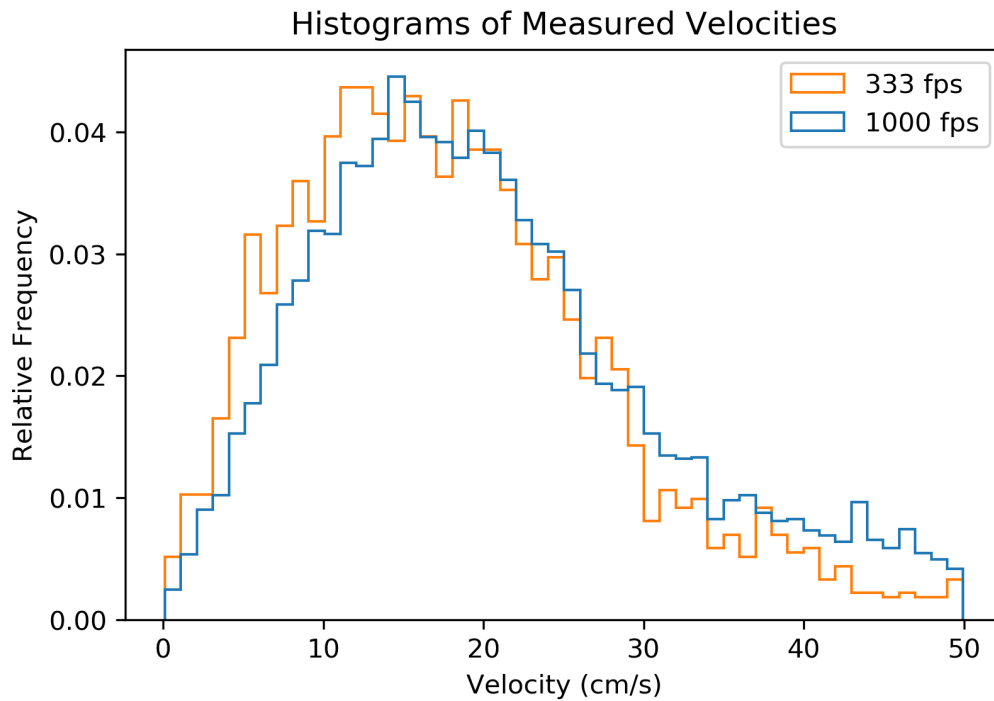


Figure 6.21: Histogram comparing the relative frequency of measured velocities for simulated 333 fps are compared to the ground truth. Both measurements were made via trackpy X-PIV.

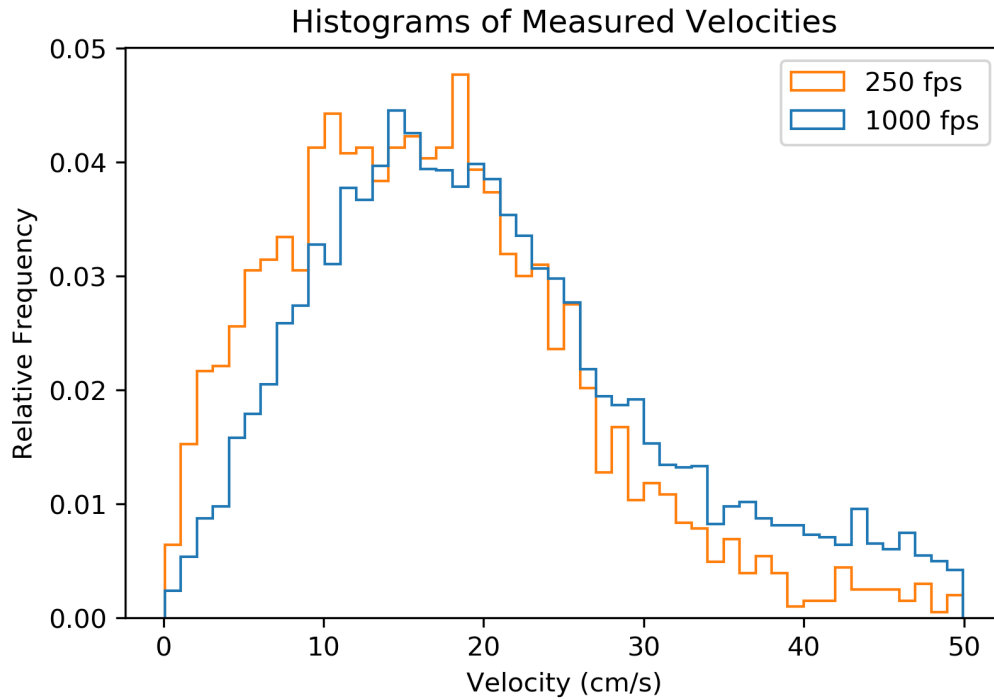


Figure 6.22: Histogram comparing the relative frequency of measured velocities for simulated 250 fps are compared to the ground truth. Both measurements were made via trackpy X-PIV.

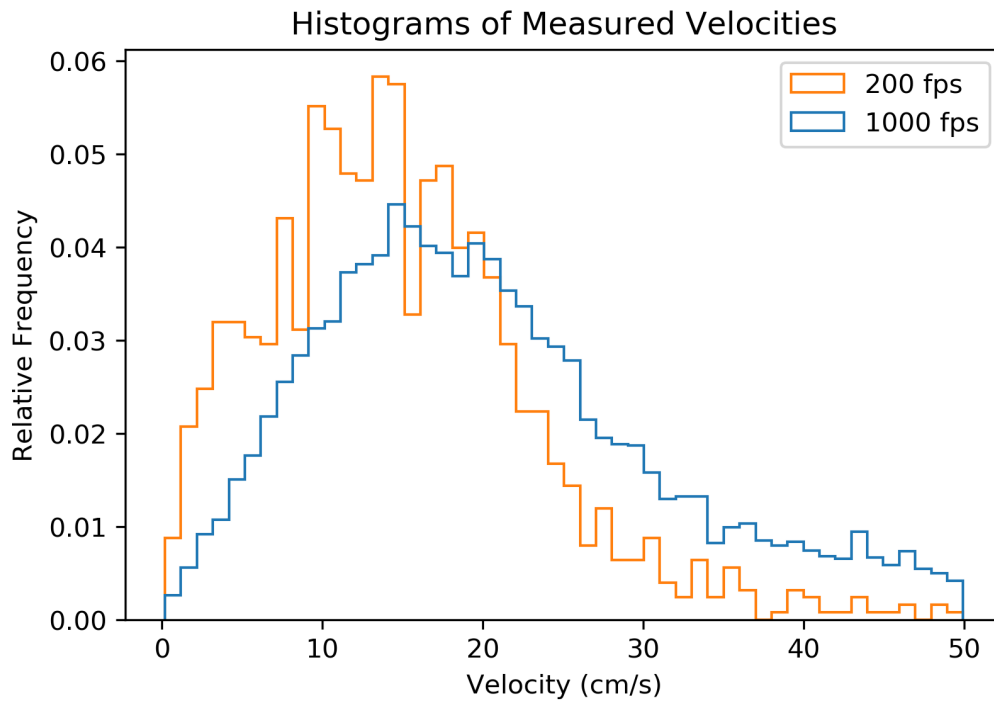


Figure 6.23: Histogram comparing the relative frequency of measured velocities for simulated 200 fps are compared to the ground truth. Both measurements were made via trackpy X-PIV.

6.4 Discussion

The methods described in this chapter have enabled the experimental measurement of flow data in patient-specific models due to the use of HSA. Though manual methods are crude, they do provide real-world measurements that could improve our understanding of how vascular pathologies impact blood flow velocities. Measurements from injected iodine contrast demonstrate great promise since it is already approved for use in patients, however methods still need to be developed to examine flow from iodine contrast. The velocity maps generated using the two X-PIV methods described above demonstrate the capacity for HSA to be used in quantifying blood flow patterns. While the two methods demonstrated reasonable agreement, there are some caveats to using both methods.

For the manual tracking method, the user estimates the center of the particles with a mouse pointer, which introduces some slight errors. However, since each particle is only 900 μm across, these errors are small and averaging across many measurements should minimize their impact on the velocity maps. In addition, since movement between individual frames is slight, the user may have to progress multiple frames to achieve an appreciable change in particle position, often resulting in a lower density of velocity measurements.

For the automated tracking method, the images must first be windowed and leveled to enhance the signal from the particles. The exact window and level used for each sequence affects which particles are recognized from one frame to the next. Also, due to quantum mottle in the image, the software will occasionally misidentify background noise as a particle, if this misidentified noise is near enough another particle, or if two particles come too close, the program may make an error in tracking a particles movement and produce some outliers in the velocity measurements. Some of these outlier velocity measurements can be seen most notably in the aneurysm sac shown in figure 10A, where random white arrows (denoting high velocities) point in odd directions and interrupt the clearly identifiable tracks of other particles. With further analysis and by carefully selecting program parameters when performing X-PIV, it is believed that these extraneous velocity

measurements can be further minimized or removed entirely.

Also of note, the cardiac pump simulates the different phases of the heart beating, but the acquired velocity data is displayed for measurements made over the entire imaging sequence. Within the sequence, flow varies despite the addition of a flow dampener to the loop. For the purposes of this experiment the velocity data was averaged across time and space to provide simple velocity maps, but in practice the data is time stamped and could be matched to a recorded cardiac cycle to show variations in flow due to cardiac phase.

Varying frame rates impacts velocity measurements. Though flow patterns remain the approximately the same, the velocity magnitudes are impacted as fast moving particles become more difficult to resolve. It is uncertain what degree of precision is needed from the X-PIV measurements in order to estimate the impact of pathology or of treatment, though even at 333 fps, there does seem to be sufficient accuracy for use in the clinic.

6.5 Conclusion

New experimental methods of quantifying flow properties in patient-specific phantoms have been presented. Flow measurements from injected iodine contrast and X-PIV have been demonstrated to be effective methods for quantifying flow in a variety of both patient specific and idealized geometries. The automated flow measurements were verified manually in two of the cases and the difference was found to be minimal. The flow measurements made in the experiments provide both qualitative and quantitative information regarding flow within vessels. These flow details can be used in treatment planning or in validating results from computational methods. It is also hoped that it may eventually be extended for use in the clinic to assess the effectiveness of endovascular interventions if appropriate particles or if better methods for measuring injected iodine contrast can be developed.

Chapter 7

Summary and Future Works

7.1 Summary

With the high prevalence of stroke, and its high rate of mortality and morbidity, improved imaging capabilities are needed to both diagnose and properly treat cerebral vascular pathologies. Minimally invasive EIGIs have become an important tool for treatment of many cerebral vascular pathologies due to reductions in patient discomfort and recovery times and reductions in mortality and morbidity. During these procedures, proper visualization of anatomical and interventional device detail becomes paramount to the success of the treatment. Conventional imaging with image intensifiers and FPDs lacks the spatial and temporal resolution to resolve critical details that can guide image-guided interventions. Improvements to both spatial and temporal resolution through use of state of the art detectors can improve visualization of interventional device detail and placement as well as provide insight into vascular flow detail. The imaging group at the Canon Stroke and Vascular Research Center has worked to help develop these state of the art detectors and develop new methods for their use in the clinic.

A new Canon detector with an integrated high spatial resolution ROI imager provides the improved spatial resolution needed for EIGIs alongside standard spatial resolution. This new detector was subjected to a variety of tests to assess the improved performance of the Hi-Def mode relative

to the FPD mode in resolving image details. The first quantitative test performed on these detectors was a measurement of the DQE for both detectors, and it was shown that for all spatial frequencies above 0.2 lp/mm the Hi-Def mode of the detector outperformed the FPD mode. The generalized performance of these detectors was also measured using generalized versions of the MTF, NNPS, and DQE for both detector modes. These generalized metrics include factors such as image scatter and feature blurring, and in spite of these deleterious effects the Hi-Def still outperforms the FPD mode, albeit the improved performance is much reduced from the standard metrics due to blurring effects negating some of the gains from improved spatial resolution. The final test performed was an objective, quantitative test using the relative object detectability (ROD) family of metrics which quantifies the relative detectors' abilities to image objects. The ROD metric integrates the detector DQE multiplied by the object functions for each spatial frequency taken in ratio with the same quantity for another detector. The ROD metric was calculated for a variety of objects with various diameters, and measurements showed that for all objects the Hi-Def mode had improved imaging performance and achieved better than three times the performance of the FPD mode. The G-ROD is calculated in a manner similar to the ROD but uses the generalized DQE in place of the detector DQE. The G-ROD was performed in an identical manner to the ROD metric with various scatter and magnification factors, and again the Hi-Def mode had improved performance over the FPD mode with the degree of the improvement being highly dependent on the scatter and magnification. The final measurement used was the GM-ROD which compares detectors' ability to image real-world objects. The GM-ROD was calculated for a pipeline stent object over a range of magnification values and the results showed improved performance of the Hi-Def relative to the FPD. Furthermore, when varying the integration bounds to focus on image detail, the Hi-Def achieved nearly ten times the performance of the FPD mode at low magnification. Overall the Hi-Def mode demonstrated improved image performance across all tests.

Anti-scatter grids improve image contrast by preventing scatter from reaching the detector. The improved contrast comes at the cost of attenuation of the primary beam before reaching the detector face and therefore increasing dose to the patient. The new Canon detector with Hi-Def

mode is equipped with an anti-scatter grid, though the grid becomes less efficient for small FOVs. The performance of the Hi-Def mode is assessed with and without the grid to assess its impact on image quality. With the grid removed the Hi-Def demonstrates equivalent performance as measured by the DQE relative to the photon fluence at the detector surface. If calculated from the photon fluence measured just prior to the grid we see that the Hi-Def mode without the grid provides superior image quality due to a reduction in image noise. These results are reflected in the measured ROD metrics which demonstrate the improved performance of the Hi-Def mode without the grid in place for small diameter objects. As a result, incorporating a removable grid in the Canon Hi-Def detector can provide improved image quality for equivalent dose, or maintain image quality for a reduced patient dose.

Image quality may also be impacted by motion, either of the patient or of the detector. Patient motion can be unpredictable, but gantry motion can be predicted and accounted for. The magnitude of gantry motion blur in individual projections was derived mathematically from parameters such as rotational velocity, frame exposure time, and object positional data. The motion blur was verified experimentally for projection images. Since the gantry is unlikely to frequently be in motion during imaging, the impact of gantry motion blur is of greatest impact in acquiring CBCT image data. To assess the degradation of CBCT due to gantry motion a fine featured pattern phantom was simulated and simulated CBCT was performed for different imaging frame rates and the measured blur was compared to the predicted blur demonstrating good agreement. Images reconstructed from higher frame rates demonstrated reduced blur relative to lower frame rates.

Image quality can also be improved not just by improving spatial resolution, but also temporal resolution. The Actaeon detector from XCounter has $100 \mu\text{m}$ pixels and can operate at up to 1000 fps, giving temporal resolution never before seen in the clinic. The high temporal resolution of the Actaeon detector enables a new imaging protocol that we have termed high-speed angiography (HSA). HSA has already been employed to reduce blurring in rapid CBCT and its applications are being further explored for use in the clinic. HSA was used to provide qualitative assessment of blood flow in patient specific 3D-printed phantoms. Initial experiments used pulsed imaging, but

interruptions to visualization of flow detail proved frustrating and important flow detail was lost during portions of the cardiac cycle. To maximize the visualization of flow detail, a new source was obtained enabling the acquisition of continuous flow detail over a total of 2.4 seconds, allowing for the visualization of flow detail across multiple cardiac cycles.

The visualization of blood flow detail can improve diagnosis and treatment of vascular pathology. Understanding of the impact of flow patterns can be further developed through quantification of blood flow. Methods for quantifying blood flow from 1000 fps HSA images have been developed. One of these methods relies on the manual tracking of injected iodine contrast and is tedious for users. The remaining two methods tracked radio-opaque particles as they pass through 3D printed vessels in a procedure we have termed x-ray particle image velocimetry (X-PIV). The first method of X-PIV also relied on manual particle tracking and the second used automated particle identification and tracking methods (through use of the software package trackpy) to quantify vascular flow. The automated method was applied to five unique 3D printed vascular phantoms, resulting in thousands of individual velocity measurements for each image sequence. The measured velocities were mapped onto projection images and were compared to manual X-PIV methods for quantifying flow. The two X-PIV methods demonstrated good agreement validating its capacity as a tool for measuring flow. Lower frame rates were simulated and automated X-PIV performed on the new image sequences. As the simulated frame rate dropped, the accuracy of the higher velocity measurements dropped as well. 1000 fps HSA clearly provides the greatest accuracy of flow measurements, but even at just 333 fps there still appears to be sufficient temporal resolution to resolve most of the flow detail.

7.2 Future Works

7.2.1 Impact of Anti-Scatter Grid on Hi-Def Mode

The analysis performed on the Hi-Def mode with and without the anti-scatter grid was limited in scope, measuring only a few of the imaging capabilities of the Hi-Def zoom mode. Further

analysis needs to be performed to assess the impact of the grid on image quality using generalized metrics. The GM-ROD metric could also be employed for assessing the impact of scatter and magnification factors on imaging stents and other interventional devices. The above metrics are useful in quantifying system performance, but to assess how the presence of an anti-scatter grid impacts perception, a model observer such as the channelized Hotelling observer should be employed.

7.2.2 Quantification of Blood Flow with HSA

The use of particles in X-PIV provides an excellent tool for studying blood flow conditions in phantoms. But to truly realize the full potential of HSA and its utility in quantifying blood flow, new techniques are being developed that quantify the movement of iodine contrast in 3D printed vessels using HSA image sequences. Once developed this tool could be ready for use in patients as it requires only iodine contrast and exposures with sufficient fluence to visualize the injected contrast. In addition, the energy discriminating nature of single photon counting detectors may someday enable material separation, allowing for the isolation of iodine contrast from background noise.

7.2.3 Time Dependent Comparative Metrics

The imaging group at the University at Buffalo is seeking to promote the development of more high-speed detectors for future use in the clinic. As high-speed detectors become more common, new methods will be needed to compare the time-dependent performance of detectors. Work has already begun to quantify a temporal modulation transfer function and temporal noise power spectrum.⁸⁰ With these two measurements, it should be possible to develop a temporal detective quantum efficiency metric. This opens up the possibility of developing a new family of temporal relative object detectability (t-ROD). These new metrics would allow for an assessment of temporal and spatial properties of new detectors and enable an objective comparison in their abilities to resolve critical image detail.

7.3 Conclusions

Endovascular image-guided interventions need improved image resolution in both the temporal and spatial domain. The imaging group at the Canon Stroke and Vascular Research Center has worked to develop, characterize, and further promote the development of detectors that improve image resolution. As the work has continued these detectors have begun to be implemented into the clinic for use in interventional procedures. The high spatial resolution detectors have already begun to impact procedures and our group has received positive feedback from physicians. This group has also sought to develop methods that could take advantage of the high temporal resolution provided by new single photon counting detectors to quantify blood flow and reduce image blurring due to gantry motion. As further development is pursued these tools will be further expanded and methods for quantifying performance will also need to be developed. Though use of high spatial and temporal resolution detectors may necessitate a higher dose rate to maintain image quality, it is believed by this group that the improved visualization of image detail may lead to shorter procedures due to the ability to more quickly ascertain conditions from improved image visualization, thus lowering patient dose over the procedure. High-speed angiography also provides new tools that could expand the capabilities of interventional procedures, improving treatment outcomes, and enabling new measurements that could broaden our understanding of vascular pathologies and their treatment methods.

References

- [1] NINDS. *What You Need to Know About Stroke*. <https://www.stroke.nih.gov/materials/needtoknow.htm>. (Accessed on 03/04/2020). Apr. 2004.
- [2] National Institute of Neurological Disorders and Stroke. *Stroke Information Page*. <https://www.ninds.nih.gov/Disorders/All-Disorders/Stroke-Information-Page>. (Accessed on 03/04/2020). Mar. 2019.
- [3] *Stroke*. <https://medlineplus.gov/stroke.html>. (Accessed on 03/04/2020).
- [4] *Ischemic Strokes (Clots) — American Stroke Association*. <https://www.stroke.org/en/about-stroke/types-of-stroke/ischemic-stroke-clots>. (Accessed on 03/04/2020).
- [5] *Transient ischemic attack (TIA) - Symptoms and causes - Mayo Clinic*. <https://www.mayoclinic.org/diseases-conditions/transient-ischemic-attack/symptoms-causes/syc-20355679>. (Accessed on 03/04/2020).
- [6] *Hemorrhagic Strokes (Bleeds) — American Stroke Association*. <https://www.stroke.org/en/about-stroke/types-of-stroke/hemorrhagic-strokes-bleeds>. (Accessed on 03/04/2020).
- [7] Graeme J Hankey, Konrad Jamrozik, Robyn J Broadhurst, Susanne Forbes, Peter W Burvill, Craig S Anderson, and Edward G Stewart-Wynne. “Five-year survival after first-ever stroke and related prognostic factors in the Perth Community Stroke Study”. In: *Stroke* 31.9 (2000), pp. 2080–2086.
- [8] *Cerebral Aneurysms Fact Sheet — National Institute of Neurological Disorders and Stroke*. <https://www.ninds.nih.gov/Disorders/Patient-Caregiver-Education/Fact-Sheets/Cerebral-Aneurysms-Fact-Sheet>. (Accessed on 03/04/2020).
- [9] *Arteriovenous Malformation — AVM — MedlinePlus*. <https://medlineplus.gov/arteriovenousmalformations.html>. (Accessed on 03/04/2020).
- [10] *What is an Arteriovenous Malformation — American Stroke Association*. <https://www.stroke.org/en/about-stroke/types-of-stroke/hemorrhagic->

strokes-bleeds/what-is-an-arteriovenous-malformation. (Accessed on 03/04/2020).

- [11] *Know the signs of stroke - Harvard Health*. <https://www.health.harvard.edu/healthbeat/know-the-signs-of-stroke>. (Accessed on 03/04/2020).
- [12] *Lets Talk About Stroke Diagnosis*. <https://www.stroke.org/-/media/stroke-files/about-stroke/stroke-symptoms/lets-talk-about-stroke-diagnosis-ucm309722.pdf?la=en&hash=738C52586818E10E713252DFD247CB425F90> (Accessed on 03/04/2020).
- [13] *Stroke - Diagnosis and treatment - Mayo Clinic*. <https://www.mayoclinic.org/diseases-conditions/stroke/diagnosis-treatment/drc-20350119>. (Accessed on 03/04/2020).
- [14] *Brain aneurysm - Diagnosis and treatment - Mayo Clinic*. <https://www.mayoclinic.org/diseases-conditions/brain-aneurysm/diagnosis-treatment/drc-20361595>. (Accessed on 03/04/2020).
- [15] Randall T Higashida, BJ Lahue, MT Torbey, LN Hopkins, E Leip, and Daniel F Hanley. "Treatment of unruptured intracranial aneurysms: a nationwide assessment of effectiveness". In: *American Journal of Neuroradiology* 28.1 (2007), pp. 146–151.
- [16] *Arteriovenous Malformations – Symptoms, Diagnosis and Treatment Options*. <https://www.aans.org/Patients/Neurosurgical-Conditions-and-Treatments/Arteriovenous-Malformations>. (Accessed on 03/04/2020).
- [17] Jerrold T Bushberg and John M Boone. "Fluoroscopic Detector Systems". In: *The essential physics of medical imaging*. Lippincott Williams & Wilkins, 2011.
- [18] Jerrold T Bushberg and John M Boone. "Flat Panel Thin-Film-Transistor Array Detectors". In: *The essential physics of medical imaging*. Lippincott Williams & Wilkins, 2011.
- [19] Edward Lee Nickoloff. "AAPM/RSNA physics tutorial for residents: physics of flat-panel fluoroscopy systems: survey of modern fluoroscopy imaging: flat-panel detectors versus image intensifiers and more". In: *Radiographics* 31.2 (2011), pp. 591–602.
- [20] Peter Kan, Parham Yashar, Ciprian N Ionita, Amit Jain, Stephen Rudin, Elad I Levy, and Adnan H Siddiqui. "Endovascular coil embolization of a very small ruptured aneurysm using a novel microangiographic technique". In: *Journal of neurointerventional surgery* 5.2 (2013), e2–e2.
- [21] Mandy J Binning, David Orion, Parham Yashar, Sharon Webb, Ciprian N Ionita, Amit Jain, Stephen Rudin, LNelson Hopkins, Adnan H Siddiqui, and Elad I Levy. "Use of the mi-

- croangiographic fluoroscope for coiling of intracranial aneurysms”. In: *Neurosurgery* 69.5 (2011), pp. 1131–1138.
- [22] Robert M Starke, Aquilla Turk, Dale Ding, Richard W Crowley, Kenneth C Liu, Nohra Chalouhi, David M Hasan, Aaron S Dumont, Pascal Jabbour, Christopher R Durst, et al. “Technology developments in endovascular treatment of intracranial aneurysms”. In: *Journal of neurointerventional surgery* 8.2 (2016), pp. 135–144.
- [23] SV Setlur Nagesh, Vernard Fennel, Jordan Krebs, Ciprian Ionita, Jason Davies, Daniel R Bednarek, Maxim Mokin, Adnan H Siddiqui, and Stephen Rudin. “High-Definition Zoom Mode, a High-Resolution X-Ray Microscope for Neurointerventional Treatment Procedures: A Blinded-Rater Clinical-Utility Study”. In: *American Journal of Neuroradiology* 40.2 (2019), pp. 302–308.
- [24] Ehsan Samei, Michael J Flynn, and David A Reimann. “A method for measuring the pre-sampled MTF of digital radiographic systems using an edge test device”. In: *Medical physics* 25.1 (1998), pp. 102–113.
- [25] Jerrold T Bushberg and John M Boone. “The Frequency Domain”. In: *The essential physics of medical imaging*. Lippincott Williams & Wilkins, 2011.
- [26] International Electrotechnical Commission et al. “Medical electrical equipment: characteristics of digital x-ray imaging devices. I”. In: *Determination of the detective quantum efficiency*. Geneva, Switzerland: International Electrotechnical Commission (2003).
- [27] Iacovos S Kyprianou, Stephen Rudin, Daniel R Bednarek, and Kenneth R Hoffmann. “Generalizing the MTF and DQE to include x-ray scatter and focal spot unsharpness: Application to a new microangiographic system”. In: *Medical physics* 32.2 (2005), pp. 613–626.
- [28] Iacovos S Kyprianou, Stephen Rudin, Daniel R Bednarek, and Kenneth R Hoffmann. “Study of the generalized MTF and DQE for a new microangiographic system”. In: *Medical Imaging 2004: Physics of Medical Imaging*. Vol. 5368. International Society for Optics and Photonics. 2004, pp. 349–360.
- [29] G Lubberts and K Rossmann. “Modulation transfer function associated with geometrical unsharpness in medical radiography”. In: *Physics in Medicine & Biology* 12.1 (1967), p. 65.
- [30] Virgil N Cooper III, John M Boone, J Anthony Seibert, and Claire J Pellot-Barakat. “An edge spread technique for measurement of the scatter-to-primary ratio in mammography”. In: *Medical physics* 27.5 (2000), pp. 845–853.
- [31] Egbert Buhr, Susanne Günther-Kohfahl, and Ulrich Neitzel. “Simple method for modulation transfer function determination of digital imaging detectors from edge images”. In: *Medical Imaging 2003: Physics of Medical Imaging*. Vol. 5030. International Society for Optics and Photonics. 2003, pp. 877–884.

- [32] Arundhuti Ganguly, Stephen Rudin, Daniel R Bednarek, Kenneth R Hoffmann, and Iacovos S Kyprianou. “Micro-angiography for neuro-vascular imaging. I. Experimental evaluation and feasibility”. In: *Medical physics* 30.11 (2003), pp. 3018–3028.
- [33] Charles E Metz, Robert F Wagner, Kunio Doi, David G Brown, Robert M Nishikawa, and Kyle J Myers. “Toward consensus on quantitative assessment of medical imaging systems”. In: *Medical physics* 22.7 (1995), pp. 1057–1061.
- [34] Arthur E Burgess. “Comparison of receiver operating characteristic and forced choice observer performance measurement methods”. In: *Medical physics* 22.5 (1995), pp. 643–655.
- [35] V Singh, A Jain, DR Bednarek, and S Rudin. “Relative object detectability (ROD): a new metric for comparing x-ray image detector performance for a specified object of interest”. In: *Medical Imaging 2014: Physics of Medical Imaging*. Vol. 9033. International Society for Optics and Photonics. 2014, p. 90335I.
- [36] V Singh, A Jain, D Bednarek, and S Rudin. “SU-E-I-29: Generalized Relative Object Detectability (G-ROD): A Metric for Comparing X-Ray Imaging Detector Systems”. In: *Medical Physics* 41.6Part5 (2014), pp. 136–136.
- [37] M Russ, V Singh, B Loughran, DR Bednarek, and S Rudin. “New family of generalized metrics for comparative imaging system evaluation”. In: *Medical Imaging 2015: Physics of Medical Imaging*. Vol. 9412. International Society for Optics and Photonics. 2015, p. 94121C.
- [38] M Russ, C Ionita, D Bednarek, and S Rudin. “SU-D-204-05: Quantitative Comparison of a High Resolution Micro-Angiographic Fluoroscopic (MAF) Detector with a Standard Flat Panel Detector (FPD) Using the New Metric of Generalized Measured Relative Object Detectability (GM-ROD)”. In: *Medical physics* 42.6Part3 (2015), pp. 3217–3217.
- [39] J Krebs, A Shankar, SV Setlur, DR Bednarek, and S Rudin. “Quantitative comparison of Hi-Def and FPD zoom modes in an innovative detector using Relative Object Detectability (ROD) metrics”. In: *Medical Imaging 2019: Physics of Medical Imaging*. Vol. 10948. International Society for Optics and Photonics. 2019, 109480E.
- [40] G Holje. “Coefficients for converting X-ray exposure to photon fluence and energy fluence”. In: (1983).
- [41] Vivek Singh. *Evaluation of performance of various high resolution x-ray imaging detectors*. State University of New York at Buffalo, 2014.
- [42] Brendan Loughran. *Experimental assessment and comparison of x-ray detectors for use in neuro-endovascular imageguided interventions*. 2014.
- [43] <http://www.ni.com/en-us/shop/select/can-interface-device>.

- [44] SN Swetadri Vasan, Ciprian N Ionita, AH Titus, AN Cartwright, DR Bednarek, and S Rudin. “Graphics processing unit (GPU) implementation of image processing algorithms to improve system performance of the control acquisition, processing, and image display system (CAPIDS) of the micro-angiographic fluoroscope (MAF)”. In: *Medical Imaging 2012: Physics of Medical Imaging*. Vol. 8313. International Society for Optics and Photonics. 2012, p. 83134C.
- [45] Jerrold T Bushberg and John M Boone. “Scattered Radiation in Projection Radiographic Imaging”. In: *The essential physics of medical imaging*. Lippincott Williams & Wilkins, 2011.
- [46] Gustav Bucky. *Method of and apparatus for projecting röntgen images*. US Patent 1,164,987. Dec. 1915.
- [47] Hollis E Potter. “The Bucky diaphragm principle applied to roentgenography”. In: *Archives of Radiology and Electrotherapy* 25.10 (1921), pp. 310–315.
- [48] Gary T Barnes. “Contrast and scatter in x-ray imaging.” In: *Radiographics* 11.2 (1991), pp. 307–323.
- [49] Willi Kalender. “Monte Carlo calculations of x-ray scatter data for diagnostic radiology”. In: *Physics in Medicine & Biology* 26.5 (1981), p. 835.
- [50] Robert YL Chu, Jane Fisher, Benjamin R Archer, Burton J Conway, and MM Goodsit. “AAPM Report No. 31: Standardized Methods for Measuring Diagnostic X-Ray Exposures”. In: *New York, USA: American Association of Physicists in Medicine by the American Institute of Physics* (1990).
- [51] Wayne S Rasband et al. *ImageJ*. 1997.
- [52] J Krebs, A Shankar, M Russ, D Bednarek, and S Rudin. “Effect of Motion Blur On High Resolution Fluoroscopic (HRF) Detector Projection Views Used for Cone-Beam Computed Tomography (CBCT): SU-E-201-04”. In: *Medical Physics* 44.6 (2017), pp. 2739–2740.
- [53] *XC-Actaeon - Direct Conversion*. <https://directconversion.com/product/xc-actaeon/>. (Accessed on 03/12/2020).
- [54] J Krebs, A Shankar, DR Bednarek, and S Rudin. “Gantry rotational motion-induced blur in cone-beam computed tomography”. In: *Medical Imaging 2018: Physics of Medical Imaging*. Vol. 10573. International Society for Optics and Photonics. 2018, 105734B.
- [55] Ronak Dholakia, Chander Sadasivan, David J Fiorella, Henry H Woo, and Baruch B Lieber. “Hemodynamics of flow diverters”. In: *Journal of biomechanical engineering* 139.2 (2017).

- [56] Jingfeng Jiang and Charles Strother. “Computational fluid dynamics simulations of intracranial aneurysms at varying heart rates: a “patient-specific” study”. In: *Journal of biomechanical engineering* 131.9 (2009).
- [57] Robert K Swank. “Absorption and noise in x-ray phosphors”. In: *Journal of Applied Physics* 44.9 (1973), pp. 4199–4203.
- [58] Katsuyuki Taguchi and Jan S Iwanczyk. “Vision 20/20: Single photon counting x-ray detectors in medical imaging”. In: *Medical physics* 40.10 (2013).
- [59] Jesse Tanguay, Ho Kyung Kim, and Ian A Cunningham. “The role of x-ray Swank factor in energy-resolving photon-counting imaging”. In: *Medical physics* 37.12 (2010), pp. 6205–6211.
- [60] Markku J Tapiovaara and R Wagner. “SNR and DQE analysis of broad spectrum x-ray imaging”. In: *Physics in Medicine & Biology* 30.6 (1985), p. 519.
- [61] Lucian Wielopolski and Robin P Gardner. “Prediction of the pulse-height spectral distortion caused by the peak pile-up effect”. In: *Nuclear Instruments and Methods* 133.2 (1976), pp. 303–309.
- [62] Cheng Xu, Mats Danielsson, and Hans Bornefalk. “Evaluation of energy loss and charge sharing in cadmium telluride detectors for photon-counting computed tomography”. In: *IEEE Transactions on Nuclear Science* 58.3 (2011), pp. 614–625.
- [63] P Guerra, A Santos, and DG Darambara. “Development of a simplified simulation model for performance characterization of a pixellated CdZnTe multimodality imaging system”. In: *Physics in Medicine & Biology* 53.4 (2008), p. 1099.
- [64] E Gros d’Aillon, Marie Claude Gentet, Guillaume Montémont, Jacques Rustique, and Loick Verger. “Simulation and experimental results on monolithic CdZnTe gamma-ray detectors”. In: *IEEE transactions on nuclear science* 52.6 (2005), pp. 3096–3102.
- [65] A Shankar, J Krebs, M Russ, D Bednarek, and S Rudin. “energy Spectra Measurements with a Cdte-based Imaging Photon Counting Detector (pcd): we-ram1-gepd-i-06”. In: *Medical Physics* 44.6 (2017).
- [66] A Shankar, J Krebs, DR Bednarek, and S Rudin. “Evaluation of a new photon-counting imaging detector (PCD) with various acquisition modes”. In: *Medical Imaging 2018: Physics of Medical Imaging*. Vol. 10573. International Society for Optics and Photonics. 2018, 105734Y.
- [67] A Shankar, J Krebs, DR Bednarek, and S Rudin. “Spectroscopy with a CdTe-based photon-counting imaging detector (PCD) having charge sharing correction capability”. In: *Medical*

Imaging 2018: Physics of Medical Imaging. Vol. 10573. International Society for Optics and Photonics. 2018, p. 1057352.

- [68] PA Shankar et al. “Characterization and Evaluation of High Spatio-Temporal Resolution Aspects of X-ray Detectors in Medical Imaging”. PhD thesis. State University of New York at Buffalo, 2019.
- [69] A Shankar, M Russ, J Krebs, D Bednarek, and S Rudin. “initial Investigation of Various Modes in a Cdte-based Imaging Photon Counting Detector (pcd): we-ab-601-07”. In: *Medical Physics* 44.6 (2017).
- [70] M Russ, R O’Hara, SV Setlur Nagesh, M Mokin, C Jimenez, A Siddiqui, D Bednarek, Stephen Rudin, and C Ionita. “Treatment planning for image-guided neuro-vascular interventions using patient-specific 3D printed phantoms”. In: *Medical Imaging 2015: Biomedical Applications in Molecular, Structural, and Functional Imaging*. Vol. 9417. International Society for Optics and Photonics. 2015, p. 941726.
- [71] Ciprian N Ionita, Maxim Mokin, Nicole Varble, Daniel R Bednarek, Jianping Xiang, Kenneth V Snyder, Adnan H Siddiqui, Elad I Levy, Hui Meng, and Stephen Rudin. “Challenges and limitations of patient-specific vascular phantom fabrication using 3D Polyjet printing”. In: *Medical Imaging 2014: Biomedical Applications in Molecular, Structural, and Functional Imaging*. Vol. 9038. International Society for Optics and Photonics. 2014, p. 90380M.
- [72] Megan Kelly Russ. “Characterization of High Resolution X-Ray Detector Systems with Applications in Neuro-Endovascular Image Guided Interventions”. PhD thesis. State University of New York at Buffalo, 2017.
- [73] JM Krebs, A Shankar, SV Setlur Nagesh, JM Davies, KV Snyder, EI Levy, LN Hopkins, M Mokin, DR Bednarek, AH Siddiqui, and S Rudin. “Flow-Pattern Details in an Aneurysm Model Using High-Speed 1000-Frames-per-Second Angiography”. In: *American Journal of Neuroradiology* 40.7 (2019), pp. 1197–1200.
- [74] J Krebs, A Shankar, D Bednarek, and S Rudin. “Extending the Sequence Length for High Speed Angiography (HSA) Revealing Detailed Vascular Flow”. In: *MEDICAL PHYSICS*. Vol. 46. 6. WILEY 111 RIVER ST, HOBOKEN 07030-5774, NJ USA. 2019, E212–E212.
- [75] J Collins, J Krebs, D Bednarek, and S Rudin. “Evaluation of Dose for High-Speed Angiography (HSA) with a High Frame-Rate Image Receptor”. In: *MEDICAL PHYSICS*. Vol. 46. 6. WILEY 111 RIVER ST, HOBOKEN 07030-5774, NJ USA. 2019, E390–E390.
- [76] J Krebs, A Shields, D Bednarek, and S Rudin. “Simultaneous Acquisition of High Speed Angiography (HSA) at 1000 Frames Per Second during Digital Subtraction Angiography (DSA) and Digital Angiography (DA)”. In: *RSNA Scientific Assembly and Annual Meeting*. Radiological Society of North America 2019 Scientific Assembly and Annual Meeting. 2019.

- [77] DB Allan, TA Caswell, and NC Keim. “Trackpy v0. 2, 2014”. In: *URL github.com/soft-matter/trackpy* ().
- [78] J Krebs, A Sharma, A Shields, D Bednarek, and S Rudin. “Quantitative flow velocity analysis of 1000 frames per second (fps) high speed angiography (HSA) image sequences”. In: *RSNA Scientific Assembly and Annual Meeting*. Radiological Society of North America 2019 Scientific Assembly and Annual Meeting. 2019.
- [79] J Krebs, A Shields, A Sharma, LM Shepard, CN Ionita, DR Bednarek, and S Rudin. “Initial investigations of x-ray particle imaging velocimetry (X-PIV) in 3D printed phantoms using 1000 fps High-Speed Angiography (HSA)”. In: *Medical Imaging 2020: Biomedical Applications in Molecular, Structural, and Functional Imaging*. Vol. 11317. International Society for Optics and Photonics. 2020, p. 1131714.
- [80] M Russ, S Mann, T Richards, and E Samei. “Quantitative Evaluation of Clinical Fluoroscopy Systems: Reproducibility of Temporal Modulation Transfer Function and Temporal Noise Power Spectrum Measurements Using a Rotating Edge Method”. In: *MEDICAL PHYSICS*. Vol. 46. 6. WILEY 111 RIVER ST, HOBOKEN 07030-5774, NJ USA. 2019, E528–E529.

Appendix A: List of Publications and Presentations

Peer Reviewed Journal Articles

1. J. Krebs, A. Shankar, S.V. Setlur Nagesh, J. Davies, E. Levy, L. Hopkins, M. Mokin, D. Bednarek, A. Siddiqui, S. Rudin, “Flow pattern details in an aneurysm model using high-speed 1000 frames per second angiography,” American Journal of Neuroradiology June 2019, DOI: 10.3174/ajnr.A6090
2. S.V. Setlur Nagesh, V. Fennel, J. Krebs, C. Ionita, J. Davies, D.R. Bednarek, M. Mokin, A.H. Siddiqui, S. Rudin, “High-Definition Zoom Mode, a High-Resolution X-Ray Microscope for Neurointerventional Treatment Procedures: A Blinded-Rater Clinical-Utility Study” American Journal of Neuroradiology Dec 2018, DOI: 10.3174/ajnr.A5922

Peer Reviewed Conference Proceedings

1. J. Krebs, A. Shields, A. Sharma, L. Shepard, C. Ionita, D. R. Bednarek, S. Rudin, “Initial investigations of x-ray particle imaging velocimetry (X-PIV) in 3D printed phantoms using 1000 fps High-Speed Angiography (HSA),” 2020 SPIE, Feb 15 – Feb 20, Houston, TX.
2. J. Krebs, S.V. Setlur Nagesh, L. Shepard, C. Ionita, D. R. Bednarek, S. Rudin, “Quantifying the effects of stenosis on blood flow using 1000 fps High-Speed Angiography (HSA),” 2020

SPIE, Feb 15 – Feb 20, Houston, TX.

3. J. Krebs, A. Shields, D. R. Bednarek, S. Rudin, “Simultaneous acquisition of high speed angiography (HSA) at 1000 frames per second during digital subtraction Angiography (DSA) and Digital Angiography (DA),” 2019 RSNA, Nov 30 – Dec 5, Chicago, IL.
4. J. Krebs, A. Shields, D. R. Bednarek, S. Rudin, “Quantitative Flow Velocity Analysis of 1000 Frames Per Second (fps) High Speed Angiography (HSA) Image Sequences,” 2019 RSNA, Nov 30 – Dec 5, Chicago, IL .
5. J. Krebs, A. Shankar, D. R. Bednarek, S. Rudin, “Impact of acquisition frame rate on visibility of vascular flow patterns,” 2019 AAPM, Jul 14 – Jul 18, San Antonio, TX .
6. J. Krebs, A. Shankar, D. R. Bednarek, S. Rudin, “Extending the sequence length for High Speed Angiography (HAS) revealing detailed vascular flow,” 2019 AAPM, Jul 14 – Jul 18, San Antonio, TX .
7. J. Krebs, A. Shankar, S. V. Setlur, D. R. Bednarek, S. Rudin, “Quantitative comparison of Hi-Def and FPD zoom modes in an innovative detector using Relative Object Detectability (ROD) metrics,” 2019 SPIE, Feb 16 – Feb 21, San Diego, CA.
8. J. Krebs, A. Shankar, S. Setlur Nagesh, D. Bednarek, S. Rudin “Demonstration of an Innovative Dual-Resolution X-Ray Imaging Detector System using a 3D-Printed Angiographic Phantom,” 2018 AAPM, July 29-Aug 2, Nashville, TN.
9. J. Krebs, M. Russ, A. Shankar, D. Bednarek, S. Rudin, “Effect of motion blur on High Resolution Fluoroscopic (HRF) detector projection views used for Cone-Beam Computed Tomography (CBCT),” 2017 AAPM, July 30-Aug 3, Denver, CO.

Peer Reviewed Abstracts

1. J. Krebs, A. Shankar, S. V. Setlur, D. R. Bednarek, S. Rudin, “Spatial Resolution Comparison of New High-Definition (Hi-Def) Mode with Standard Flat Panel Detector (FPD) Mode of an Innovative X-Ray Imaging Detector,” 2018 AAPM, Jul 29 – Aug 2, Nashville, TN.
2. J. Krebs, A. Shankar, D. R. Bednarek, S. Rudin, “Gantry rotational motion-induced blur in cone-beam computed tomography,” 2018 SPIE, Feb 16 – Feb 21, Houston, TX.

Additional Presentations

1. J. Krebs, A. Shankar, D. Bednarek, S. Rudin “Varying frame rate acquisition for observation of vascular flow patterns,” 2019 Upstate New York Chapter of the AAPM, April 12, Buffalo, NY.
2. J. Krebs, A. Shankar, S. Setlur Nagesh, D. Bednarek, S. Rudin “Demonstration of an Innovative Dual-Resolution X-Ray Imaging Detector System using a 3D-Printed Angiographic Phantom,” 2018 Upstate New York Chapter of the AAPM, June 22, Buffalo, NY.
3. J. Krebs, M. Russ, A. Shankar, D. Bednarek, S. Rudin, “Magnitude of motion-induced blur on High-Resolution Fluoroscopic (HRF) detector projection views due to gantry rotation in Cone-Beam Computed Tomography (CBCT),” 2017 Upstate New York Chapter of the AAPM, Apr 21, Buffalo, NY.